

**THE BREAKDOWN MECHANISMS IN ELECTRICAL DISCHARGES:  
THE ROLE OF THE FIELD EMISSION EFFECT IN DIRECT  
CURRENT DISCHARGES IN MICROGAPS****M. Radmilović-Radjenović<sup>1\*</sup>, B. Radjenović\*, M. Klas<sup>†</sup>, A. Bojarov\*  
and Š. Matejčík<sup>†</sup>***\*Institute of Physics, University of Belgrade, Pregrevica 118, 110 80 Belgrade, Serbia**†Department of Experimental Physics, Comenius University, Mlynská dolina F2  
842 48 Bratislava, Slovakia*

Received 17 March 2014, accepted 19 March 2014

This review represents an attempt to sum up the current state of the research in the field of breakdown phenomena in electrical discharges. The paper provides facts and theories concerning different classes of direct current, radio and microwave frequency discharges, in vacuum, in the gas and in liquids, without and in the presence of the magnetic fields. The emphasize was made on the field emission effects and on the fundamental aspects of the breakdown phenomena in microdischarges via discussions and analysis of the experimental, theoretical and simulation results. It was found that the Paschen's law is not applicable for the micron gap sizes, when deviations from the standard scaling law become evident and modified Paschen curve should be used. The explanation of the deviations from the Paschen law was attributed to the secondary electron emission enhanced by the strong field generated in microgaps. The experiments were carried out in order to establish scaling law in microgaps. The volt-ampere characteristics were also recorded and compared with the theoretical predictions based on the Fowler-Nordheim theory. The importance of the enhancement factor and the space charge on results was also considered. On the basis of the experimental breakdown voltage curves, the effective yields in microgaps have been estimated for different gases which can be served as input data in modeling. The effective yields allow analytically produce modified Paschen curves that predicts the deviations from the Paschen law observed in the experiments. In addition, we present results of computer simulations using a Particle-in-cell/Monte Carlo Collisions (PIC/MCC) code with the secondary emission model in order to include the field emission enhanced secondary electron production in microgaps. The agreement between simulation and experimental results suggest that computer simulations can be used to improve understanding of the plasma physics as an alternative to analytical models and to the laboratory experiments. Apart from their theoretical importance, the results reviewed in this paper could be useful for determining the minimum ignition voltages in microplasma sources as well as the maximum safe operating voltages and critical dimensions in different microdevices. Finally, the understanding of the scaling may play a crucial role in developing models of micro-discharges and applications.

DOI: 10.2478/apsrt-2013-0003

---

<sup>1</sup>E-mail address: marija@ipb.ac.rs

PACS: 51.50,+v, 52.80.-s, 52.65.Rr

KEYWORDS: Electrical discharges, Breakdown, Microdischarges, Field emission

### Contents

<b>1</b>	<b>Introduction</b>	<b>108</b>
<b>2</b>	<b>Electrical breakdown of gases</b>	<b>111</b>
<b>3</b>	<b>Townsend's breakdown mechanism</b>	<b>112</b>
3.1	Paschen law . . . . .	114
<b>4</b>	<b>Ionization coefficients</b>	<b>116</b>
4.1	Ionization coefficient in the presence of magnetic fields . . . . .	119
<b>5</b>	<b>Cathode processes-secondary effects</b>	<b>120</b>
5.1	Thermionic emission . . . . .	121
5.2	Schottky effect . . . . .	121
5.3	Field emission . . . . .	122
<b>6</b>	<b>Secondary electron emission processes</b>	<b>123</b>
6.1	Electron impact secondary emission . . . . .	123
6.2	Ion induced secondary electron emission . . . . .	125
6.2.1	Ion-enhanced field emission . . . . .	126
6.3	Secondary emission model in a crossed electric and magnetic fields . . . . .	127
6.4	Secondary emission model in a magnetic field parallel to the electric field . . . . .	128
<b>7</b>	<b>Types of discharges</b>	<b>129</b>
7.1	Direct current discharges . . . . .	130
7.1.1	Expression for the air . . . . .	132
7.2	Radio frequency discharges . . . . .	133
7.2.1	Frequency effect . . . . .	137
7.3	Combined fields . . . . .	137
7.4	Microwave discharges . . . . .	139
7.5	The effect of the magnetic fields . . . . .	141
<b>8</b>	<b>Streamer mechanism</b>	<b>144</b>
<b>9</b>	<b>Vacuum breakdown</b>	<b>147</b>
9.1	Electrode separation . . . . .	148
9.2	Electrode effects . . . . .	149
9.3	Area and the electrode configuration . . . . .	150
9.4	Temperature and the pressure effect . . . . .	151
<b>10</b>	<b>Multipaction breakdown</b>	<b>152</b>

<b>11 Breakdown in liquids</b>	<b>154</b>
11.1 Electronic breakdown . . . . .	155
11.2 Suspended solid particle mechanism . . . . .	156
11.3 Cavity breakdown . . . . .	157
<b>12 Microdischarges: departure from the Paschen curves</b>	<b>158</b>
<b>13 Historical review of the electrical discharges in strong fields</b>	<b>161</b>
<b>14 The Fowler-Nordheim equations</b>	<b>163</b>
<b>15 Space charge field</b>	<b>165</b>
15.1 Estimation of the space charge field . . . . .	165
<b>16 Semi-empirical formula</b>	<b>167</b>
16.1 The pressure dependence . . . . .	167
<b>17 Semi-analytical relation</b>	<b>170</b>
<b>18 Experimental set-up for DC breakdown in microgaps</b>	<b>171</b>
18.1 Electrodes . . . . .	171
18.2 Measurements of the breakdown voltage . . . . .	175
18.3 Measurements of the volt-ampere characteristics . . . . .	176
<b>19 Simulation technique</b>	<b>179</b>
19.1 Modeling with the PIC algorithm . . . . .	179
19.1.1 Monte Carlo module . . . . .	182
19.1.2 Mobility Calculations using Monte Carlo Collisions . . . . .	184
19.1.3 Boundary and simulation conditions . . . . .	184
19.2 Calculations of the ionization coefficients . . . . .	184
<b>20 Results for microdischarges</b>	<b>186</b>
20.1 Argon . . . . .	186
20.2 Hydrogen . . . . .	187
20.2.1 Argon-hydrogen mixtures . . . . .	190
20.3 Nitrogen . . . . .	192
20.3.1 Argon-nitrogen mixtures . . . . .	193
20.3.2 Argon-hydrogen-nitrogen mixtures . . . . .	194
20.4 Air . . . . .	195
<b>21 Conclusions</b>	<b>198</b>
<b>Acknowledgment</b>	<b>199</b>
<b>References</b>	<b>200</b>

## 1 Introduction

Plasma breakdown as an important fundamental process in plasma science has been a subject of enormous studies from the early days of gaseous electronics, due to its relevance in a wide range of applications [1]-[15] and for a deeper understanding of fundamental plasma behavior [16]-[28]. Renewed interest in breakdown phenomena, especially breakdown in small gaps, emerged from the possibility of lower facility and process costs for a variety of plasma processing and micro-manufacturing techniques currently performed at low pressures. At the same time, direct current (DC), pulsed DC and radio-frequency (RF) discharges are widely used in the microelectronics industry, in plasma display panels, for depositing thin films, for semiconductor processing, surface modification, analytical chemistry, biotechnological and environmental applications, waste treatment, etc. [29]-[35]. As already pointed out, a better understanding of voltage breakdown, besides being scientifically interesting, will aid progress in many fields and technologies, which generally fall into two categories: those that require high electric fields, and those that require high electric currents. On the other hand, unwanted voltage breakdown limits many technologies involving high electric fields [36].

Electric breakdown is referred to as a process that transforms a non-conducting material to a conducting one when a sufficient strong electric field is applied comprising an involved set of transient processes such as collision of electrons, ions and photons with gas molecules and electrode processes which take place at or near the electrode surface. Other possible gas processes include ion-atom collisions, excited atom-molecule collisions, and atom-atom collisions. In 1928, Langmuir [37] introduced the word plasma to describe the ionized gas that is created in a gas discharge. Without mentioning any further developments in plasma physics during the past decades, we conclude that nowadays gas discharges are known to consist of a collection of different particles, mainly electrons, ions, neutral atoms and molecules. These particles have a variety of interactions with each other, with surrounding wall materials and with electric and magnetic fields present in the discharge. This multitude of particles and interactions makes a gas discharge a complex system that is still not fully understood.

It was shown that in large scale systems, the experimentally observed Paschen law [38] has been successfully explained by the Townsend theory [39]. The processes that are primarily responsible for the breakdown of a gas are ionization by charged particle collisions, photo-ionization and the secondary ionization processes. However, Townsend mechanism when applied to breakdown at atmospheric pressure have some shortcoming [40] -[43]. The high electric fields obtained in small gaps combined with the lowering of the potential barrier seen by the electrons in the cathode as an ion approaches lead to the onset of ion-enhanced field emissions [44] -[48].

Microdischarge is a concept applied to a small, localized plasma region which, due to its size, demonstrates characteristics different from those of plasma regions created on a larger scale. A benefit of microdischarges is that they can exist as unbounded discharges, where their size is determined by the electrode spacing, electrode shape, pressure, and temperature as opposed to the volume of the spatial cavity in which they are generated. Despite the high collision rate at pressures as high as atmosphere, the electrons are in non-equilibrium, as they have much higher temperatures. In these weakly

ionized plasmas, electron-electron and electron-ion collisions can be ignored compared to electron-neutral collisions. In addition, the positive column, typically observed in macroscale plasmas, can be absent. At higher operating pressures, microdischarges pass into high-temperature arcs or microarcs. Although many interesting application-oriented studies have been extensively performed, only a limited number of reports about their basic discharge characteristics have been published so far [43]-[48].

In the past few decades the field of microdischarges have become more common in everyday life and the field of microdischarges has grown into the most interesting field of the physics of collisional nonequilibrium plasmas [49]. Although, the initial motivation for these studies came from the need to optimize plasma screens [50], new applications were developed very rapidly. Localized silicon etching [51], tunable UV source [52], gas spectroscopy [53], spectroscopy of water impurities [54], localized treatment of materials and assembly of nanostructures [55], to name a few, all have the features with dimensions in the micron and sub-micron range. Recently, an effort to fabricate microplasma sources that can be integrated with other MEMS (microelectromechanical systems) to form larger microsystems has been made. Plasma-based microsystems can find application in bio-microelectromechanical systems (bio-MEMS) sterilization, small-scale materials processing and microchemical analysis systems [56]. However, integrability requires not only a reduction in size, but also the understanding of the physics governing the new small-scale discharges.

Every new generation of devices is stringently followed by scaling down of device feature sizes and consequently reducing of the gap spacing. Downscaling of devices can result in a reduced electrical breakdown voltage which, if ignored, can cause problems during device operation. In fact, devices with micrometer and sub-micrometer gaps can face a serious challenge due to electrical breakdown during manufacturing, handling and operation. Therefore, the knowledge of gas breakdown conditions in a discharge device are needed for optimization of plasma technological processes [57]. It also serves as input data for plasma discharge modeling [58, 59].

There are numerous unresolved question to clarify in order to get better understanding of the phenomena involved in microplasmas where complex behaviors are observed [60, 61]. Electric field is one of the key parameters in discharge dynamics which should be better understood for the discharge optimization. Concerning the physical process responsible for the sustaining of the discharge, the question of electronic secondary emission at the cathode emerges as a very important one. Microdischarges operate under such conditions that the role of boundary dominated phenomena and the possible breakdown of standard  $pd$  scaling become very important [62]-[64]. Actually, electrical breakdown in microgaps occurs at voltages far below the pure Paschen curve minimum and the modified Paschen curve should be used instead for micron and sub-micron gaps. Electrons generated by the field emission are one of the possible reasons why the breakdown and sparks occur in the vacuum, which of course is not possible if one only considers the Townsend avalanche mechanisms for the gas phase and the surface ionization that are normally used to generate the Paschen curve.

Plasma physics has motivated a great interest in computer simulation, considering the plasmas complex nature. The simulation has played an essential role in understanding and development of plasma theory. Beside this, the computer simulation has an

important role in the design and prediction of plasma physics applications, representing a fast and inexpensive tool with its applicability ranging from low temperature plasmas to fusion plasmas.

Recently, computer modeling and simulation has emerged in an effective tool that complements laboratory experiments and analytic models. Plasma simulation codes [65]-[68] have acquired a high level of sophistication and are routinely used in the design of plasma reactors in the semiconductor industry. Furthermore, the difficulty in achieving well-defined experimental conditions and the limited diagnostic techniques available for small scale discharges, favor the investigation of meso/nano scale systems with simulation tools. Given these experimental challenges, computer simulations provide an alternative method of analysis of microplasmas, contributing to the advance in our current understanding of the underlying physics. The development of simulation techniques is an ongoing process over a decades with rapid growth occurring over the last decade.

Plasma simulation codes can be roughly divided into: fluid (or hydrodynamic), particle-in-cell (PIC) and hybrid methods. Fluid simulation proceeds by numerically solving magnetohydrodynamic equations of continuous fluid involving assumed transport coefficients. [69, 70]. Kinetic models, on the other hand, consider more detailed model with particles interacting through the electromagnetic field, achieved either by solving kinetic equations or by particle simulation. PIC simulations take advantage of the collective behavior of charged particles in plasmas and model the kinetics of various species by simulating a reduced number of particles [71, 72]. Kinetic simulations but still retain some of their advantages, several researchers have used hybrid schemes, i.e., combinations of continuum and kinetic simulations [73, 74].

In this review an overall presentation of different types of discharges will be illustrated comparing experimental, simulation and/or theoretical results. The influence of the various parameters on the breakdown mechanism will be discussed. Beside results for the gaps of the order of a few centimeters, this review will be primary focused on the studies of microdischarges i.e. on the effect of the strong electric field generated in microgaps on the discharge characteristics. Experimental, theoretical and simulation techniques that we used to obtain the breakdown voltage curves and volt-ampere characteristics in various gas discharges in microgaps will be described in details. We would like to note that among various simulation techniques that can be employed in simulations of microdischarges, our results were obtained by using Particle-In-Cell (PIC) and Particle-In-Cell/Monte Carlo (PIC/MC) code [75], while some discharge parameters were calculated using Bolsig++ code [76]. The importance of the role of field emission and vapor arc has been demonstrated for gaps smaller than  $5 \mu\text{m}$ , leading to the description of the "modified" Paschen curve. The obtained simulation results confirm that one possible mechanism responsible for the reduction of the breakdown voltage in microgaps is the increase of the secondary electron yield due to the quantum tunneling of electrons from the metal electrodes into the gas phase and the other is the field induced emission. The high electric fields obtained in small gaps combined with the lowering of the potential barrier seen by the electrons in the cathode as ion approaches lead to ion-enhanced field emission. In addition, discharge parameters and coefficients necessary for determination of the breakdown characteristics in microdischarges have been determined, which still remains very difficult task.

## 2 Electrical breakdown of gases

Two mechanisms of the electrical breakdown in the gases are known: the avalanche and the streamer mechanisms. In the early 1950's a lot of efforts have been made to determine whether there is a stage in the development of a pre-breakdown current where the streamer process takes over from the Townsend amplification process [77]. Most of the papers on this topic have been studied of either the spatial growth to breakdown of small ionization currents [78] or of the temporal growth of a pre-breakdown discharge [79].

Generally speaking, for the breakdown to occur, two criteria must be satisfied: there must be suitably placed initiatory electrons and a mechanism of ionization must occur to produce amplification of the ions or electrons which compensate the loss by diffusion. The Townsend mechanism by which successive ionizations of gas molecules induce the gas breakdown, explains the process satisfactorily at large separations. However, avalanches can not be built up in the same way at micrometer separations so the gas breakdown is initiated by the secondary emission process rather than processes in the gas [80].

Electrical breakdown always begins with the multiplication of some primary seed electrons in cascade ionization when accelerated by the electric field. After this initial stage the following development of the discharge depends on several parameters such as the gas composition, the pressure, distance between the electrodes, frequency of the applied field and geometry of the system. For sufficient low pressures the mean free path of the electrons is long and the initial avalanche proceeds until the plasma is generated in the whole discharge gap. For relative high pressure the mean free path of the electrons is reduced and the avalanche ionization can generate a great number of electrons giving rise to a localized space charge which propagates in the discharge gap creating a thin conductive channel named streamer.

The theories that are usually used for the explanation of the electrical breakdown can be roughly divided into four categories [81]. In the so called "Clump" theories the breakdown is initiated by a particle or "clump", which becoming detached from one electrode, then crosses the gap between the electrodes and strikes on the other electrode with sufficient energy to trigger a breakdown. According to the "Interaction" theories, chain reactions involving electrons, positive ions, negative ions, and photons cause a rapid rise in pre-breakdown current which increases until breakdown of the gap occurs. The main assumption under the "Cathodic" theories is that field emission of electrons from the cathode produces sufficient amount of electrons in the gap to cause breakdown. Finally, "Anodic" theories assume the existence of a beam of electrons emitted from the cathode. This beam impinges upon the anode, producing effects there which ultimately lead to the breakdown.

On the other hand, the special conditions of the electrical breakdown include the corona breakdown, the breakdown in long discharge gaps of non-uniform fields, the lightning discharges and the laser-induced breakdown. Some objections to the above mentioned mechanisms of the electrical breakdown led to the development of 'streamer theory of breakdown' described in [82, 83].

### 3 Townsend's breakdown mechanism

Townsend breakdown mechanism is based on the generation of successive secondary avalanches to produce breakdown. Figure 3.1 illustrates the electron impact ionization of the neutral gas molecules that starts initiate the avalanche processes and amplifying the initial current  $I_0$  due to and external source. The initial electrons generated from an external source are accelerated by the electric field  $E$  in the gap  $d$  and reach the anode unless they are lost on the way by ion recombination or interaction with the chamber wall. The electric current  $I$  in the circuit is proportional to the number of charged species which reach the electrodes and initially increases with increasing the applied voltage  $U$ . At a certain voltage, electrons and ions reach the electrodes and the current reaches a saturation value  $I_0$  and ceases to depend on  $U$ . At this point the discharge is non self-sustaining, i.e. the discharge depends on the presence of the external sources, as can be seen from in Figure 3.2).

The electron impact ionization of neutral gas molecules leads to the avalanche process and amplification of the initial current  $I_0$  due to the external source. It is convenient to describe the ionization in the avalanche by the Townsend ionization coefficient  $\alpha$  that express the electron production per unit length:

$$\frac{dn_e}{dx} = \alpha n_e. \quad (3.1)$$

Solving the previous equation, we obtain expression for the electron density  $n_e$  at the distance  $x$  from the cathode:

$$n_e(x) = n_{e0}e^{\alpha x}, \quad (3.2)$$

where  $n_{e0}$  is the initial electron density created by the external sources. If the electron losses due to recombination and attachment to electronegative molecules are neglected,

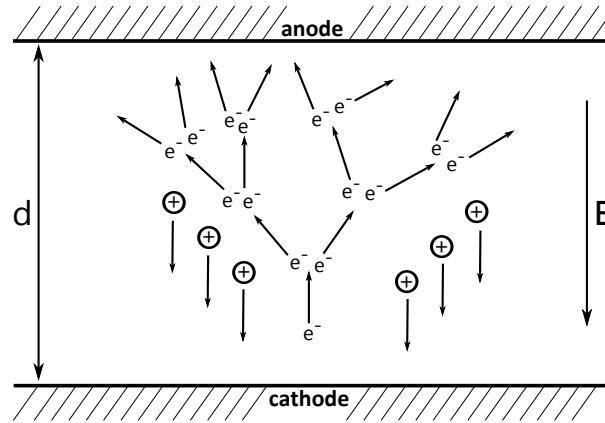


Fig. 3.1. Electrical breakdown in a gap between the electrodes  $d$  when a constant electric field  $E = U/d$  is applied.

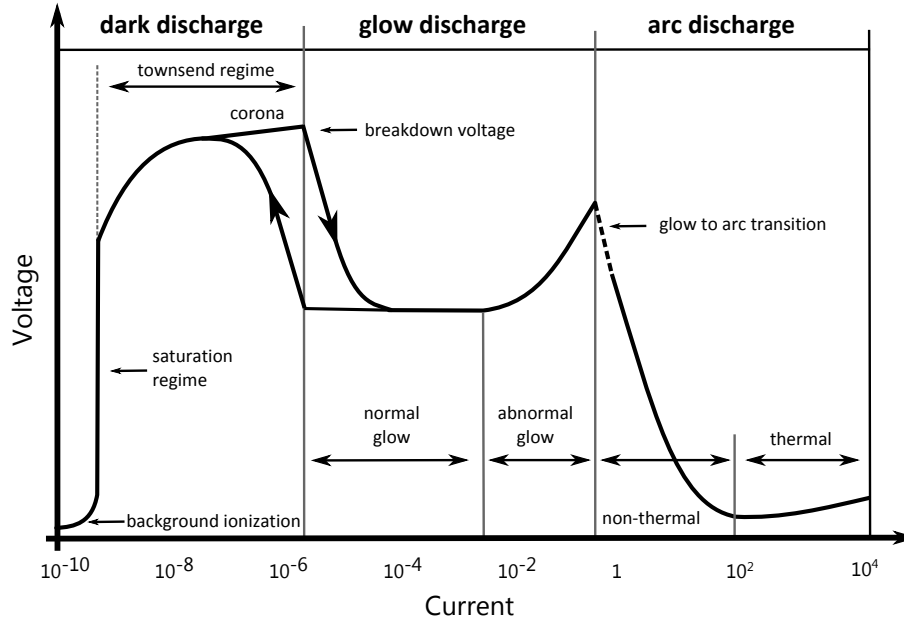


Fig. 3.2. Different electrical discharge regimes over a wide range of current.

the current at the anode is equal to:

$$I = I_0 e^{\alpha d}, \quad (3.3)$$

where  $I_0 = q_e n_{e0}$  and  $q_e$  is charge of the electron. The primary process of electron impact ionization creates  $n_{e0}(e^{\alpha d} - 1)$  ions during the avalanche propagation. Ions reach the cathode and can generate  $\gamma n_{e0}[e^{\alpha d} - 1]$  electrons in the process of secondary electron emission. The secondary emission yield  $\gamma$  depends on cathode material, state of the surface and the ion energy. Including the secondary emission process, the current  $I$  is given by the Townsend formula:

$$I = \frac{I_0 e^{\alpha d}}{1 - \gamma[e^{\alpha d} - 1]}. \quad (3.4)$$

The transition from non-selfsustaining to self-sustaining discharge is controlled by the denominator in Equation (3.4). If  $\gamma[e^{\alpha d} - 1] < 1$  the discharge is still non self-sustaining, but when it approaches to unity the current grows to infinity, the breakdown occurs and the discharge becomes self-sustaining. The simplest relation for the breakdown condition is:

$$\gamma[e^{\alpha d} - 1] = 1, \quad (3.5)$$

indicating that each primary electron generated in the initial avalanche and lost at the anode is replaced by another electron generated by secondary emission at the cathode which

represents a steady self-sustained current. Figure 3.2 demonstrates that regions appear over a wide range of operating conditions and are very characteristic of the normal glow discharge. Various regions of the normal glow discharge are: *Cathode*- the electrically conductive metal whose secondary electron emission coefficient plays a significant role in the discharge formation; *Aston dark space*- the space immediately beyond the cathode surface and is thin and dark with strong electric field and a negative space charge due to the slow electrons accelerating from the cathode surface. This region is dark since the electrons coming off the cathode have not enough energy to result in any visible excitations; *Cathode glow*- the region with a relatively high ion number density and depending on the gas can be often seen reddish or orange in air due to emissions by excited atoms sputtered off the cathode surface or due to positive ions moving towards the cathode. The length of this region depends on the pressure and type of gas; *Cathode dark space*- also known as the Crookes/Hittorf dark space has a moderate electric field, a positive space charge and relatively high ion density. *Cathode region*- the region where the electrons are accelerated to high enough energies to result in ionizing collisions and avalanches in the negative glow and beyond; *Negative glow*- the brightest region of the entire discharge. This region has relatively low electric field and is long as compared to the cathode glow and brighter on the cathode side. Almost all the current in this region is carried by the electrons because the electrons accelerated from the cathode region produce intense excitation and ionization in the negative glow region resulting in its brightness; *Faraday dark space*- the region where the electron energy is very low as a result of high activity in the negative glow region; *Positive column*- the region is a long, quasi-neutral uniform glow with small electric field; *Anode dark space*- is the anode sheath between the anode and the anode glow with negative space charge due to the electrons traveling from the positive column to the anode, and has a higher electric field than the positive column. The electrons are pulled out of the positive column by the anode; *Anode glow*- the bright region at the anode end of the positive column, brighter than the positive column but can not always be observed; *Striations*- traveling waves or stationary perturbations in the electron number density which occur in partially ionized gases.

### 3.1 Paschen law

The basic ideas under the Townsend's theory are that secondary electron production at the cathode induced by ion impact compensates the loss of electrons at the anode and thereby enables self-sustained discharge. In addition it is assumed that the growth of electrons between two electrons may be described by ionization coefficient that is defined for fully relaxed electric field. Paschen's Law describes the Townsend breakdown mechanism in gases. The significant parameter is  $pd$  - the product of the gap distance and the pressure. The Paschen curve represents a balance between the number of electrons lost by diffusion and drift in the interelectrode gap and the number of secondary electrons generated at the cathode [19]. In general, over a wide range of pressures and electrode separations, the probability of ionization per electron-neutral collision in the gas and the probability of the secondary electron production at the cathode by ion impact are proportional to the reduced electric field  $E/N$  (electric field over the gas number density ratio) and lead to the well-established  $pd$  similarity law [19]. Different gases exhibit

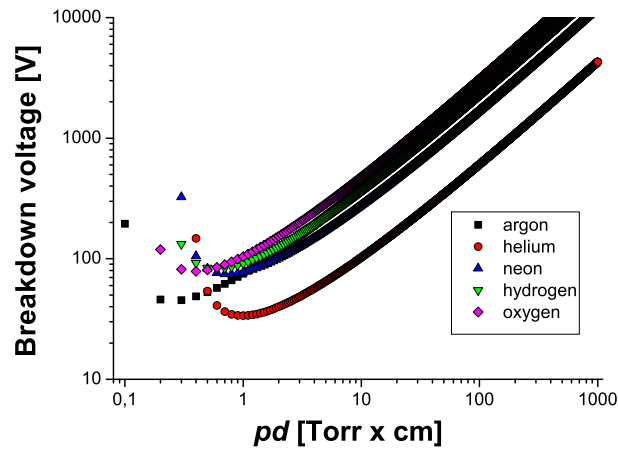


Fig. 3.3. The breakdown voltage curves for DC current discharges in argon, helium, neon, hydrogen and oxygen.

similar "Paschen" behavior as demonstrated in Figure 3.3 which show typical Paschen curves plotted for argon (squares), helium (circles), neon (up triangles), hydrogen (down triangles) and oxygen (diamonds). On the left side of the Paschen minimum, when the  $pd$  product is small, the electron mean free path becomes comparable or longer than the gap between the electrodes, so the electrons cannot gain enough energy to perform ionizations. Consequently, a higher voltage is required to assure ionization of enough gas molecules to start an avalanche. Of course, different gases will have different mean free paths for molecules and electrons since different molecules have different diameters. Noble gases like helium and argon are mono atomic and tend to have smaller diameters and therefore a greater mean free path length. More collisions will take place when the  $pd$  product is high and an electron will collide with many different gas molecules as it travels from the cathode to the anode.

#### 4 Ionization coefficients

In order to explain the exponential rise in the current, Townsend introduced the coefficient  $\alpha$  defined as the number of electrons produced by an electron per unit length of the path in the direction of field:

$$\alpha = \frac{1}{\lambda_i} = \frac{\omega_i}{\lambda_0}, \quad (4.1)$$

where  $\lambda_i$  and  $\lambda_0$  represent the electron mean path for the ionization and for any type of collision, respectively, while  $\omega_i$  is the probability that an electron travel the distance  $\lambda \geq \lambda_i$ . If the electron gained the energy  $eE\lambda_i = U_i$  on its free path, than the probability is:

$$\omega_i = \exp(-\lambda_i/\lambda_0) = \exp\left(-\frac{U_i}{eE\lambda_0}\right), \quad (4.2)$$

so the expression for the  $\alpha$  is:

$$\alpha = \frac{1}{\lambda_0} \exp\left(-\frac{U_i}{eE\lambda_0}\right), \quad (4.3)$$

where  $U_i$  is the ionization potential. Since the mean free path is inversely proportional to the gas pressure, the Townsend's first ionization coefficient can be related to the reduced electric field  $E/p$  (electric field to the gas pressure ratio) by the similarity law  $\alpha/p = f(E/p)$  [80]:

$$\alpha/p = A \exp\left(-\frac{B}{E/p}\right), \quad (4.4)$$

with coefficients  $A$  and  $B$  which values for various gases could be found elsewhere (see, for example, [80]). The  $\alpha/p = f(E/p)$  similarity law has been verified experimentally for wide ranges of gas pressures and electric field enabling a simplified mathematical treatment of the discharges. Actually, general form of the previous expression is:

$$\alpha/p = A_k \exp\left[-B_k(p/E)^{1/k}\right]. \quad (4.5)$$

The index  $k$  has been empirically determined to be 1 for the molecular gases and 2 for atomic gases [84, 85]. The differences between results obtained by using different  $k$  index is clearly visible from Figure 4.1.

It was found that the process of impact ionization in noble gases becomes significant at much lower values of the reduced electric field as compared to that for molecular gases. This is associated with the greater ionization energy of an electron in avalanche in a noble gases. Consequently, small admixtures of molecular gases have a strong influence on the ionization coefficient. Based on the experimental data for low pressure discharges [86, 87], the empirical formula for the ionization coefficient has been proposed [80]:

$$\alpha/p = A \left(\frac{E}{p}\right)^{a-b\ln(E/p)} - B \left(\frac{E}{p}\right)^{2[a-b\ln(E/p)]}, \quad (4.6)$$

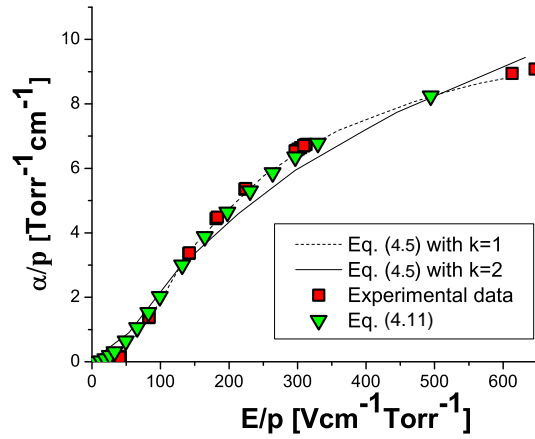


Fig. 4.1. The ionization coefficient for argon. Dash and solid curves are plotted by using expression (4.5) with  $k=1$  and  $k=2$ , respectively. Red squares correspond to the experimental data taken from [84], while the green down triangle were obtained by using formula (4.11).

Gas	$A$	$B$	$a$	$b$
He	$1.645 \cdot 10^{-4}$	0	3.065	0.242
Ne	$1.584 \cdot 10^{-4}$	0	3.052	0.230
Ar	$-4.140 \cdot 10^{-3}$	$-1.57 \cdot 10^{-4}$	1.5	0.0984
Kr	$-4.160 \cdot 10^{-3}$	$-1.56 \cdot 10^{-4}$	1.5	0.0963

Tab. 4.1. The values of the constants involved in the expression (4.6).

with the values of the constants  $A$ ,  $B$ ,  $a$  and  $b$  given in Table 4.1 [80]:

In addition to expressions (4.4) and (4.6), there are other formulas for the ionization coefficients. For example, for nitrogen, several empirical expressions also could be used [80]:

$$\alpha/p = A \exp\left(B \frac{E}{p}\right), \quad (4.7)$$

for  $E/p = 20 - 36 \text{ V}/(\text{cm} \cdot \text{Torr})$ ,  $A = 3.3 \cdot 10^{-7} (\text{cm} \cdot \text{Torr})^{-1}$  and  $B = 0.265 \text{ cm} \cdot \text{Torr}/\text{V}$ .

$$\alpha/p = A \left(\frac{E}{p} - B\right)^2, \quad (4.8)$$

for  $E/p = 45 - 150 \text{ V}/(\text{cm} \cdot \text{Torr})$ ,  $A = 1.2 \cdot 10^{-4} \text{ cm} \cdot \text{Torr}/\text{V}^2$  and  $B = 30 \text{ V}/(\text{cm} \cdot \text{Torr})$ .

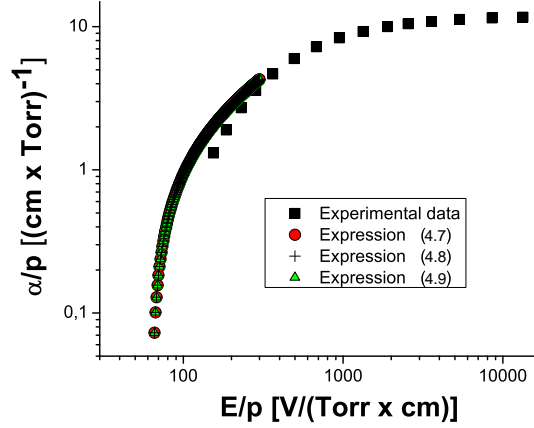


Fig. 4.2. The ionization coefficient versus the ratio  $E/p$  for nitrogen. Values estimated from the experimental data taken from [88] (red symbols) are compared with the values obtained by using expressions (4.7)-(4.9).

$$\alpha/p = \sqrt{\frac{AE}{p}} - B, \quad (4.9)$$

for  $E/p=200 - 1000 \text{ V}/(\text{cm} \cdot \text{Torr})$ ,  $A=0.21 \text{ (V} \cdot \text{cm} \cdot \text{Torr)}^{-1}$  and  $B=3.65 \text{ (cm} \cdot \text{Torr)}^{-1}$ . In Figure 4.2, circles, crosses and triangles correspond to the values obtained by using expressions (4.7)-(4.9), respectively. Obviously, expressions (4.7)-(4.9) provide similar values for the ionization coefficients for nitrogen and a good agreement with the results of measurements [88] (solid squares)

Based on the measurements performed at the pressure of 760 Torr [89], there is another formula that can be used for the ionization coefficient for argon [80]:

$$\alpha/p = A \exp\left(-\frac{B}{\sqrt{E/p}}\right), \quad (4.10)$$

with  $A = 33 \text{ (cm} \cdot \text{Torr)}^{-1}$  and  $B = 22.7 \text{ V}^{1/2}/(\text{cm} \cdot \text{Torr})^{1/2}$ .

Finally, the ionization coefficients can be also determined by using expressions (taken from [90]), for the gas and gas mixtures, respectively:

$$\frac{\alpha}{N} = \sum_i A_i e^{-B_i/(E/N)}, \quad (4.11)$$

$$\left[\frac{\alpha}{N} \left(\frac{E}{N}\right)\right]_m = \sum_z x_z \left[\frac{\alpha}{N} \left(\frac{E}{N}\right)\right]_z, \quad (4.12)$$

where  $x_z$  represents the fraction of the gas  $z$  in the mixture.

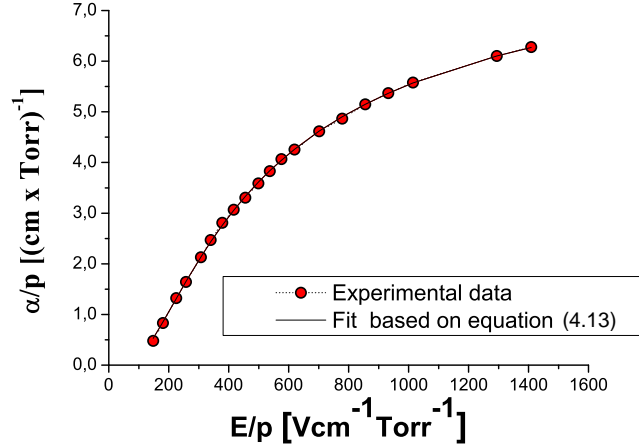


Fig. 4.3. The influence of the magnetic field on the ionization coefficient versus the ratio  $E/p$  for argon. Values estimated from the experimental data taken from [92] (symbols) are fitted by using expression (4.13).

#### 4.1 Ionization coefficient in the presence of magnetic fields

Since the mass of the positive ion is many times greater than the mass of the electron, the magnetic field affects the electron motion much stronger than the motion of the positive ions. Therefore, the expression for the first Townsend's coefficient in the presence of both electric and magnetic fields is given by [91]:

$$\left(\frac{\alpha}{p}\right)_{E,B} = A_k \sqrt{1 + C\left(\frac{B}{p}\right)^2} \times \exp\left[-B_k \left(\frac{p\sqrt{1 + C(B^2/p^2)}}{E}\right)^{1/k}\right], \quad (4.13)$$

where  $B$  is label for the the magnetic flux density. With knowledge of  $\lambda_e$ -the electron mean free path in the gas at the pressure of 1 Torr and the electron velocity  $v$ ,  $C$  can be determined in accordance to:

$$C = \left[\frac{e}{m_e} \cdot \frac{\lambda_e}{v}\right]. \quad (4.14)$$

Applicability of the expression (4.13) is demonstrated in Figure 4.3 via fitting the experimental data taken from [92].

## 5 Cathode processes-secondary effects

Cathode plays an important role in gas discharges by supplying electrons for the initiation, maintenance and completion of a discharge. In a metal, under normal condition, electrons are not allowed to leave the surface as they are tied together due to the electrostatic force between the electrons and the ions in the lattice. The energy required to knock out an electron from a Fermi level is known as the work function and is a characteristic of a given material. There are several methods of giving electrons the needed energy to escape the lattice, such as by applying strong electric fields or bombarding the metal with high energy photons. In addition, the metal may be heated to a point at which electrons break free from the surface. Various ways in which this energy can be supplied to release the electron as illustrated in Figure 5.1 and corresponding voltage-current curve shown in Figure 5.2.

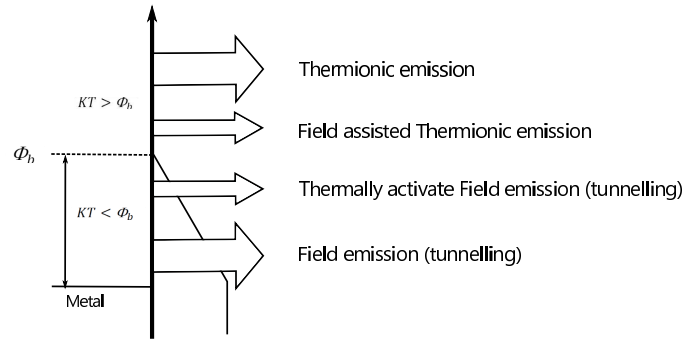


Fig. 5.1. Various mechanisms of the electron ejection from the surface.

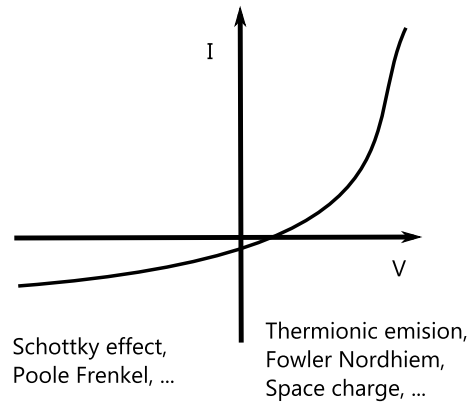


Fig. 5.2. Typical voltage-current characteristics illustrating different mechanisms of the electron ejection.

### 5.1 Thermionic emission

At room temperature, the conduction electrons of the metal do not have sufficient thermal energy to leave the surface. But if the metals are heated above the temperature of 1500° K, the electrons will receive energy from the violent thermal lattice in vibration sufficient to cross the surface barrier and leave the metal. When electrons are emitted from a surface due to heating, the process is known as thermionic emission, and this is the subject of interest in the experiment. If the emitted electrons do not escape the region around the emitter, a buildup of negative charge results; this effect is known as space charge, and it hinders the production of free electrons. However, when a sufficiently large potential difference exists between the emitter and some collection surface, electrons will be pulled away from the emitter and reduce this space charge effect, which results in a current flow between the emitter (cathode) and collector (anode). Richardson provided an expression for the saturation current density  $J_s$  (today known as the Richardson-Dushman equation) which describes the current flow between the cathode and the anode [93]:

$$J_s = AT^2 \exp(-W/kT), \quad (5.1)$$

with  $A = 4\pi m_e k^2/h^3$ .  $W$  is the work function and  $k$  is the Boltzmann constant. The expression (5.1) indicates that the saturation current density increases with decreasing the work function and increasing the temperature. The gas present between the electrode affects the thermionic emission as the gas may be absorbed by the metal and can also damage the electrode surface due to continuous impinging of ions.

### 5.2 Schottky effect

Generally speaking, increase in the discharge of electrons from the surface of a heated material by application of an electric field that reduces the value of the energy required for electron emission. If a strong electric field is applied between the electrodes, the effective work function of the cathode decreases in accordance to:

$$W' = W - \varepsilon^{3/2} E^{1/2}. \quad (5.2)$$

The expression for the saturation current density is then [94]:

$$J_s = AT^2 \exp(-W'/kT), \quad (5.3)$$

which is known as Schottky effect. Calculations have shown that at room temperature the total emission is still low even when the fields of the order of  $10^5$  V/cm are applied. However, if the field is of the order of  $10^7$  V/cm, the emission current is much larger than the calculated thermionic value. This can be explained only through quantum mechanical analysis at these high surface gradients, the cathode surface barrier becomes very thin and quantum tunneling of electrons occurs which leads to field emission even at room temperature.

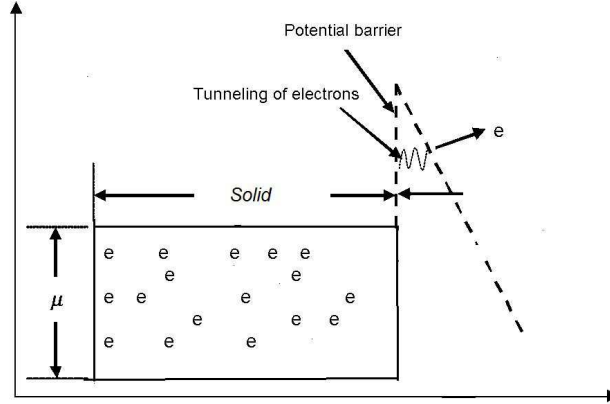


Fig. 5.3. Schematic view of electrons tunnel through a barrier in the presence of a high electric field.

### 5.3 Field emission

Field emission can be described as the ejection of electrons from the surface at high-field strengths representing the most important factor in breakdown initiation in small gaps. Since field emission can occur at temperature that is much lower than required for thermionic emission, it is also sometimes called cold-cathode emission. In the absence of a strong electric field, an electron must acquire a certain minimum energy to escape through the surface of a given material, which acts as a barrier to electron passage. However, if the material is placed in an electric circuit that renders it strongly negative with respect to a nearby positive electrode (i.e., when it is subjected to a strong electric field), the work function is lowered to such an extent that some electrons will have a sufficient energy to leak through the surface barrier as presented in Figure 5.3. The resulting current of electrons through the surface of a material under the influence of a strong electric field is called the field emission (FE) or Fowler-Nordheim tunneling [95].

The field emission process has some advantages as compared to the thermionic emission and photoemission, such as dramatically higher efficiency, less scatter of emitted electrons, faster turn on times, and compactness. The field emission, which limits the maximum operating voltage for microdevices, can be applied as an electron source in flash memory, electron microscopy, MEMS systems, and FE displays. In our studies, we focused on the effect of FE on the breakdown voltage in microgaps. The field emission and its effect on the breakdown phenomena in microdischarges will be discussed in details latter.

## 6 Secondary electron emission processes

It was recently shown that the basic assumption of Townsend's theory that ions produced the secondary electrons is correct only in a very narrow range of conditions [96]. In other words the basic phenomenology of Townsend's theory is in error except in a very narrow  $E/N$  range, yet this theory is the foundation for employing the binary collision data in plasma modeling. According to the revised Townsend's theory secondary electrons are produced in collisions of ions, fast atoms, metastable atoms or photons with the cathode or in gas phase ionization of neutrals [96]. The secondary emission process is described by the secondary emission yield defined as the number of secondary electrons emitted per incident particle.

The yield depends on the work function, the value of the reduced electric field, the energy of the incident particles, etc. If the work function of the cathode surface is low, under the same experimental conditions will produce more emission. Also, the value of the yield is relatively small at low value of the reduced field  $E/N$  and will increase with increase in  $E/N$ , since at higher values of  $E/N$ , there will be more number of positive ions and photons of sufficiently large energy to cause release of secondary electrons upon impact on the cathode surface.

### 6.1 Electron impact secondary emission

The electron bombardment of surface can lead to the emission of electrons from the materials (termed secondary electron emission) by different processes as illustrated in Figure 6.1. The backscattered electrons are reflected after experiencing elastic collisions with the valence electrons of the surface material, and are at approximately the electron energy of primary electrons. The inelastically reflected electrons possess energies between 50 eV and the primary electron energy. True secondaries with energies below 50 eV are produced by the ionization of the atoms within the material by primary and reflected electrons [97].

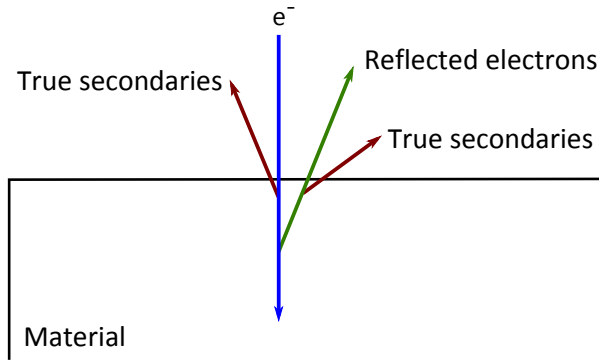


Fig. 6.1. Mechanism of the secondary electron emission due to bombardment with primary electrons.

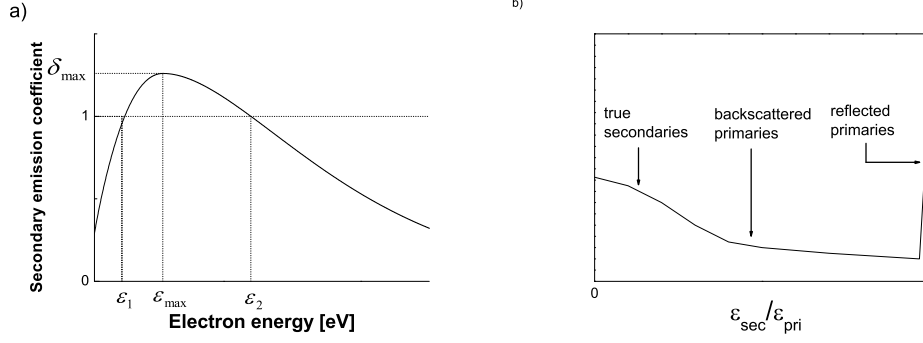


Fig. 6.2. a) The secondary emission coefficient  $\delta$  versus the impact energy of electrons at the normal incident to the surface [100, 101]. b) Spectrum that contains reflected, backscattered electrons true secondaries.

Electron impact secondary emission process is defined as the ratio of the emitted electrons normalized to the initial flux and represented by the secondary emission coefficient  $\delta$  [98]. The flux of secondary electrons depends on the energy of the particles, on the surface potential and on the material properties of the charged grains. Secondary electron emission (SEE) from electron bombardment of materials can have adverse effects at the plasma-material interface, where SEE from the wall decreases the potential at the wall and hence increases the electron loss to the wall, heating of the wall, and cooling of the plasma [99].

Various models that describe the secondary electron emission by electron impact exist. Among them, we used the Vaughan's model for the secondary emission coefficient that includes both its energy and angular dependence [100, 101]:

$$\delta(\varepsilon, \theta) = \delta_{\max 0} \left( 1 + \frac{k_{s\delta} \theta^2}{2\pi} \right) (we^{1-w})^k. \quad (6.1)$$

$w$  is the normalized energy given by:

$$w = \frac{\varepsilon - \varepsilon_0}{\varepsilon_{\max 0} (1 + k_{sw} \theta^2 / 2\pi) - \varepsilon_0}, \quad (6.2)$$

where  $\varepsilon$  is the incident energy of a particle and  $\theta$  is the angle of incidence measured perpendicular to the surface normal,  $\delta_{\max 0}$  is the peak secondary emission coefficient corresponding to the energy  $\varepsilon_{\max}$  and the normal incidence. The exponent  $k$  can be determined from a curve-fit analysis,  $\varepsilon_0$  is the secondary emission threshold,  $k_{s\delta}$  and  $k_{sw}$  are the surface-smoothness parameters. Electrons gain energy from the electric field and strike the surface with impact energy  $\varepsilon$ . When this energy lies between energies  $\varepsilon_1$  and  $\varepsilon_2$ , the first and the second cross over energy, respectively, of the secondary electron yield curve, the secondary emission coefficient  $\delta$  is greater than unity and a net gain of secondary electrons occurs, as can be seen from Figure 6.2a. Schematic view of the spectrum due to electron impact is shown in Figure 6.2b.

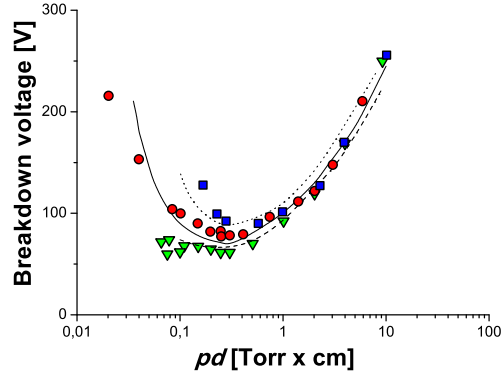


Fig. 6.3. Simulation results for the RF breakdown in argon obtained with:  $\delta_m = 0$  (squares-dotted line),  $\delta_m = 2.4$  (circles-solid line) and  $\delta_m = 4, 8$  (down triangles-dashed line). Solid line corresponds to the results provided by global model [102].

The importance of the proper choice of the secondary coefficient  $\delta$  strongly affects the simulation results as demonstrated Figure 6.3 via comparison between the simulation results obtained with different  $\delta$  coefficients (symbols) and the theoretical prediction based on global model (solid curve) [102]. Presented results, clearly show that the secondary emission is essentially unimportant in the righthand branch of the breakdown curve, where breakdown is dominated by volume processes, but plays a large role at low  $pd$  values.

## 6.2 Ion induced secondary electron emission

The electrons released at the cathode travel the whole distance to the anode and produce more ionization than the electrons created en route. Consequently, the onset of breakdown is determined by the gamma-effects at the cathode. The secondary electron emission from the cathode surface is usually attributed only to the ions which is possible in the case of breakdown studies as all relevant fluxes are proportional to the electron flux. The secondary electron emission from a surface under the action of an ion is described by the coefficient quantifying the number of secondary electrons produced at the cathode per ion impact usually known as the yield per ion  $\gamma_i$ . This coefficient depends on the cathode material and the gas. The dependence of the yield per ion on the ratio  $E/p$  for different gases is depicted in the Figure 6.4 [103]. In line with the expectations, the yield of helium has the highest values, while oxygen and oxygen-containing gases have low yields. Even more, it was suggested that the yield per ion depends on the incident angle too, as can be observed from the Figure 6.5. But as already pointed out, the contribution of the ions to the secondary electron production is dominant only in a narrow range of the reduced electric field [96].

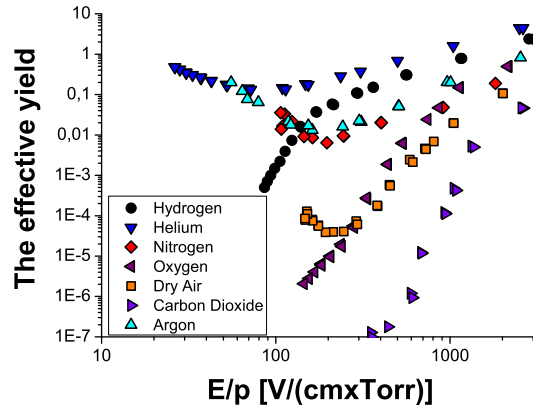


Fig. 6.4. The yield per ion as a function of the ratio  $E/p$  for hydrogen, helium, nitrogen, oxygen, dry air, carbon dioxide and argon [103].

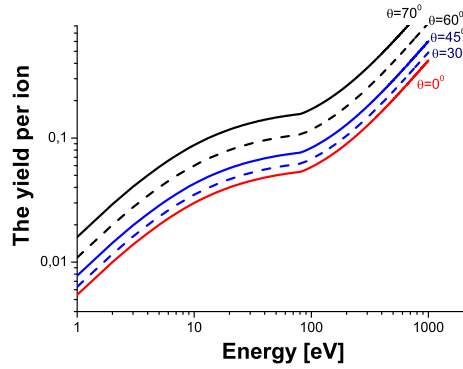


Fig. 6.5. The yield per ion as a function of the ion energy in accordance to the expression for argon taken from [96], for several angles of ion incidence on a metal electrode.

### 6.2.1 Ion-enhanced field emission

The previously described mechanism of the ion induced secondary electron emission, however, is not applicable in the presence of high electric fields [104, 105]. When the gap size is of the order of a few micrometers or smaller, electric fields near the cathode are sufficiently large and therefore the electrons can be liberated from the surface by quantum mechanical tunneling. Furthermore, as an ion approaches the cathode, it could narrow the potential barrier seen by the electrons in the metal resulting in an ion-enhanced

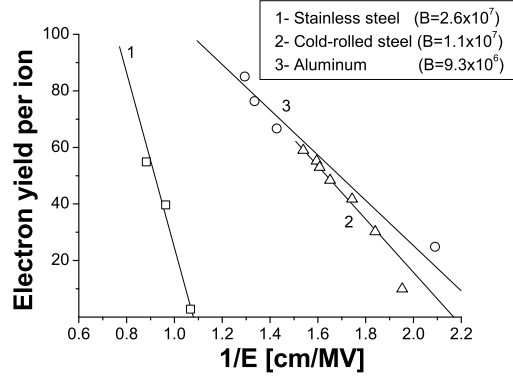


Fig. 6.6. The yield per ion versus the inverted electric field. Experimental data are shown by symbols, for electrodes of: 1- stainless steel, 2- conventional steel and 3- aluminum (see, for example, Ref. [104]).

electron field emission [104]. The effective secondary electron emission coefficient  $\gamma_i$  that incorporates this ion-enhanced field emission in microgaps can be written in the form [106]:

$$\gamma = \gamma_i + K \exp(-B/E), \quad (6.3)$$

where  $K$  and  $B$  are material and gas dependent constants and  $E$  is the electric field near the cathode. The first term on the right side of (6.3) corresponds to the ion induced secondary emission, while the second term corresponds to the emission due to the strong electric field. Actually, the exponential dependency of the field emission on the electric field strength pins the electric field during breakdown to the threshold for field emission and allows for a rapid reduction of the breakdown voltage as the gap size is reduced. Figure 6.6 clearly demonstrates that when the electric field in the cathode region becomes larger than the threshold value given by  $B$  and the secondary electron emission coefficient increases rapidly. From the slopes of the straight lines the constant  $D$  was found to be equal to 26, 11 and 9.3 MV/cm for stainless steel, conventional steel and aluminum, respectively [104].

### 6.3 Secondary emission model in a crossed electric and magnetic fields

It was found that the presence of the magnetic field affects the second Townsend's coefficient. The expression that describes the variation of the coefficient  $\gamma$  with magnetic field has been suggested by Sen and Gosh [107]:

$$\gamma_{E,B} = \gamma - \frac{A'E}{p} \left( 1 - \frac{1}{\sqrt{1 + C \frac{B^2}{p^2}}} \right), \quad (6.4)$$

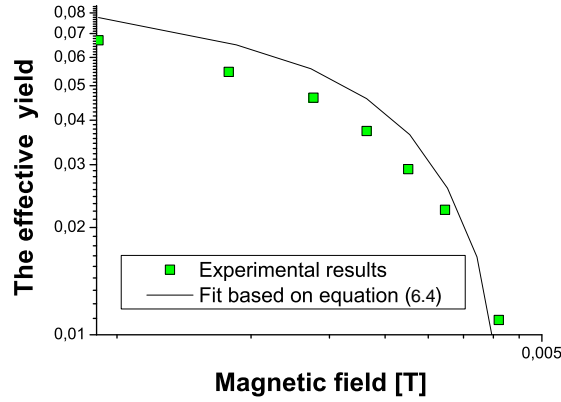


Fig. 6.7. The effect of the magnetic field on the effective yield. Experimental data taken from [108] are fitted in accordance with expression (6.4).

where  $\gamma$  is the effective yield of secondary electrons in the absence of a magnetic field. Variation of the effective yield in a crossed electric and magnetic fields can be observed in Figure 6.7. Experimental results taken from [108] (symbols) are compared with the theoretical predictions obtained by using expression (6.4) (curves) for the dependence of coefficient  $\gamma$  on the ratio  $E/N$  in air. A good agreement between them indicates that the expression (6.4) suggested by Sen and Gosh [108] fits well the experimental data for the secondary electron yield.

#### 6.4 Secondary emission model in a magnetic field parallel to the electric field

An empirical expression for the secondary electron yield when a magnetic field is parallel to the electric field has been obtained by fitting the experimental data taken from [92]:

$$\gamma_{E,B} = \gamma - \frac{C' E}{p} \left( 1 - \frac{1}{\sqrt{1 + C'' \frac{B^2}{p^2}}} \right), \quad (6.5)$$

where labels have the same meaning as in the previous expressions and  $C'$  and  $C''$  are appropriate coefficients. The dependence of the secondary emission coefficient  $\gamma$  on the ratio  $E/N$  (in this case  $E/p$ ) in argon is shown in In Figure 6.8. The experimental data obtained in the absence of the magnetic field (open squares) and in the presence of the magnetic field (open circles) are compared with the theoretical values achieved by using equation (6.5) (solid lines). Values of the constants  $C'$  and  $C''$  were calculated as proposed in Refs. [91, 109], by using transport parameters from [91]. A good agreement between theoretical and experimental results noticeable from Figure 6.8 leads to the conclusion that the empirical formula (6.5) fits well the experimental data.

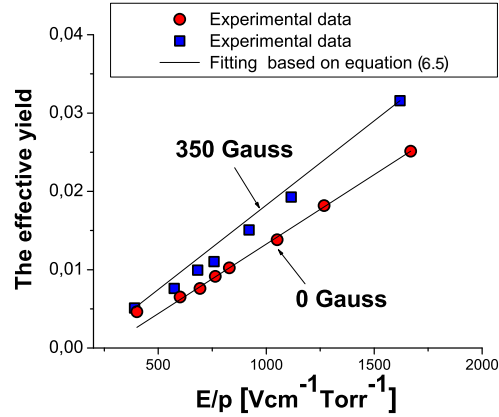


Fig. 6.8. The variation of the secondary electron yield with the ratio  $E/p$  in argon under the action of a parallel electric and magnetic field of 350 Gauss.

## 7 Types of discharges

Transforming an insulator into a conductor requires the introduction of free or mobile charges to carry the electric current. Depending on the medium in which this occurs, the breakdown can be classified to: *Dielectric breakdown*- breakdown in solid insulators, usually destroying part of the insulator (making holes in it), or the breakdown of high voltage ceramic insulators. *Breakdown of gases*- usually involving electron avalanches caused by electron-impact ionization of the ambient neutral gas. *Townsend discharges*- electron avalanches started by chance ionization events, and regenerated by secondary processes (e.g., photon or ion bombardment of the cathode that releases secondary electrons at the cathode). *Glow discharges*- basically Townsend discharges (electron avalanches and secondary emission) that produce enough charge to alter the applied field, but not enough current to dominate the applied voltage. *Arcs*- electron avalanches that create enough current and charge to support more efficient mechanisms of charge production. *Vacuum breakdown*- arcing in vacuum, caused by interaction of the electric field and the vacuum walls (or electrodes in the vacuum) perhaps stimulated by the energy gain of charged particles that travel unhindered in the electric field.

In general, the discharges should scale according to:  $E/N$ -electric field to gas number density ratio- proportional to the energy gain from the field between two collisions;  $pd$ -product pressure (or  $Nd$  by using gas number density) times the characteristic distance between two electrodes- proportional to the number of collisions;  $jd^2$ -current density multiplied by the geometric dimension to the square- describing the space charge effects;  $\omega/N$ -frequency normalized by gas number density for scaling of the RF discharges. Depending on the type of the electric field, the mechanism of the electrical breakdown is different, requiring different theoretical approaches and thereby expressions for its calculations.

### 7.1 Direct current discharges

In DC discharges, the secondary electron production at the cathode surface plays a key role in discharge maintenance [85]. For the discharge to be self-sustainable, the generation of electron-ion pairs must be sufficient to make up for the loss of charged particles lost by collision processes such as attachment and drift and diffusion to the walls. At low pressures the ionization process becomes ineffective since the probability for electron-neutral collisions is too small, whereas at high pressures elastic collisions prevent the electrons from gaining the energies sufficient for ionization and also ion-neutral collisions are responsible for increasing of the ion losses to the walls. Therefore, for a fixed gap an optimum pressure for gas breakdown exists.

Under the action of a DC field an electron is accelerated by the electric field until its collision with a gas molecule. The direction of the motion is then reoriented almost randomly. Most of the kinetic energy gained during the acceleration period is kept during the scattering process, since the mass of the molecule is large as compared to that of the electron. After collision, the electron is accelerated or decelerated by the field, depending on the direction of the electron velocity relative to the field. The randomly directed velocity immediately after collision does not contribute to the flow of electrons along the field direction, except the component of produced by acceleration in the field. The kinetic energy of the electrons is built up through successive accelerations until the loss of energy by elastic and inelastic collisions and diffusion equals the gain of energy from the field. The motion consists of a large random and a small drift component. The energy transferred to the electrons is a function of the ratio  $E/N$ , which determines the energy gained between the collisions.

It is important to note that the continuous loss of the electrons to the anode represents a rather severe loss to the system. It renders the DC discharge quite inefficient, since the lost electrons have to be constantly replenished by the release of secondary electrons into the system, i.e. by ion bombardment of the cathode. Thus, the plasma densities obtained in the dc discharge are rather modest.

Using a simple exponential analytic form for the ionization coefficient, DC breakdown criterion leads to the following expression for the breakdown voltage [84, 85]:

$$U_{DC} = \frac{B_k^k pd}{(\ln A_k/\Gamma_k + \ln pd)^k}, \quad (7.1)$$

where  $p$  is the gas pressure in units of Torr,  $d$  represents the interelectrode separation expressed in cm and  $\Gamma_k = \ln(1 + 1/\gamma)$ ,  $\gamma$  is the second Townsend's coefficient.

From the equation (7.1) it is easy to derive expressions for the minimum and inflection point of the Paschen curve. It can be noticed that ratio of the  $pd$  values at the inflection point and the minimum  $(pd)_{\text{infl}}/(pd)_{\text{min}} = e$  is independent of  $k$ . On the other hand, the ratio of the voltage values in these points  $V_{\text{infl}}/V_{\text{min}} = e[k/(k+1)]k$ , where  $e$  is the base of natural logarithm. The minimum on the Paschen curve occurs when the electronic mean free path is just barely sufficient to allow electrons to gain the ionization energy. The various values of the  $pd$  and the voltages at the breakdown voltage curves that correspond to various gases are listed in Table 7.1 [110]. The pressure dependence of the breakdown voltage in argon is shown in Figure 7.1. Symbols represent results of

Gas	$pd_{\min}$	$U_{\min}[\text{V}]$
Air	0.55	352
Nitrogen	0.65	240
Hydrogen	1.05	230
SF <sub>6</sub>	0.26	507
Carbon Dioxide	0.57	420
Oxygen	0.70	450
Neon	4.0	245
Helium	4.0	155

Tab. 7.1. Values of the  $pd$  product and the voltage at the minimum of the Paschen curves for various gases [110].

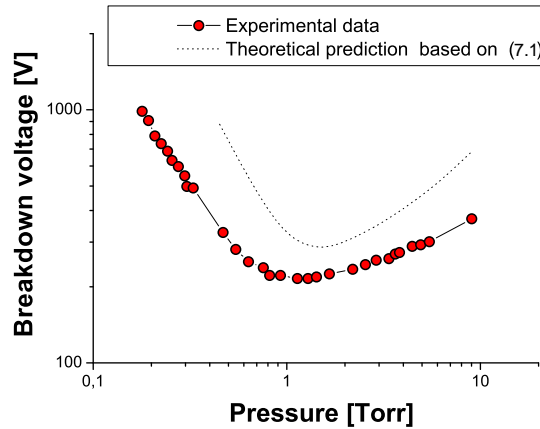


Fig. 7.1. DC breakdown voltage versus the pressure in argon for the interelectrode separation of 1.1 cm. Experimental data [22] (symbols) are compared with the theoretical values obtained by (7.1).

measurements [22], while the dot curve corresponds to the theoretical prediction obtained by using expression (7.1). There are similar trends between experimental and theoretical results. The lower breakdown voltage obtained in measurements could be attributed to the fact that in the expression (7.1) a constant yield  $\gamma$  is used.

Besides the breakdown voltage, there are other important aspects of the DC discharge like Volt-ampere characteristics that should be predicted by the Townsend's theory and having in mind that the procedure of determination of Paschen curves is valid only in the low current limit. Failure of the standard Paschen law observed in microgaps indicates that Paschen curves do not offer sufficient information regarding very small separations and therefore it is necessary to determine Volt-ampere characteristics of the DC discharges, especially in microgaps.

### 7.1.1 Expression for the air

Combination of the spark criterion in uniform fields:

$$\alpha d = k = \left(1 + \frac{1}{\gamma}\right), \quad (7.2)$$

and the a quadratic relation between the ionization coefficient  $\alpha/p$  and the reduced field  $E/p$  ( $E/N$ ) :

$$\frac{\alpha}{p} = C \left[ \frac{E}{p} - \left( \frac{E}{p} \right)_c \right]^2, \quad (7.3)$$

provide expression:

$$\frac{K}{dp} = C \left[ \frac{E}{p} - \left( \frac{E}{p} \right)_c \right]^2, \quad (7.4)$$

where  $\left( \frac{E}{p} \right)_c$  is the minimum value of the electric field at which the effective ionization begins,  $p$  is the pressure and  $C$  is the constant. Relation (7.4) can be re-written as:

$$\frac{E}{p} = \left( \frac{E}{p} \right)_c + \left( \frac{K/C}{pd} \right)^{1/2}, \quad (7.5)$$

$$\frac{U}{dp} = \left( \frac{E}{p} \right)_c + \left( \frac{K/C}{pd} \right)^{1/2}, \quad (7.6)$$

$$U_b = \left( \frac{E}{p} \right)_c pd + \left( \frac{K}{C} \right)^{1/2} \sqrt{pd}. \quad (7.7)$$

Substituting assumed values for  $E_c = 24.36 \text{ kV/cm}$ ,  $K/C = 45.16 \text{ (kV)}^2$  for the air and the pressure of 1 atm in (7.7), we obtain an empirical relation:

$$U_b = 6.72\sqrt{pd} + 24.36 \cdot pd, \quad (7.8)$$

for the breakdown voltage expressed in kV. In Figure 7.2 we compare results obtained by using the expression (7.8) (squares) and experimental data taken from [111] (diamonds). There is a good agreement between them. The lower theoretical values for the breakdown voltages as compared to the experimental data [111] are attributed to the experimental conditions.

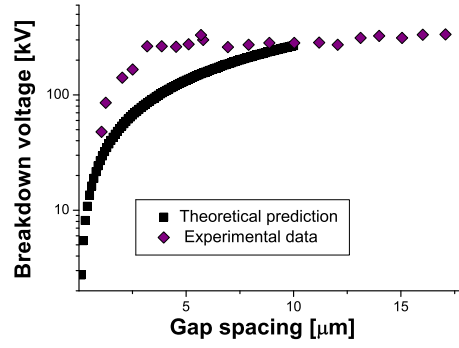


Fig. 7.2. The breakdown voltage against the gap size for the air the pressure of 760 Torr. Experimental data [111] (diamonds) are compared with the theoretical values obtained by (7.8) (squares).

## 7.2 Radio frequency discharges

In Radio Frequency (RF) discharges, the electrons can attain in the RF field oscillatory energy from the applied field. The field induced motion is interrupted by the collisions, which occur often during RF cycle. When a collision takes place, the electron oscillatory motion is disturbed and its momentum is randomized. RF discharge can be considered as a diffusion-controlled one i.e. a discharge in which the diffusion loss is the primary loss mechanism. In the steady state, there is balance between the electron loss and the ionization processes, which can be mathematically expressed as [112]:

$$\frac{\nu_I}{D} = \frac{1}{\Lambda_D^2}, \quad (7.9)$$

where  $\nu_I$  is the ionization frequency,  $D = T_e/m_e\nu_c$  is the diffusion coefficient with the collision frequency labeled by  $\nu_c$  and  $\Lambda_D$  represents the diffusion scale length.

In the Kihara theory the fundamental processes of the molecular kinetic theory of electrical discharges consider the collisions between gas molecules and charged particles. The basic idea under the theory adopt a proper molecular model for the molecular collisions and their fundamental quantities such as the effective cross sections for the elastic scattering, excitations and ionizations [113]. In RF field, the main equation that should be solved in order to obtain the expression for the RF breakdown is [113]:

$$\frac{\partial n}{\partial t} = \nu n + D \frac{\partial^2 n}{\partial z^2} - KE_0 \cos \omega t \frac{\partial n}{\partial z}, \quad (7.10)$$

where  $n$  and  $KE_0 \cos \omega t$  are the electron density and the drift velocity of electrons, respectively. Solving the equation (7.10) with boundary condition for  $n(z, t)$  :

$$n(\pm d/2, t) = 0, \quad (7.11)$$

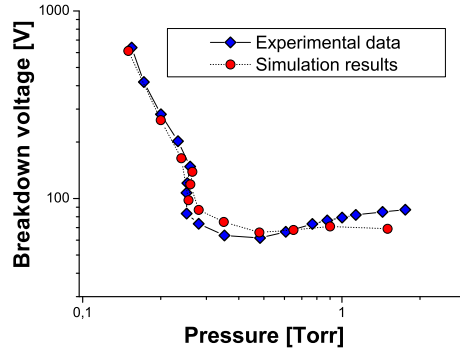


Fig. 7.3. The RF breakdown voltage as a function of the gas pressure in argon at 13.56 MHz. Diamonds represent the experimental data taken from [114], while circles correspond to the simulation results [112].

we obtain a solution periodic in time. On the other hand, the explicit form of the molecular model is [113]:

$$\exp\left(\frac{mc_i^2}{2kT_e}\right) = \frac{3\sigma\lambda}{c_i} \left(\frac{Nd}{\pi}\right)^2 \left(1 - \frac{2KE_0}{\omega d}\right)^2, \quad (7.12)$$

where  $K = q_e/(mN\lambda)$  and  $q_e$  are the electron mobility and its charge, respectively. Finally, the condition for the RF gas breakdown is given by the Kihara equation [113]:

$$\exp\left(\frac{B_0 p}{2E}\right) = A_1 p d \left(1 - \frac{E/B_0 p}{C_2 d/\lambda}\right) \quad (7.13)$$

where  $E = E_{RF}/\sqrt{2}$  is the effective RF field,  $p$  is the gas pressure,  $d$  is the distance between the electrodes,  $\lambda$  is the vacuum wave length of the RF field and finally,  $A_1$ ,  $B_0$  and  $C_2$  are constants for the breakdown gas and their values can be found, for example, in Ref. [113].

A good agreement between the experimental data [114] (diamonds) and the simulation results (circles) [112] is demonstrated in Figure 7.3. Following the procedure described in [115], based on the breakdown voltages and pressures measured at the minimum and the inflection point, molecular constants could be determined:

$$C_2 = \frac{\lambda(1-Z)}{2d(2Z-1)}, \quad (7.14)$$

$$A_1 = \frac{1 + (\lambda/2C_2 d)}{(pd)_{\min}} \exp\left(1 + \frac{\lambda}{2C_2 d}\right), \quad (7.15)$$

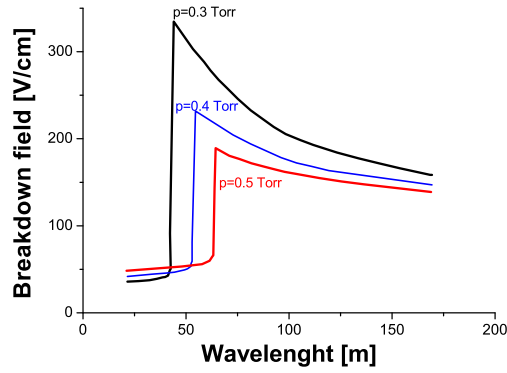


Fig. 7.4. The pressure dependence of the RF breakdown voltage [112, 116].

$$B_0 = \sqrt{2} \left( \frac{U_{RF}}{pd} \right)_{\min} \left( 1 + \frac{\lambda}{2C_2 d} \right), \quad (7.16)$$

where:

$$Z = \frac{(U_{RF}/pd)_{\text{infl}}}{(U_{RF}/pd)_{\min}}. \quad (7.17)$$

In order to provide clear picture of the RF breakdown, the so called oscillation amplitude limit  $x_0$  of a charged particle will be define [116]:

$$x_{0e,i} = \frac{e_{e,i} E_0}{m_{e,i} \omega (\nu_{ce,i}^2 + \omega^2)^{1/2}}, \quad (7.18)$$

where  $\nu_c$  is the collisions frequency and  $\omega$  is the angular frequency of the applied RF field. The increase in the breakdown field as the wavelength is reduced is shown in Figure 7.4. At very low frequencies, both electrons and ions respond to the RF fields quickly and the oscillation amplitude for both species is less d the oscillation amplitude limit (7.18). Both species therefore reach the electrodes at the ends. The plasma in this case is also sustained by secondary electrons produced by the ion bombardment of the cathode, taking into account that the cathode and anode alternate in each half cycle of the wave, so that the electron-ion bombardment also switches round each half cycle.

As the frequency is increased further, the ion response to the RF field becomes more sluggish, although the electrons follow the RF fields without any difficulty. Thus, the ion current to the cathode decreases so that both the ion bombardment and the secondary electron production go down. To compensate for the reduced secondary electron production, the breakdown field rises. With further increase of the frequency, the oscillation amplitude for the ions falls below the oscillation amplitude limit so there is a sharp reduction in the ion bombardment of the cathode, along with a concomitant decrease in the

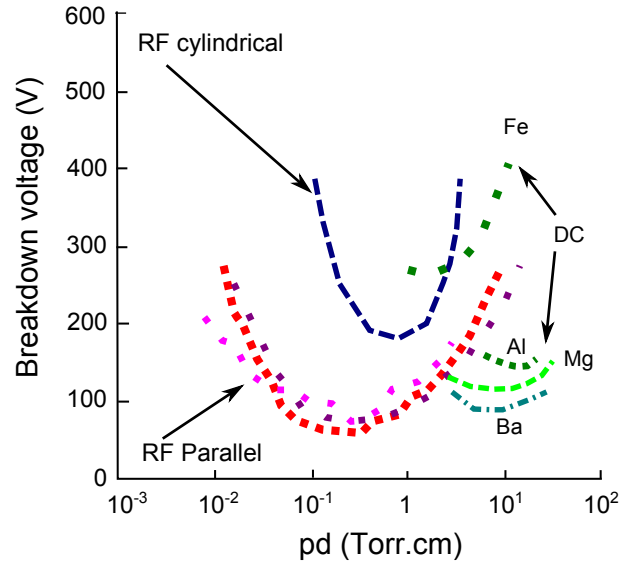


Fig. 7.5. The breakdown voltage curves for RF and DC discharges according to [117].

secondary electron production. The electron response, however, is still almost instantaneous and the electron loss is large. Due to the acute shortage of secondary electrons, the discharge is difficult to maintain and the breakdown field strength rises steeply. At the same time, the time-averaged plasma potential attains moderately high values in order to draw out the ions from the plasma to preserve the charge neutrality. The increased ion bombardment of the electrodes enhances secondary electron production that partially compensates, the electron loss from the system.

With further raise of the frequency, the maximum excursion of electrons also goes below oscillation amplitude limit, which leads to the heavy loss of electrons so the breakdown field strength drops abruptly by a very large amount. In addition, the time-averaged plasma potential also reduces sharply, since the ion currents are no longer needed for maintaining the discharge.

The breakdown voltage curves corresponding to the measured breakdown voltages for RF discharges in argon and DC discharges with various electrode material are presented in Figure 7.5 [117]. Several curves are plotted: data measured for a capacitively coupled parallel plate RF system with various inter-electrode distance of 2 cm (open red triangles), 5 cm (solid red circles) and 10 cm (open red circles). For DC discharges, data for iron, aluminum, manganese and beryllium electrodes are shown by solid green squares, solid green losanges, solid green circles and beryllium solid green triangles, respectively.

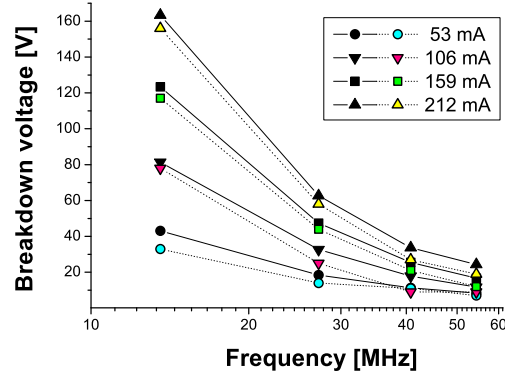


Fig. 7.6. RF breakdown voltage plotted against RF frequency. Calculations were performed at the gas pressure of 250 mTorr and the electrode separation of 2 cm for different values of the RF current. Simulation results shown by colored symbols are compared with the experimental results (solid symbols) [118].

### 7.2.1 Frequency effect

We also performed calculations keeping the RF current constant and varying the frequency in the range from 13.56 Hz to 54.4 MHz at the gas pressure of 250 mTorr. Simulation results (open symbols) and the available experimental data [118] (solid symbols) are compared in Figure 7.6. Similar trends are observed in simulation and experimental results while simulation results are systematically lower than the experimental data. Although the same gap size is used in both cases, the temperature and electrode materials used in the experiments are unknown [118] leading to the differences between simulations and experimental results.

As expected, the breakdown voltage decreases with an increasing frequency and both experimental and simulation results indicate that the breakdown voltage is a strong function of the frequency for all the current levels. For the three highest current values, the frequency dependence of the breakdown voltage can be expressed as  $U_{\text{RF}} \sim f^{-1.4}$  ( $f$  is the frequency of the RF field). For the lowest current value, the relation between the RF breakdown voltage and the frequency is  $U_{\text{RF}} \sim f^{-1.2}$ .

### 7.3 Combined fields

Simultaneous application of a RF and a small DC fields induces an enhanced drift of electrons to the electrodes causing increase of the loss of the charged particles and consequently, the discharge may be ignited only at higher voltages and gas pressures. Applying a large DC voltage, DC field contributes to the ionization of the gas molecules and causes the ion induced secondary electron emission from the cathode surface, the discharge may be ignited at lower gas pressure and RF voltages. Applying a weak DC electric field

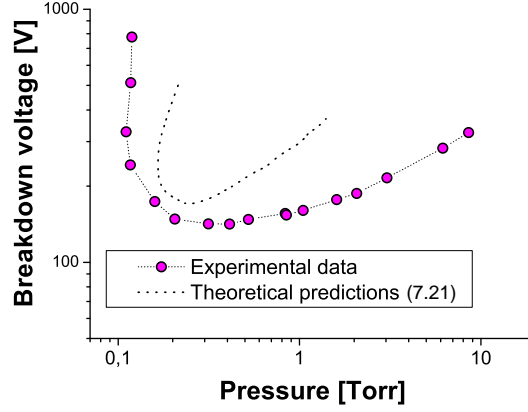


Fig. 7.7. The RF breakdown voltage against the gas pressure for the simultaneous action of RF field at 13.56 MHz and DC electric field of 100 V [120].

to the RF discharges mainly increases the losses of charged particles, while strong DC field contributes to the gas ionization and therefore an increase in the number of charged particles [115].

When a small DC field is applied to RF discharges the electrons are lost both by diffusion and drift. The breakdown condition can be formulated mathematically by considering these processes and the derived expression is taken from Ref. [119]:

$$\nu_I/D = 1/\Lambda_{DC-RF}^2, \quad (7.19)$$

where  $\Lambda_{DC-RF}$  denotes a modified diffusion length given by relation:

$$1/\Lambda_{DC-RF}^2 = 1/\Lambda_D^2 + \left[ E_{DC}/(2D/\mu) \right]^2, \quad (7.20)$$

where  $\mu$  is the mobility coefficient. The only difference between the breakdown condition in the combined field as compared to that in the pure RF field is the substitution of a modified diffusion length  $\Lambda_{DC-RF}$  for the characteristic diffusion length.

Figure 7.7 displays the pressure dependence of the RF breakdown voltage when additional DC voltage of 100 V is applied to RF discharges at 13.56 MHz. The available experimental data (solid symbols) agree well with the theoretical curves obtained by using equation (7.21) (dot curve). Due to the fact that the secondary electron emission from the electrodes is not included in the Kihara equation, theoretical values of the RF breakdown voltages are much higher than the experimental data.

The equation governing RF breakdown with a superimposed weak DC electric field can be written in the form [115]:

$$\left( A_1 p d - \frac{A_1 \lambda U_{RF}}{\sqrt{2} B_0 C_2 d} \right) \exp \left( -\frac{B_0 d p}{\sqrt{2} U_{RF}} \right) = \left\{ 1 + \left[ \frac{U_{DC}}{U_{RF}} \left( A_1 p d - \frac{A_1 \lambda U_{RF}}{\sqrt{2} B_0 C_2 d} \right) \left( \frac{c_i \rho}{2\sigma} \right)^{1/2} \right]^2 \right\}^{1/2}, \quad (7.21)$$

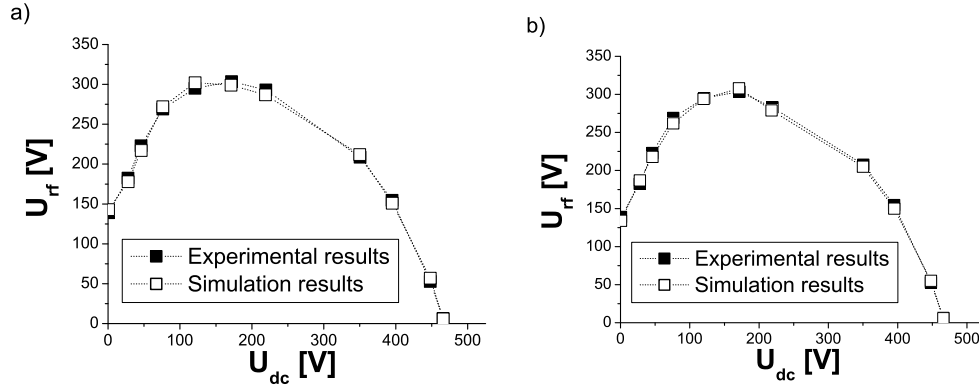


Fig. 7.8. The RF breakdown voltage against the DC voltage in combined discharges in argon at the interelectrode separation of 2.3 cm and the gas pressure of: a) 1 Torr and b) 5 Torr.

where  $\sigma$  and  $\rho$  represent molecular constants given in [113]. In derivation of the Equation (7.21), the drift-diffusion approach has been employed and therefore the effective RF field is assumed to be  $E = E_{RF}/\sqrt{2}$  where  $E_{RF}$  is the peak value of the electric field.

As an illustration Figure 7.8 shows comparison between our simulation results (open symbols) and the available experimental data [115] (solid symbols) for the RF breakdown voltage versus the DC voltage for the gap spacing of 2.3 cm and two different values of the gas pressure. As can be observed, the RF breakdown voltage increases with increasing DC voltage applied to it. At large DC voltages, DC field contributes to the ionization of gas molecules by electrons and the RF breakdown voltage reaches the maximum value. After that, it decreases due to ion-induced secondary electron emission from the electrodes approaching zero when the dc voltage becomes equal to the breakdown potential of the dc discharge. Ion impact secondary electron production represents the additional source of charged particles and the discharge may be ignited at lower gas pressures and RF voltages.

#### 7.4 Microwave discharges

Microwave-induced plasma are related to frequencies in the range from 300 MHz to 10 GHz. At such high frequencies, ions are not capable to respond to the electric field and electrons are "trapped" in an oscillatory motion within the inter-electrode gap. When this occurs, the electron loss is dominated by the diffusion and a significant reduction of the breakdown voltage is observed as compared to the DC case. The basic physics involved in the microwave-induced breakdown process can be shortly described as rapid

growth in time of the free-electron density in the device, when the ionization rate caused by microwave accelerated free electrons hitting the neutral gas particles or device walls exceeds the rate of electron losses. Several different models of the microwave breakdown exist with varying degree of accuracy. The kinetic approach offers a very detailed description of the mechanism and represents the basis on which other models rely. The great details in descriptions, however, makes the kinetic approach very complex and more useful in pure physical research with simplified geometry. On the other hand, fluid models enable description with enough details that can be used in large classes of research [121].

In microwave electric fields, gas breakdown can be regarded as an avalanche-like increase in time of the free-electron density caused by the ionization of the neutral gas molecules by free electrons accelerated to high energies by microwave field. Electron-neutral collisions are characterized by the collision frequency  $\nu_c$ . The continuity equation describing the time evolution of the electron density  $n_e$  is [122]:

$$\frac{\partial n_e}{\partial t} = \nabla(D_e \nabla n_e) + \nu n_e, \quad (7.22)$$

where the electron diffusion coefficient is denoted by  $D_e$  and the net production rate of the electrons per electron by  $\nu$ . In the fluid approach based on the diffusion-controlled model, the microwave breakdown for a non-attaching gas can be determined as the balance between the ionization rate and the loss rate of the electrons. It is easy to derive the expression for the the pressure dependence of the breakdown electric field  $E_r$  [123]:

$$E_r = \frac{\varepsilon \sqrt{\omega^2 + \nu_c^2} \exp\left(Bp \sqrt{\omega^2 + \nu_c^2} / (\nu_c E_r)\right)}{\nu_c \Lambda^2 A p}, \quad (7.23)$$

with already explained constants  $A$  and  $B$ . The transcendental Equation (7.23) can be solved numerically using the pressure dependence of the diffusion coefficient and characteristic frequencies from [124]:

$$D \approx \frac{10^6}{p} [cm^2/s], \quad (7.24)$$

$$\nu_i \approx 5 \cdot p \cdot 10^{11} \cdot \exp\left[-73(E_{eff}/p)^{(-0.44)}\right] [1/s], \quad (7.25)$$

$$\nu_c \approx 5 \cdot p \cdot 10^9 [1/s]. \quad (7.26)$$

In the phenomenological approach, the Kihara equation governs the microwave-induced breakdown [113]:

$$\frac{B_0 p}{E} \left[1 + \left(\frac{C_1 d / \lambda}{A_1 p d}\right)^2\right]^{1/2}, \quad (7.27)$$

with molecular constants  $A_1$ ,  $B_0$  and  $C_1$  determined from the measured breakdown voltages in order to achieve the proper agreement between the experiment and theory. According to equation (7.27), the breakdown field  $E$  is expressed in terms of the  $pd$

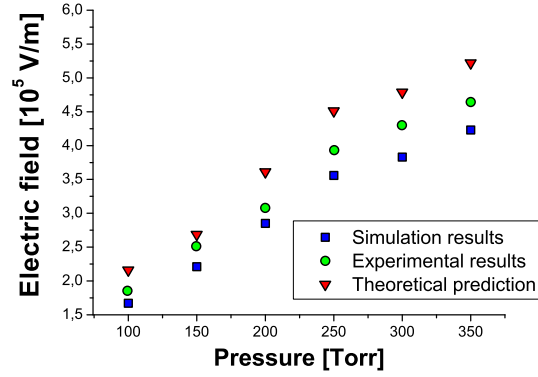


Fig. 7.9. Breakdown field strength as a function of the pressure for an argon microwave discharge at 2.45 GHz. Experimental data [62] (circles) are compared with the simulation (squares) and theoretical results based on expression (7.27) (triangles).

product and the ratio  $d/\lambda$  (gap length to the vacuum wavelength of the applied field expressed in cm).

Combination of analytical and experimental studies described in [124], is based on the experimental data of the breakdown voltages at low pressures and their extrapolation over a wide range of pressures. The breakdown electric field is expressed as:

$$E_b = 3,75 \cdot p \left[ 1 + \left( \frac{2\pi f}{\nu_c} \right)^2 \right]^{1/2} \left( \frac{D}{p\lambda_D^2} + 6.4 \cdot 10^4 \right)^{3/16}, \quad (7.28)$$

where  $E_b$  represents the real rms electric field in volts per centimeter, whereas the characteristic length  $\lambda_D$  (in  $\text{cm}^2/\text{s}$ ) determines the curvature of the breakdown voltage curve,  $p$  is pressure in torr,  $\nu_c$  is the collision frequency of electrons with gas particles in  $\text{s}^{-1}$  and  $f$  is the frequency of the microwaves in Hz.

Figure 7.9 shows the breakdown electric field strength versus the pressure in argon for the gap size of  $600 \mu\text{m}$  at frequency 2.45 GHz. Comparison with experimental data (circles) shows a good agreement with both simulation results (squares) and results obtained by using Kihara equation (7.27) (triangles). In microwave discharges, the breakdown voltage strongly depends on the the frequency and decreases with increasing the frequency as can be resolved from from Figure 7.10.

### 7.5 The effect of the magnetic fields

The breakdown voltage in presence of magnetic field is always found to be higher than in the case when no magnetic field is present for all values of the pressure. The pressure at which the breakdown voltage becomes a minimum increases gradually as the magnetic field is increasing. The presence of the magnetic fields do not influence the motion of

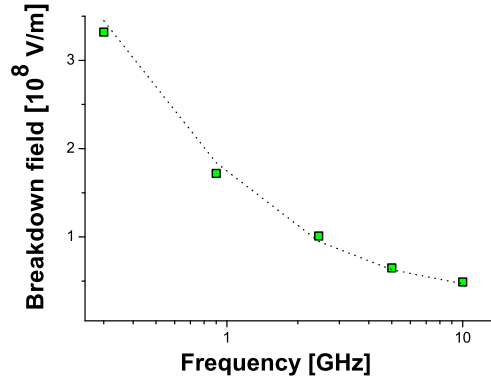


Fig. 7.10. Breakdown field strength as a function of microwave frequency in argon at the pressure of 7600 Torr by varying the frequency from 300 MHz to 10 GHz.

the ions as strong as electrons, because the mass of ions is many times greater than the mass of electrons. Therefore it can be assumed that the value of the electron yield per ion  $\gamma_i$  remains constant in the magnetic field and is equal to its value in the absence of a magnetic field [91], while the ionization coefficient changes in accordance to expression (4.13). Then, applying the sparking criterion the derived expression for the breakdown voltage in a crossed electric and magnetic fields is given by [91]:

$$U_{E,B} = \frac{B_k^k p d \sqrt{1 + C \frac{B^2}{p^2}}}{\left[ \ln A_k / \Gamma_k + \ln \left( p d \sqrt{1 + C \frac{B^2}{p^2}} \right) \right]^k}. \quad (7.29)$$

The expression (7.29) provides the pressure dependence of the breakdown voltage in the presence of both electric and magnetic field. From the condition  $dU_{E,B}/dp = 0$ , values of the gas pressure and the breakdown voltage at the minimum of the breakdown curve are found to be:

$$p_{\min} = \frac{\sqrt{e^{2k} \Gamma_k^2 - C d^2 B_k^2 A_k^2}}{A_k d}, \quad (7.30)$$

$$U_{\min} = \left( \frac{B_k}{k} \right)^k \frac{e^k}{A_k}. \quad (7.31)$$

The influence of the crossed electric and magnetic field on the breakdown voltage is demonstrated Figure 7.11. Simulation results obtained including the magnetic field (circles) are systematically lower than experimental data [125] (squares). Although, theoretical prediction based on the expression (7.29) (dot curve) are lower they have the same tendencies as both experimental and simulation results.

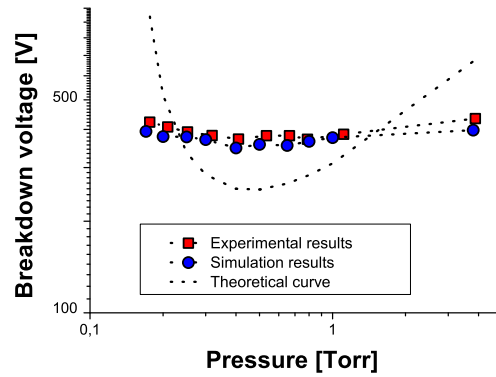


Fig. 7.11. The breakdown voltage as a function of the gas pressure in a crossed electric and magnetic field of 121 Gauss.

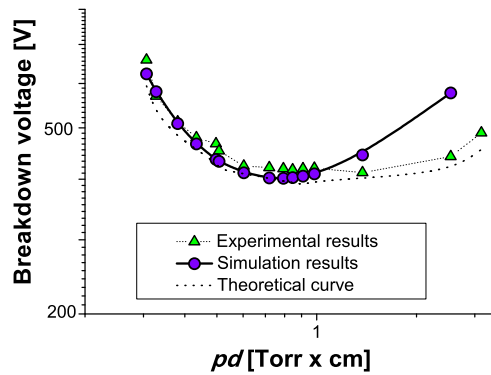


Fig. 7.12. The breakdown voltage versus  $pd$  product in the case of parallel electric and magnetic fields of 350 Gauss in argon.

When the electric and magnetic fields are parallel, simulation results are compared with the results of measurements published by Petraconi et al. [92] and shown in Figure 7.12. Experimental data (up triangles), results of calculations (squares) and results of phenomenological model represented by Equation (7.29) (dot curve) are in a good agreement.

## 8 Streamer mechanism

Based on the Townsend mechanism the electric discharge occurs due to the ionization of gas molecule by the electron impact and release of electrons from cathode due to positive ion bombardment at the cathode. As already pointed out, for  $pd > 100 \text{ Torr} \cdot \text{cm}$ , the Townsend breakdown cannot describe the discharge development. On the other hand, the Streamer theory originally developed by Raether [77] predicts the development of a spark discharge directly from a single avalanche.

Let us consider an avalanche in a uniform external field  $E$  between two plane electrodes. Let it be initiated by a single electron that leaves the cathode at the time  $t = 0$ . The  $x$ -axis is directed from a point on the cathode to the anode. The radial distance from the  $x$ -axis is denoted by  $r$ . The total numbers of electrons and ions increase as the avalanche moves forward in accordance to:

$$\frac{dN_e}{dx} = (\alpha - \eta)N_e, \quad \frac{dN_+}{dx} = \alpha N_e, \quad \frac{dN_-}{dx} = \alpha N_e, \quad (8.1)$$

$$N_e = \exp((\alpha - \eta)x), \quad N_+ = \frac{\alpha}{\alpha - \eta}(N_e - 1), \quad N_- = \frac{\alpha}{\alpha - \eta}(N_e - 1), \quad (8.2)$$

with ionization  $\alpha$  and attachment  $\eta$  coefficients. The electron density  $n_e$  can be expressed as:

$$n_e = (4\pi D_e t)^{-3/2} \exp \left[ -\frac{(x - v_d t)^2 + r^2}{4D_e t} + (\alpha - \eta)v_d t \right], \quad (8.3)$$

where  $v_d = \mu_e E$  and  $D_e$  are the drift velocity of the electrons and diffusion, respectively. The density of the electrons decreases with the distance and the radius of the sphere on which the density is  $e$ -times less than that at the center  $n_e(x_0, 0, t)$  is given by:

$$r_D = \sqrt{4D_e t} = \sqrt{\frac{4D_e x_0}{\mu_e E}} = \sqrt{\frac{4T_e x_0}{eE}}, \quad (8.4)$$

where  $x_0 = v_d t$  and  $\mu_e$  is the electron mobility. The ions remain almost fixed during the time of flight of the avalanche to the anode as can be observed from Figure 8.1. The positive ions density is [126]:

$$n_+(x, r, t) = \int_0^t \alpha v_d n_e(x, r, t') dt', \quad (8.5)$$

and taking into account equation for the density of electrons (8.3), we obtain:

$$n_+(x, r) = \frac{\alpha}{\pi r_a^2(x)} \exp \left[ \alpha x - \frac{r^2}{r_a^2(x)} \right], \quad (8.6)$$

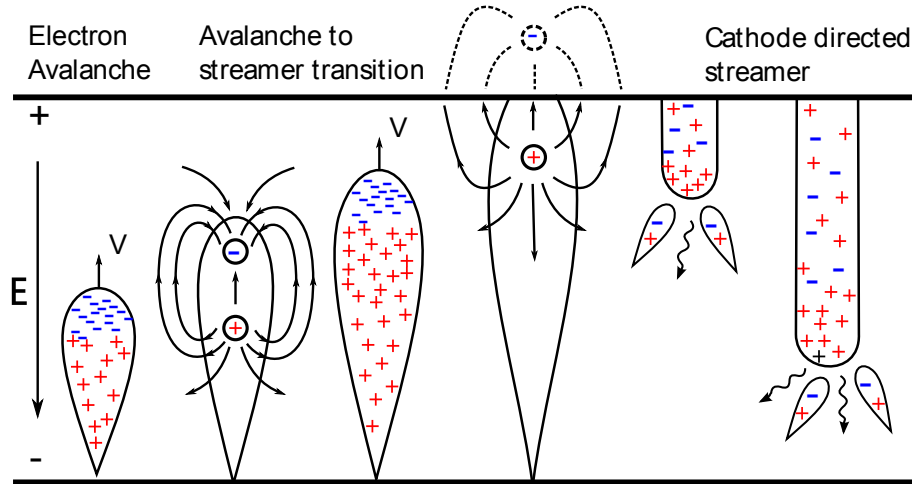


Fig. 8.1. Formation of the streamers.

where where  $r_a^2(x)$  is the avalanche radius defined by expression (8.4).

When the charge amplification factor  $\exp(\alpha x)$  is high, the production of a space charge with its own significant electric field takes place. This local electric field should be added to the external field  $E$ . Since the electrons are much faster than ions the electrons always run at the head of avalanche leaving the ions behind and thus creating a dipole with the characteristic length  $1/\alpha$  (mean distance for an electron before creating an ion) and charge  $N_e \sim \exp(\alpha x)$ . The fields in front of the avalanche head add up and give a field stronger than  $E$ . The fields in the zone between the centers of the space charges of opposite signs point in opposite directions and the resultant field is weaker than  $E$ . When the avalanche reaches the anode, the electrons sink into the metal and only the positive space charge of the ionic trail remains in the gap as depicted in Figure 8.1. At the electron absence, the total electric field is due to the external field, the ionic trail and also the ionic charge image in the anode. The resulting electric field in the ionic trail near the anode is less than the external electric field. The total electric field reaches the maximum value on the characteristic ionization distance. A strong primary avalanche amplifies the external electric field leading to formation of thin weakly ionized plasma channel, the so called streamer. The avalanche-to-streamer transformation occur, when the internal field of an avalanche becomes comparable with the external one i.e. when the amplification  $\alpha d$  is big enough.

At a relatively small discharge gaps, the transformation takes place only when the avalanche reaches the anode. Such a streamer is known as the cathode-directed or positive streamer. If the discharge gap and over-voltage are big enough, the avalanche-to-streamer transformation can take place quite far from anode. In this case the so called anode-directed or negative streamer is able to grow toward the both electrodes.

The cathode-directed streamer starts near the anode. The anode-directed streamer

occurs between electrodes, if the primary avalanche becomes strong enough even before reaching the anode. The streamer propagates in the direction of the cathode in the same way as cathode directed streamer. Mechanism of the streamer growth in direction of anode is also similar, but in this case the electrons from primary avalanche head neutralize the ionic trail of secondary avalanches as illustrated in Figure 8.1.

Again between the tail and the cathode the field is enhanced as illustrated in Figure 8.1. Due to the enhanced field between the head and the anode, the space charge increases, causing a further enhancement of the field around the anode. The process is very fast and the positive space charge extends to the cathode very rapidly resulting in the formation of a streamer and causing the breakdown process displayed in Figure 8.1. The anode-directed streamer occurs between electrodes, if the primary avalanche becomes strong enough even before reaching the anode. The streamer propagates in direction of cathode in the same way as cathode directed streamer. Similar mechanism takes place in the case of the streamer growth in direction of anode, although electrons from primary avalanche head neutralize the ionic trail of secondary avalanches. However, the secondary avalanches could be initiated here not only by photons, but also by some electrons moving in front of the primary avalanche. When the streamer channel connects the electrodes, the current may be significantly increased to form the spark or arc discharge which are characterized by high current and low voltage. This would lead to Joule heating of the gas and the generation of a thermal plasma [126].

In accordance with the experimental observations of the streamer phase of breakdown, several theoretical models of the process have been developed. Due to complexity of the process, all models are based on using assumptions and simplifications. The main assumption in model is quasimetallic ellipsoid body of the streamer placed in an external electric field with the streamer velocity [126]:

$$V = \mu_- E_0 \left( \frac{a}{R_0} \right) \left[ \ln \left( \frac{2}{e} \sqrt{\frac{a}{R_0}} \right) \right]^{-1}, \quad (8.7)$$

where  $R_0$  is the radius of the curvature of the streamer and  $a$  is the ellipsoid major semi-axis. In this mode, the streamer velocity is determined by the drift of electrons in an enhanced field, where enhancement factor depends on the ratio  $a/R_0$ .

### 9 Vacuum breakdown

The behavior of gases under low pressures and uniform and non-uniform fields and in particular the breakdown characteristics are covered in detail in work by Craggs and Meek [19]. Under very low pressures, the gaseous breakdown mechanism is dominated mostly by the electrodes, and is called the “Vacuum breakdown ”and is not affected much by the gases involved. As already pointed out, in a Townsend type of discharge, in a gas, the mean free path of the particles is small and electrons get multiplied due to various ionization processes and an electron avalanche is formed. In a vacuum of the order of  $10^{-5}$  Torr, the mean free path is of the order of few meters and thus when the electrodes are separated by a few mm an electron crosses the gap without any collision. Therefore, in a vacuum, the current growth prior to breakdown can not take place due to formation of electron avalanches.

Voltage breakdown in vacuum results from the interaction of the electric field and the electrodes. Vacuum is ideally the best insulator, with breakdown strengths of the order of  $10^4$  kV/cm. The breakdown voltage of a high vacuum is the voltage which when increased by a small amount will cause the breakdown that was held at that voltage for an infinite time. In practice, the breakdown is affected by many factors.

Electrons from the field emission are one of the possible reasons why the breakdown and sparks occur in a vacuum, which of course is not possible if one only considers the Townsend avalanche mechanisms for the gas phase and the surface ionization that are normally used to generate the Paschen curve. Regime of the vacuum breakdown can be clearly distinguished from the gas breakdown regime as presented in Figure 9.1.

The fundamental explanation of the vacuum breakdown related phenomena is pro-

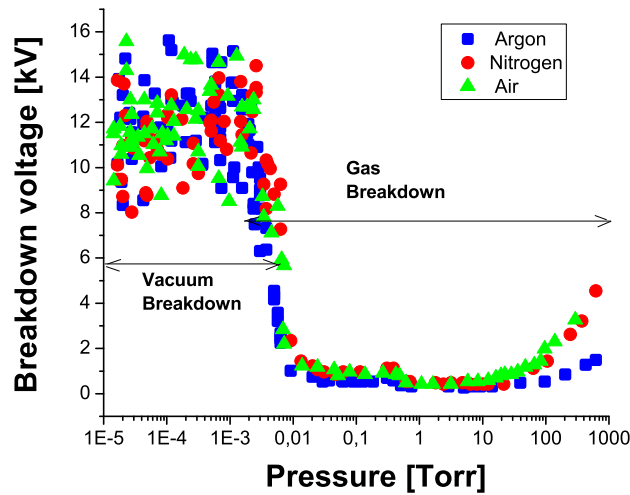


Fig. 9.1. Different electrical discharge regimes over a wide range of current.

posed by Crangber [127]. The limit on maximum electric field is determined as [127]:

$$E_{\max} = 10^5/U, \quad (9.1)$$

where  $E_{\max}$  is expressed in kV/cm, while the voltage  $U$  in kV. A constant product of the electric field and the voltage is attributed to the fact that vacuum breakdowns are caused by microparticle transport. The idea is that microscope electrode protrusions with induced charge proportional to the electric field  $E$  become detached and accelerate across the vacuum gap. When they strike the opposite electrode, their kinetic energy is proportional to product  $E \cdot U$ . Above a certain energy, the impact drives enough material from the surface to initiate a vacuum arc. The theory is consistent with several experimental observations: polished electrodes made of hard materials sustain higher voltages; breakdown levels may be raised by conditioning. During conditioning, the system is isolated with a high series resistance to prevent anode damage; surface contaminants should be avoided. This implies high vacuum and bake-out of the electrodes.

For clean, well-conditioned surfaces, the breakdown level for long pulses ( $\tau > 1$  ms) or DC operation is expressed as:

$$E_{\max} \leq 8000/U. \quad (9.2)$$

On the other hand, higher electric fields are possible with short pulses, when the relationship between the electric field and the voltage is given by:

$$E_{\max} \leq 1000/(U\tau^{0.34}), \quad (9.3)$$

where  $\tau$  is expressed in seconds.

### 9.1 Electrode separation

For vacuum gaps less than about 1 mm, the breakdown voltage is approximately proportional to the length, but all other parameters remaining almost constant providing a constant breakdown strength. For these small gaps, the breakdown stress is relatively high, being of the order of 1 MV/cm and field emission of electrons probably plays an important role in the breakdown process. For the gap sizes  $d < 1$  mm, breakdown voltage can be determined as:

$$V = \kappa \cdot d, \quad (9.4)$$

where  $\kappa$  is a constant.

For the gaps  $d > 1$  mm, the breakdown voltage does not increase at an equal rate and the apparent breakdown stress for longer gaps is much reduced. As can be seen from Figure 9.2, the breakdown stress defined as the voltage required to cause breakdown divided by the distance between the electrodes is reduced for longer gaps. At a spacing of 10 cm, the breakdown stress is about 10 kV/cm.

It was shown theoretically that for longer gaps, the product of breakdown voltage and breakdown stress that remain constant:

$$U \cdot E = \kappa_1, \quad (9.5)$$

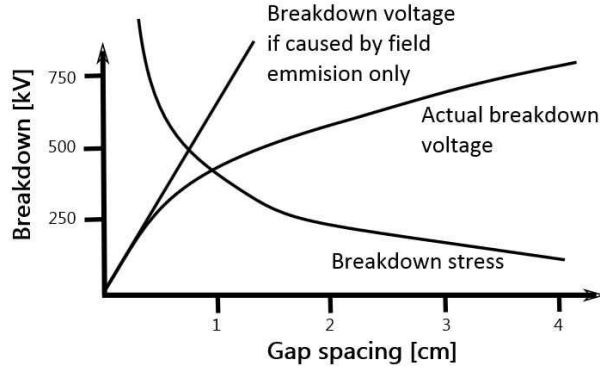


Fig. 9.2. The breakdown versus the gap spacing.

where the constant  $\kappa_1$  depends on the material and surface conditions of the electrodes. For gaps greater than about 1 mm, the breakdown voltage does not increase at an equal rate and the apparent breakdown stress for longer gaps is much reduced.

In general form, both regions can be expressed by the relation:

$$V = \kappa d^x, \tag{9.6}$$

where  $x = 0.5$  for  $d > 1$  mm and  $x = 1$  for  $d < 1$  mm.

### 9.2 Electrode effects

The breakdown voltage increases on successive flash-overs, until a constant value is achieved. The electrodes are then said to be conditioned. This increase in voltage is attributed to the burning off by sparking of microscopic irregularities or impurities which may exist on the electrodes. The effect of conditioning is clearly demonstrated in Figure 9.3. Unconditioned electrodes may have breakdown values low around 50% of the values recorded for the breakdown voltage with conditioned electrodes. Figure 9.4 shows the influence of the electrode material on the breakdown voltage. As can be noticed, the standard deviation for each material encompasses the average of all breakdown events taken together. Therefore, one may conclude that the underlying cathode material plays a minor role compared to that of the contaminant particles.

The electrode materials also strongly affect the values of the breakdown voltage. For example, for the gap size of 1 mm, the breakdown voltage for some electrode materials is given in Table 9.1 [110].

It was also found out that the presence of contamination reduces the breakdown voltage sometimes by as much as 50% of the clean electrode value.

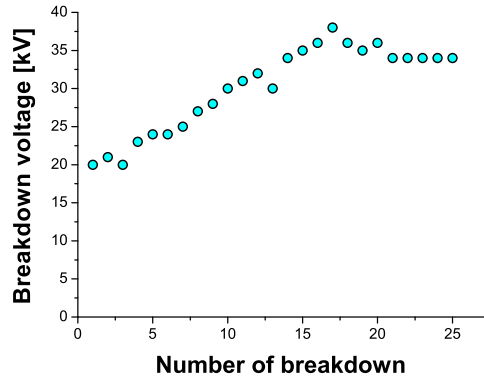


Fig. 9.3. The effect of conditioning on breakdown characteristics.

Electrode material	Breakdown voltage[kV]
Steel	122
Stainless Steel	120
Nickel	90
Monel metal	66
Aluminum	41
Copper	37

Tab. 9.1. Effect of electrode material on voltage across 1 mm gap [110].

### 9.3 Area and the electrode configuration

Comprehensive studies indicate that the electric field distribution of different electrode configurations is different although the same voltage is applied across the electrode, which further leads to the disparate breakdown voltage amplitude [128]. For example, the cone-ring electrode requires the maximum discharge breakdown voltage amplitude, while the breakdown voltage amplitude for cone-mesh, cone-cross line, and cone-line electrode is in descending sequence.

Under the same discharge conditions (including capacitor voltage, cathode material, shape and electrode spacing), the electrode configuration with higher breakdown voltage is able to generate higher-density plasma since the cathode runaway electrons can gain relatively larger energy from the electric field [128]. As respect to the same electrode configuration, the larger the voltage amplitude applied to the main discharge capacitor leads to the greater the discharge current and the greater plasma density. Nevertheless, the electrode breakdown voltage is independent of the changing of the voltage applied on the main discharge capacitor. The cathode itself supplies the particles to the gap in the vacuum discharge process and the generated plasma energy is directly related to the

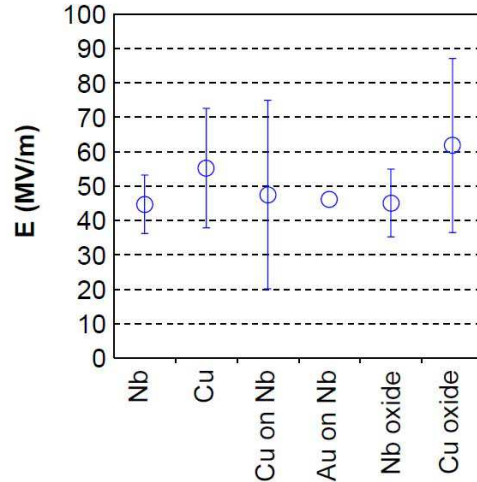


Fig. 9.4. The average breakdown fields for different materials. The materials are solid Nb, solid Cu (prepared in different ways, including electropolishing and diamond machining), Cu film on solid Nb, Au film on solid niobium, Nb oxide on Nb, and Cu oxide on Cu.

materials of the cathode.

Increasing the area of the electrodes makes it more difficult to maintain a given breakdown voltage. Thus breakdown voltage decreases slightly with increase in surface area. For example, for the 1 mm gap size and the same electrode materials, the electrodes of 20 cm<sup>2</sup> area provides the breakdown voltage of 40 kV, while the electrodes of 1000 cm<sup>2</sup> area gives breakdown voltage of 25 kV.

#### 9.4 Temperature and the pressure effect

The frequency dependence on the breakdown voltage has already been mentioned. The variation of the breakdown voltage with temperature is very small, and for nickel and iron electrodes, the field strength remains unchanged for temperatures as high as 500<sup>0</sup>C. On the other hand, cooling the electrodes to liquid nitrogen temperature increases the breakdown voltage.

For small gaps, increasing the degree of vacuum increases the breakdown voltage until below a certain pressure there is no change. The vacuum breakdown region is the region in which the breakdown voltage becomes independent of the nature of the pressure of the gap between the electrodes. However, for large gaps (about 200mm spacing) it is found that below a certain pressure the breakdown voltage starts decreasing again, so that the breakdown stress at this stage could in fact be improved by actually worsening the vacuum.

## 10 Multipaction breakdown

Multipaction breakdown appears from a resonant-secondary-electron emission in the conductor wall requiring a high-vacuum condition, where the mean free path of an electron is greater than the distance between the inner and outer conductors. Under such conditions, free electrons are accelerated by the electric field component of the microwave signal and strike the conductor surface, thus producing additional electrons. This electron cloud increases in intensity by being swept by half-wave cycles between conductor surfaces. When the gap distance, microwave frequency, and electric fields support a resonant mode, the process is sustained, and an electron avalanche condition exists.

As can be seen from Figure 10.1, transitions from classical discharge to multipactor phenomenon in RF range occur at lower pressures. The dotted line illustrates the expected behavior of the breakdown voltage from the classical DC gas discharge, while the horizontal line branching off in the transition region is the speculated behavior due to the influence of the high frequency applied fields. Actually, the behavior in the transition region, it is not entirely understood if the breakdown mechanism in this region is neither multipactor nor classical discharge.

At the pressures less than  $10^{-5}$  Torr multipaction breakdown is the limiting mechanism. At higher pressures, multipaction cannot exist and ionization breakdown is the limiting breakdown mechanism. Breakdown can be expressed in terms of the product between the conductor gap  $d$  (expressed in mm) and the fundamental frequency  $f$  (expressed in GHz). Referring to the Figure 10.2 that shows breakdown mechanism,

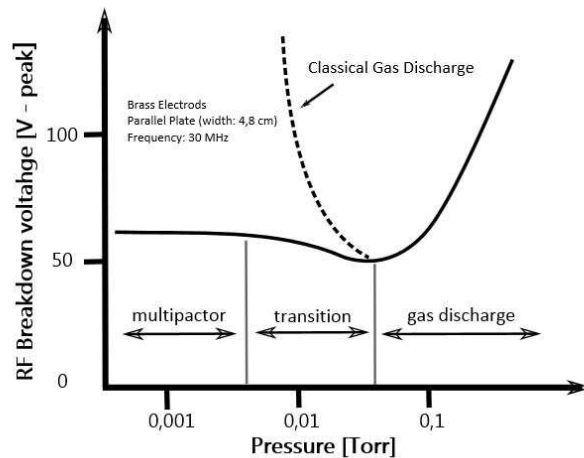


Fig. 10.1. Variation of RF breakdown voltage with pressure illustrating the pressure transition region from the gas discharge to multipactor discharges.

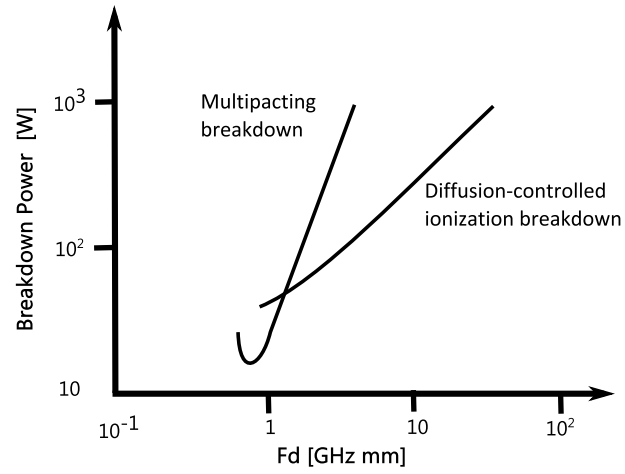


Fig. 10.2. Regions of multipacting and diffusion-controlled ionization breakdown.

multipaction is the dominating factor for  $fd$  product less than  $0.7\text{GHz} \cdot \text{mm}$ . Above  $2\text{GHz} \cdot \text{mm}$ , ionization breakdown limits power handling. Between these two regions, both mechanisms may take place as shown in Figure 10.2.

## 11 Breakdown in liquids

In the past few decades, studies of the liquid discharges and discharges in the gas and vapor phase in and around liquids have become extremely important due to a wide range of potential applications such as water decontamination or purification [129], microorganism destruction [130], biomedical and environmental applications [131]. Comparing with other conventional water treatment technologies, methods based on plasmas combine the contributions of UV radiation, active chemicals, and high electric fields which leads to higher treatment efficiency. Fundamental knowledge of the electric breakdown in water vapor, however, has not kept pace with these increasing interests, mostly due to the complexity of the phenomenon related to the plasma breakdown process. Recent studies of discharges with liquid electrodes [132] and discharges in heterogeneous water air bubble systems [133] are closely related to water vapor discharges since in both cases the gas would be expected to contain a significant percentage of water vapor affecting the most of its transport properties. As an illustration, Figure 11.1 shows columns observed in glow discharges [134].

In liquids, breakdown is controlled by phenomena similar to those for gases with the high electric strength. Unfortunately, liquids are easily contaminated and the effect of these impurities is relatively small for short duration pulses. However, if the voltage is applied continuously, the solid impurities line up at right angles to equipotentials and distort the field so that breakdown occurs at relatively low voltage. Under the action of the electric field, dissolved gases may come out of solution, forming a bubble. The gas in the bubble has a lower strength than the liquid, so that more gas is produced and the bubble grows, ultimately causing breakdown making electrical breakdown and streamer physics in liquids very complex. Two competing theories of liquid breakdown can be found in the literature: a bubble-initiated breakdown process [135] and an elec-

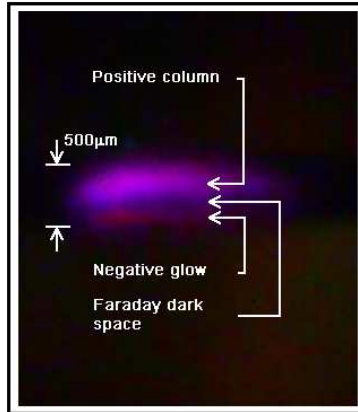


Fig. 11.1. Columns observed in DC discharge in water vapor, for the gap size of  $50 \mu\text{m}$  and the gas pressure of around 24 Torr [134].

tronic impact-ionization process within the bulk liquid [136]. Despite of growing demand for better understanding of water vapor breakdown, existing data on breakdown and discharge properties are scarce and often not well documented. Most of the measurements of the breakdown voltage curves for water vapor cover limited range of conditions [137] without the data for a minimum breakdown potential. Recently published data for the breakdown voltage curves for DC breakdown of water vapor in centimeter [138] and microgaps [134] cover a full range of pd product.

Three most important properties of liquid dielectric can be recognized: the dielectric strength, the dielectric constant and the electrical conductivity. Other important properties are viscosity, thermal stability, specific gravity, flash point etc. The most important factors which affect the dielectric strength of oil are the presence of fine water droplets and the fibrous impurities. For example, the presence of even 0.01% water in oil brings down the dielectric strength to 20% of the dry oil value and the presence of fibrous impurities brings down the dielectric strength much sharply. The impurities could also be in the form of gaseous bubbles which obviously have lower dielectric strength than the liquid itself and hence on breakdown of bubble the total breakdown of liquid may be triggered.

### 11.1 Electronic breakdown

When an electron is injected into the liquid, it gains energy from the electric field applied between the electrodes. Some electrons are accelerated under the electric field and would gain sufficient energy to knock out an electron and thus initiate the process of avalanche. The threshold condition for the beginning of avalanche is achieved when the energy gained by the electron equals the energy lost during ionization (electron emission) and can be determined as:

$$e\lambda E = ch\nu, \quad (11.1)$$

where  $\lambda$  is the mean free path,  $h\nu$  is the ionization energy and  $C$  is the constant. Typical values of dielectric strengths of some of the highly purified liquids are given in Table 11.1.

Liquid	Strength [MV/cm]
Benzene	1.1
Goodoil	1.0-4.0
Hexane	1.1-1.3
Nitrogen	1.6-1.88
Oxygen	2.4
Silicon	1.0-1.2

Tab. 11.1. Dielectric strengths (expressed in MV/cm) of pure liquids.

### 11.2 Suspended solid particle mechanism

Commercial liquids always contain solid impurities either as fibers or as dispersed solid particles. The permittivity of these solids  $\varepsilon_1$  are always different from that of the liquid  $\varepsilon_2$ . Under assumption that these particles are sphere with radius  $r$ , they get polarized in an electric field  $E$  and experience a force  $F$  expressed as:

$$F = r^3 \frac{\varepsilon_1 - \varepsilon_2}{\varepsilon_1 + 2\varepsilon_2} \cdot E \frac{dE}{dx}, \quad (11.2)$$

and increases as the permittivity of the suspended particles increases. If  $\varepsilon_1 > \varepsilon_2$ , the force is directed towards a place of higher stress. Otherwise, it is directed towards a place of lower stress. If  $\varepsilon_1 \rightarrow \infty$ , the previous expression for the force can be written as:

$$F = r^3 \frac{1 - \varepsilon_2/\varepsilon_1}{1 + 2\varepsilon_2/\varepsilon_1} \cdot E \frac{dE}{dx}, \quad (11.3)$$

$$F = r^3 E \frac{dE}{dx}, \quad (11.4)$$

which lead that the force will tend the particle to move towards the strongest region of the field. In a uniform electric field which usually can be developed by a small sphere gap, the field is the strongest in the uniform field region. Since  $dE/dx \rightarrow 0$ , the force on the particle is zero and the particle remains in the equilibrium. Therefore, the particles will be dragged into the uniform field region. Due to the fact that the permittivity of the particles is higher than that of the liquid, the presence of particle in the uniform field region will cause flux concentration at its surface. Other particles if present will be attracted towards the higher flux concentration. If the particles present are large, they become aligned due to these forces and form a bridge across the gap. The field in the liquid between the gap will increase and if it reaches critical value, breakdown will take place. If the number of particles is not sufficient to bridge the gap, the particles will give rise to local field enhancement and if the field exceeds the dielectric strength of liquid, local breakdown will occur near the particles and thus will result in the formation of gas bubbles which have much less dielectric strength and hence finally lead to the breakdown of the liquid.

The movement of the particle under the influence of electric field is opposed by the viscous force posed by the liquid and since the particles are moving into the region of high stress. So, equating the electrical force with the viscous force we obtain:

$$6\pi\eta r\nu = r^3 E \frac{dE}{dx}, \quad (11.5)$$

where  $\eta$  is the viscosity of liquid and  $\nu$  the velocity of the particle. Diffusion process also should be included and the drift velocity due to diffusion is:

$$v_d = -\frac{D}{N} \frac{dN}{dx} = -\frac{KT}{6\pi\eta r} \frac{dN}{Ndx}, \quad (11.6)$$

where  $K$  is Boltzmann's constant and  $T$  the absolute temperature. The relation  $D = KT/(6\pi\eta r)$  is known as Stokes-Einstein relation. It is straightforward to obtain the

relation between breakdown strength  $E$  and the concentration of particles  $N$ , radius  $r$  of particle, viscosity  $\eta$  of liquid and temperature  $T$  of the liquid:

$$\frac{KT}{r} \ln N = -\frac{r^2 E^2}{2}. \quad (11.7)$$

It was found that liquid with solid impurities has lower dielectric strength as compared to its pure form. Also, it has been observed that larger the size of the particles impurity the lower the overall dielectric strength of the liquid containing the impurity.

The electric field in a gas bubble which is immersed in a liquid of permittivity  $\varepsilon_2$  can be written as:

$$E_b = \frac{3E_0}{\varepsilon_2 + 2}, \quad (11.8)$$

where  $E_0$  is the field in the liquid in absence of the bubble.

The breakdown strength depends on the initial size of the bubble which of course depends upon the hydrostatic pressure above the bubble and temperature of the liquid, which is included in a more accurate expression for the bubble breakdown strength:

$$E_b = \frac{1}{\varepsilon_2 - \varepsilon_1} \left\{ \frac{2\pi\sigma(2\varepsilon_2 + \varepsilon_1)}{r} \left[ \frac{\pi}{4} \sqrt{\frac{U_b}{2rE_0} - 1} \right] \right\}^{1/2}, \quad (11.9)$$

where  $\sigma$  is the surface tension of the liquid,  $\varepsilon_2$  and  $\varepsilon_1$  are the permittivities of the liquid and bubble, respectively,  $r$  the initial radius of the bubble and  $U_b$  the voltage drop in the bubble.

### 11.3 Cavity breakdown

It was shown experimentally that the dielectric strength of liquid depends upon the hydrostatic pressure above the gap length. The higher the hydrostatic pressure, the higher the electric strength, which suggests that a change in phase of the liquid is involved in the breakdown process. Consequently, a kind of vapor bubble formed plays a crucial role in the breakdown. Several processes might lead to formation of bubbles in the liquids: gas pockets on the surface of electrodes, due to irregular surface of electrodes, point charge concentration may lead to corona discharge, changes in temperature and pressure and dissociation of products by electron collisions giving rise to gaseous products.

## 12 Microdischarges: departure from the Paschen curves

The Paschen's law [38] is based on the observation that, over a large range of pressures and electrode separations, the probability of the ionization per collision in the gas and the probability of the production of the electrons by the ions by a secondary process are both dependent on the average kinetic energy of the electrons and ions and therefore on the reduced electric field  $E/N$  [19]. The Townsend mechanism by which successive ionizations of gas molecules induce the gas breakdown, describes the process satisfactorily at large separations [19]. Avalanches, however, can not be built up in the same way in microgaps. The number of ions in the inner-electrode space is too small so the initiation of the electrical breakdown is based on the cathode-induced breakdown model [44, 62].

Deviations from Paschen's theory in microgaps were first reported in the 1950's by Germer and Kisluik [42, 104] in a series of papers that studied sub-millimeter electrode spacings. Later, Torres and Dhariwal [44] provided an explanation for the deviation based on quantum tunneling of electrons during a study of micro-motors and micro-actuators. Lee et al. observed similar results while investigating electrode erosions caused by arc discharges [111]. Slade and Taylor [160] compared the work done by Torres et al. [44] and Lee et al. [111] and applied a linear-fit equation to the breakdown voltage versus the gap data. They also introduced the effect of cathode micro-projections into the Fowler-Nordheim equation to quantify the role of field emissions in the breakdown process. Figure 12.1 clearly demonstrates departure of the experimental data for microgaps taken from [111] (solid symbols) and [44] (open symbols) from the standard Paschen law (solid curve). Figure 12.2 contains breakdown voltage curves measured for a fixed pressure of 746 Torr illustrating failure from the standard scaling law in microgaps [103]. For the gaps lower than  $5 \mu\text{m}$ , breakdown voltage curves for all gases demonstrate the departure from the standard Paschen law.

When the electric field near the cathode becomes sufficiently large, electron tunneling

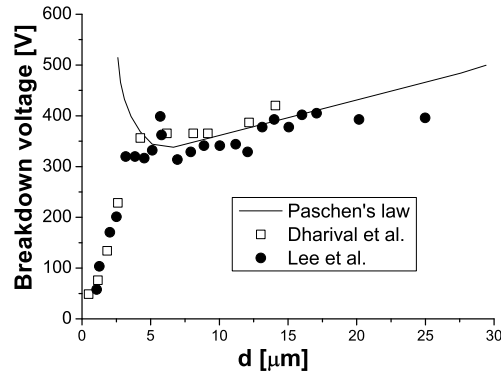


Fig. 12.1. Failure from the Paschen law observed in microgaps.

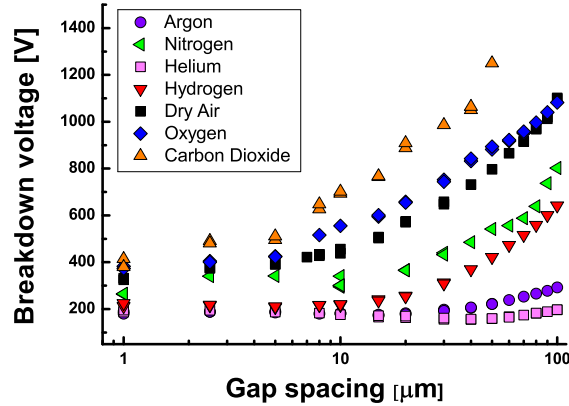


Fig. 12.2. Paschen curves measured for different gases for a fixed pressure of 746 Torr by varying the gap size [103].

from the metal to the gas phase needs to be taken into account. Furthermore, as an ion approaches the cathode, it lowers the potential barrier seen by the electrons in the metal resulting in an ion-enhanced electron field emission [104]. An explicit expression for the effective secondary electron emission coefficient  $\gamma$  that incorporates this ion-enhanced field emission is suggested by [104]:

$$\gamma_{\text{eff}} = K e^{-D/E}, \quad (12.1)$$

where  $K$  and  $D$  are material and gas dependent constants and  $E$  the electric field near the cathode. The proposed process of the electron emission due to the combined applied and ionic-space charge fields depends primarily on the electric field  $E$  rather than  $E/N$ , leading directly to the limitation of the Paschen's law. According to expression (12.1), when the electric field in the cathode region is larger than the threshold value given by  $D$ , the secondary electron emission coefficient increases rapidly as illustrated by Figure 6.6. A rapid fall of the breakdown voltage with decreasing gap size may be attributed to the onset of the ion-enhanced field emission in microgaps. The constant  $D$  depends on the work function in accordance to the expression [104]:

$$D = 6.85 \times 10^7 \Phi^{3/2} / \beta, \quad (12.2)$$

where  $\beta$  is the field enhancement factor involving the geometric effects on the surface and  $\Phi$  is the work function of the metal expressed in eV. In this paper we have used the value of  $9.3 \times 10^8 \text{V/m}$  that corresponds to the aluminum [104]. On the other hand, determination of the constant  $K$  that appears in expression (12.1) may be quite difficult, especially if there are complications due to electron attachment, ionization by metastables, ect. (for more details see Ref. [104]). In particular, the constant  $K$  can be determined from

the ratio of the field emission current density to the positive ion current density onto the cathode [45].

Violations of the similarity law take place for the left hand branch, for such  $pd$  values where the electron mean free path is comparable to the separations. This regime can be determined from the condition:

$$d/\lambda_0 = \sigma n_0 p d \leq 1, \quad (12.3)$$

where  $\lambda_0$  is the mean free path of the electron,  $\sigma$  is the effective cross section for the collisions of electrons with neutrals and  $n_0$  is the gas density at a unit pressure [80].

One of the key issues in transferring our standard knowledge for low pressure non-equilibrium discharges to micro discharges is that of scaling. The Paschen curve obtained when the field emissions are accounted for, retains the right branch of the conventional Paschen curve, i.e. field emissions can be neglected for large gaps. The left branch, however, is substituted by a rapid decrease of the breakdown voltage below the minimum of the conventional Paschen curve [45].

### 13 Historical review of the electrical discharges in strong fields

The scientific literature dealing with DC breakdown originates from the early days of gaseous electronics. In the early twentieth century, Millikan showed that breakdown voltage has no dependence on the ambient pressure once a high vacuum is achieved [139]. In 1928, Fowler and Nordheim introduced the model of the field emission due to the tunneling probability through a triangular barrier and applied it to the emission of electrons from a metal under the influence of a strong electric field [140]. The basic Fowler-Nordheim model persists to this day, albeit with various modifications and enhancements [141]. The Fowler-Nordheim field emission has received experimental confirmation for sharply-pointed (single crystal points) electrodes [142]. In calculation of the tunneling rate, one assumes nearly-free electrons near the Fermi level and a sharp transition to vacuum. In reality, larger-area electrodes do not present ideal surfaces and the field emission mechanism(s) on electrodes with macroscopic areas is(are) still not completely understood.

A detailed review of field emission was provided by Noer [143]. It was shown that field emission occurs at much lower fields than those predicted by Fowler-Nordheim. Moreover, electrons appear to be emitted from a few tiny points on the cathode [144], not from the whole cathode area. Initial explanations involved microprotrusions on the surface that enhance the electric field. Some experiments actually found protrusions [145]-[149]. However, a number of problems are related to the protrusion model [143]. Actually, protruding shapes definitely enhance the electric field and field emission and according to some papers the geometrically enhanced field emission is the only certain way of enhancing field emission. Other theories of field emission have been suggested and developed [150], but they are not easy to confirm experimentally, because they are sensitive to complicated surface states and they are not as simple as the Fowler-Nordheim model with geometric field enhancement. In order to find similarities between DC breakdown and breakdown in superconducting cavities, it's important to note that superconductivity seems to have no effect on field emission.

Microprotrusion model offered an attractive explanation for vacuum breakdown. Field emission indicated the presence of long, thin, pointy whiskers on the cathode. High current densities would heat the whisker, the thinness of which would impede thermal conduction to the bulk cathode, allowing the tip of the emitter to reach very high temperatures. If the tip is vaporized, providing a source of neutral gas, the field emission would ionize the gas and ions would bombard the cathode, creating more heating, more vaporization and more current and breakdown would occur. The vaporizing field emitter model is so attractive, although have some shortcomings such as that field emission often does not originate from extremely tall and thin protrusions, which are necessary to explain a large temperature rise. At the same time, even with assumption of a long and thin emitter, the mechanism by which vapor is suddenly produced has not been well understood.

Nevertheless, there is the vaporizing microprotrusion model. For extremely sharp cathodes, where field emission is reasonably Fowler-Nordheim, this model appears to be a good explanation [151, 152]. Charbonnier et. al. [153] have worked out the critical field enhancement factor that divides the cathode-initiated breakdown described above and

anode-initiated breakdown. Emitters like needle have higher enhancement and higher current densities and Joule heating at the emitter should be proportional to the current density squared. On the other hand, heating at the anode will be proportional to the total current times the voltage, so higher field enhancements cause higher power densities at the cathode than at the anode, while lower field enhancements lead to higher power densities at the anode than at the cathode.

Kranjec and Ruby [154] carried out measurement of the field emission before breakdown on thirteen different electrode materials with mechanically polished, heavily conditioned electrodes. They found that for each material the local electric field at breakdown was constant, The local electric field was found by multiplying the macroscopic field by the enhancement factor found by fitting the emission current to the Fowler-Nordheim formula. The critical local breakdown field is related to a critical current density via Fowler-Nordheim model. In [155], Alpert et. al. published similar experimental data supporting the existence of the critical local field in the theory of breakdown. They also point out that in general, larger gaps lead to higher field enhancements explaining the generally observed diminishing of breakdown field that larger gaps have higher field enhancements and hence they break down at lower macroscopic fields.

Since the production of vapor is very important for vacuum breakdown, a few experiments detecting vaporized electrode material should be listed here. Kranjec and Ruby [154] concluded that the local breakdown field for aluminum lays between 9.8 and 11.2 GV/m with values of enhancement factor from 72 to 309. Bennette et. al. [156] determined the local breakdown field ranging from 5.8 to 8.9 GV/m with enhancement factors from 24 to 360. In the experiment described in [157], the electrode vapor was detected microseconds before breakdown, measured the vapor by its absorption of light, which allowed detection before breakdown. The vapor density is greater near the cathode than the anode. The importance of this experiment is not only that vapor is detected just before breakdown, but also that the vapor is the same material as the bulk electrode. Other experiments have measured light emission from cathode and anode material [158, 159], which measures vapor only after the onset of the arc and not before the arc. In [158] pulsed voltages were used in order to show that for breakdown events that begin within microseconds after the pulse rise, cathode vapor emits light first, but when breakdown occurs after a longer period, anode vapor first emits light. Several mechanisms for breakdown have been proposed, none of them universally acceptable, but more than one may be applicable in different situations. The validity of each model depends on its explanation of how to get vapor and then charged particles into the gap (and the vapor is the hard part, since field emission can make ions from vapor). Various models involve small clumps of material breaking off the cathode or anode due to electric field pressure and heating, abrupt and violent explosions at the field emitter, etc. Finally, in the past few years, simulations that include Fowler-Nordheim model have been extensively performed based on fluid models or kinetic models [161] - [165]. For our studies, we have used the PIC/MCC code with implementation of the secondary emission enhanced by strong fields in microgaps [62] - [64], as well as Fowler-Nordheim equations [164, 165].

## 14 The Fowler-Nordheim equations

The process of the extraction of electrons from a solid by tunneling through the surface-potential barrier under the application of a strong electric field i.e. field emission is mathematically expressed by the the Fowler-Nordheim (F-N) equation [140]. This phenomenon is highly dependent on both the properties of the material and the shape of the particular cathode, so that higher aspect ratios produce higher field emission currents. The current density produced by a given electric field is governed by the Fowler-Nordheim equation. The original Fowler-Nordheim equations [140] was erroneous and have been corrected and developed further by the inventors themselves and other authors [166] - [168]. The Fowler-Nordheim (F-N) equation provide relation between the current density of field emission electrons and the electric field at the surface of the emitter [140]:

$$j_{FE} = \frac{A^2 \beta^2 E^2}{\phi t^2(y)} \exp\left(-\frac{B \phi^{3/2} \nu(y)}{\beta E}\right), \quad (14.1)$$

where  $j_{FE}$  is the current density and  $\phi$  is the work function, while  $A = 6.2 \times 10^{-6}$  A/eV and  $B = 6.85 \times 10^7$  V/cm/eV<sup>3/2</sup> are constants.

Factors  $\nu(y) \approx 0.95 - y^2$  and  $t^2(y) \approx 1.1$  represent corrections that include the influence of a tunneling barrier shape on the exponential term in the F-N equation and  $y \approx 3.79 \times 10^{-4} \sqrt{\beta E} / \phi$ . For nanostructures, the local field strength  $E$  is usually much stronger than the applied field  $E_{\text{appl}}$ , and modified by a field enhancement factor  $\beta = E/E_{\text{appl}}$  depending on the aspect ratio of the nanostructures, crystal structures, and the density of the emitting points. Actually, Fowler and Nordheim originally have calculated the current for a cold flat surface [140]. In fact, the current weakly depends on temperature, but it is strongly dependent on emitter shape. To take shape into account, there is a geometric field enhancement parameter  $\beta = E/E_{\text{app}}$  defined as the ratio of the local emitter field over the applied field. The local field enhancement factor  $\beta$  is often introduced in the Fowler-Nordheim equation to represent the geometrical effects at the surface of the cathode [164]. In principle, this factor has a direct physical meaning only for metallic protrusions. If the shape of the protrusion is reasonably simple, its  $\beta$  value can be calculated quite accurately. Experimentally, the numerical value of  $\beta$  can be derived from Fowler-Nordheim plot. This plot can be used for determination if the current flow is due to field emitted electrons. In general, the F-N equation, derived from quantum mechanical considerations, implies that a perfect surface has a  $\beta$  value of unity. However, curve-fitting of experimental results requires values of  $\beta$  as high as 1000 or more [169]. This is attributed to field gradient enhancements resulting from microscopic surface irregularities [80]. As an illustration of the enhancement factor  $\beta$  on the simulation results, comparison between the measured current-voltage characteristics (black symbols) and corresponding curves obtained by using F-N expression (19.1) for various  $\beta$  values is demonstrated in Figure 14.1.

$$\ln\left(\frac{I_{FE}}{U^2}\right) = \varsigma - \frac{1}{U}\xi, \quad (14.2)$$

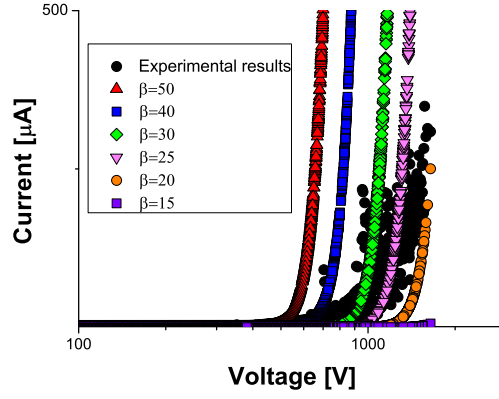


Fig. 14.1. Experimentally recorded current-voltage characteristics (black symbols) and the curves plotted in accordance with the F-N expression (19.1) for various values of the enhancement factor  $\beta$  for the gap size of:  $5 \mu\text{m}$  [165].

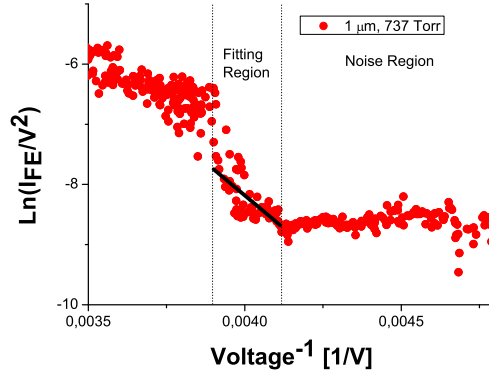


Fig. 14.2. Fowler-Nordheim plot. Solid symbols correspond to our experimental data for  $1 \mu\text{m}$  gap size and the pressure of 737 Torr, while black line represents the fit to the experimental data [165].

$$\varsigma = A_e \frac{1.54 \cdot 10^6 \beta^2}{\phi \cdot d^2} \exp(10.41 \cdot \phi^{-1/2}), \quad (14.3)$$

$$\xi = \frac{6.53 \cdot 10^3 \cdot \phi^{3/2}}{\beta/d} \approx \frac{\text{constant}}{\beta}. \quad (14.4)$$

Field emission results are more conventionally and clearly demonstrated by the so called Fowler-Nordheim (F-N) plot which shows  $\ln(I_{FE}/U^2)$  versus  $U^{-1}$ . In the scenario of electron field emission, the F-N plot should fit a straight line as shown in Figure 14.2. In the fitting region, experimental data for the  $1 \mu\text{m}$  gap size and the pressure of 737 Torr are fitted by black line in accordance with expression (3.4).

## 15 Space charge field

Relation between the space charge and the field emission effect is an important issue due to strong variation of the emitted current with the field that exists at the emission site. Consequently, charge between anode and the emitter (or emitter-gate) boundary bears a complex relation to the voltages and separation distances defining the diode region indicating the impact of the space charge on field emission. In the pre-breakdown stage of electrical breakdown of gases under high pressure and high voltage, the space-charge field and the secondary mechanisms for electron production play an important role. When field emission effects take place the space charge of electrons leaving the cathode produces a region of low-potential potential in front of the cathode, inhibiting electron flow from the cathode and limiting the current density  $j_{CL}$ . The space charge limiting current density can be determined from Child's law [170]:

$$j_{CL} = \frac{4\varepsilon_0}{9} \sqrt{\frac{2e}{m}} \frac{U^{3/2}}{d^2}. \quad (15.1)$$

At higher pressures such as atmospheric pressures, an avalanche increase in the discharge gives rise to a space charge, which alters the character of the breakdown process. In our experiment, the ionic space charge field at the cathode  $E_+$  is macroscopic value which is low even for the maximal experimental currents  $E_+ \sim 0.1 - 1\text{V/cm}$  whereas the applied field  $E \approx 2.5\text{MV/cm}$ . The field of the ion approaching the cathode surface is the microscopic field of an individual ion, that can be very high at the distances small in comparison with  $d$  and the mean distance between the neighboring ions,  $r \sim 3\ \mu\text{m}$  for  $d = 1\ \mu\text{m}$ . When an ion contacts the cathode its field is sufficient to extract electron independently due to the same tunnel effect. This is the usual mechanism of the secondary emission.

For a work function of  $\phi = 4.5\text{eV}$  and a gap length of  $1\ \mu\text{m}$ , F-N current density (blue symbols) obtained from the experimental data in accordance with equation (14.1) and space charge limited current density (red symbols) calculated from equation (15.1) versus the electric field are shown in Figure 15.1. They cross at around  $1.3 \cdot 10^6\ \text{V/cm}$  considering it as the "transition field" (transition from F-N field emission to space charge current density) [170].

### 15.1 Estimation of the space charge field

Space charge field can estimated in accordance to [165]:

$$E_+ \approx \frac{en_+d}{2\varepsilon_0} \approx \frac{j_+d}{2\varepsilon_0v_+} \quad (15.2)$$

where  $n_+$ ,  $j_+$  are the ion- and ion current densities, respectively and  $v_+$  is the ion drift velocity.

For the gap size of  $d = 1\ \mu\text{m}$ ,  $V_t = 250\text{V}$ ,  $I_{\text{max}} = 1.6\text{mA}$ , the cathode area  $S = 0.2\text{cm}^2$  and the obtained mean value of  $\gamma_{\text{eff}} \approx 4$ , the applied field is  $E = 2.5\text{MV/cm}$ , while the current density is  $j_+ = I_{\text{max}}/[(1 + \gamma_{\text{eff}})S] = 1.5\text{mA/cm}^2$ .

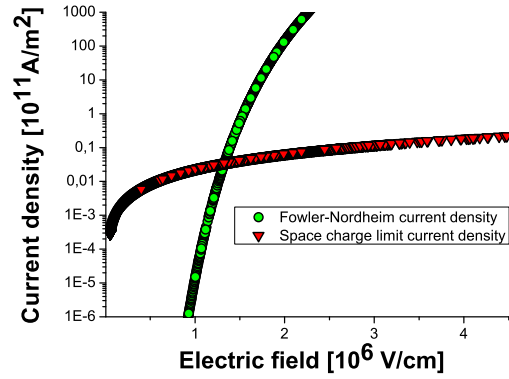


Fig. 15.1. Comparison of F-N current density (blue symbols) with space charge limited current density (red symbols) for a range of electric field at the  $1 \mu\text{m}$  gap size.

For the ratio  $E/p = 3300\text{V}/(\text{cm} \cdot \text{Torr})$ , the ion mobility is not constant. The ion energy is  $\varepsilon_+ \approx eEl = 33\text{eV}$  and  $v_+ \sim (eEl)^{1/2} \sim 10^7\text{cm/s}$  for the length of free path  $l \approx 1.310^{-5}\text{cm}$ . As a result we obtain the density of  $n_+ \approx 10^9\text{cm}^{-3}$  and  $E_+ \approx 0.08\text{V/cm}$ .

For the gap spacing of  $d = 10 \mu\text{m}$ ,  $E_+ \sim 1\text{V/cm}$ . The mean distance between the neighboring ions  $r \sim n_+^{-1/3}$ . But for  $d = 1 \mu\text{m}$  we obtain  $r = 10 \mu\text{m} > d$ . For such cases  $r \sim n_+^{-1/2} d^{-1/2} \sim 3 \mu\text{m}$ . The field of an individual ion at the distance  $r$  is  $1.6\text{V/cm}$  and is, therefore, comparable with the field of the space charge.

## 16 Semi-empirical formula

When changing the size of plasmas there are scaling laws that are helpful in determining the operating parameters of various sizes of plasmas. An important scaling factor for a dc plasma is the product of  $pd$ , which must remain constant. It means that, if  $d$  is reduced then  $p$  must be increased to keep the product constant.

Let start from the DC breakdown criteria [21]:

$$\gamma (e^{\alpha d} - 1) = 1, \quad (16.1)$$

where  $\gamma$  and  $\alpha$  are the already introduced electron yield and ionization coefficient, respectively. Combining the equations (16.1) and (4.4) with the expression (12.1) for the effective yield, we obtain a transcendental equation:

$$K e^{-Dd/V} \left( e^{A p d e^{-B p d/V}} - 1 \right) = 1, \quad (16.2)$$

$K$  and  $D$  are material and gas dependent constants. The equation (16.2) has no analytical solution and can be solved numerically in order to obtain the breakdown voltage as a function of the gap size  $d$ . The obtained numerical values for the breakdown voltage, for a fixed pressure of 760 Torr, are then fitted by simple analytical expression [45]:

$$V = a + b * d^c, \quad (16.3)$$

where values of the fitting coefficients  $a$ ,  $b$  and  $c$ , for various gases are given in Table 16.1.

### 16.1 The pressure dependence

The equation (16.2) has been also solved numerically for the fixed gap spacing of  $1 \mu\text{m}$  in order to obtain the pressure dependence of the breakdown voltage. The fitting procedure,

Gas	$a$	$b$	$c$
Argon	-31.71	95.56	0.69
Helium	-11.01	80.71	0.84
Xenon	-30.04	90.83	0.65
CO <sub>2</sub>	-22.93	85.61	0.72
Acetone	-23.93	87.69	0.73
Methane	-19.99	86.18	0.78
Neon	-31.71	95.56	0.69
Krypton	-33.63	96.15	0.66
Hydrogen	-16.00	83.56	0.81
Air	-24.32	87.89	0.73
Oxygen	-21.14	86.98	0.77
Nitrogen	-22.37	86.83	0.75

Tab. 16.1. Fitting parameters that appear in the semi-empirical formula (16.3). The voltage is expressed in [V] [45].

Gas	$m$	$n$
Argon	101.42	-0.07
Helium	120.61	-0.08
Xenon	87.92	-0.06
CO <sub>2</sub>	83.83	-0.04
Acetone	90.75	-0.05
Methane	104.24	-0.07
Neon	115.34	-0.08
Krypton	96.44	-0.07
Hydrogen	109.84	-0.07
Air	90.24	-0.05
Oxygen	102.94	-0.07
Nitrogen	92.86	-0.05

Tab. 16.2. Fitting parameters for the semi-empirical formula (16.4).

in that case, has been performed by using a simple functional form:

$$V = m * p^n, \quad (16.4)$$

with fitting coefficients  $m$  and  $n$  given in Table 16.2. The voltage is expressed in [V] and the pressure in Torr [45].

Figure 16.1a shows the dependence of the breakdown voltage on the gap spacing for the pressure of 1 atm in argon. Three curves are plotted. Solid curve represents the standard Paschen curve obtained not taking into account ion-enhanced field emission. The second one (solid symbols) represents simulation results obtained including field emission described by equation (12.1) taken from Ref. [104]. Experimental results [8] are shown by open symbols. Finally, the dot curve was plotted by applying semi-empirical formula (16.3). As expected, for relatively large gaps, a small difference is found between all three curves. For gaps smaller than  $5 \mu\text{m}$ , however, significant differences can be observed between conventional (solid curve) and modified Paschen curve (solid symbols), although the expression (16.3) satisfactorily describes the reducing of the breakdown voltage in microgaps. The exponential dependency of the field emission on the electric field strength pins the electric field during breakdown to the threshold for field emission and allows for a rapid reduction of the breakdown voltage as gap size is reduced. A comparison between the available experimental data taken from [111] (triangles) and [44] (circles) and the theoretical prediction achieved applying simple formula (16.3) (dot curve) for the breakdown curve in air is shown in Figure 16.1b. Similar trends are observed in both experimental and theoretical results, especially in the small gaps where field emission effect becomes significant. For the gaps larger than  $10 \mu\text{m}$ , theoretical prediction does not follow the standard Paschen law, as expected, since the expression (16.3) has been derived including field emission effect.

The breakdown voltage as a function of the pressure for a fixed gap size of  $1 \mu\text{m}$  is given in Figure 16.2. The presented results were obtained by using the fitting expression

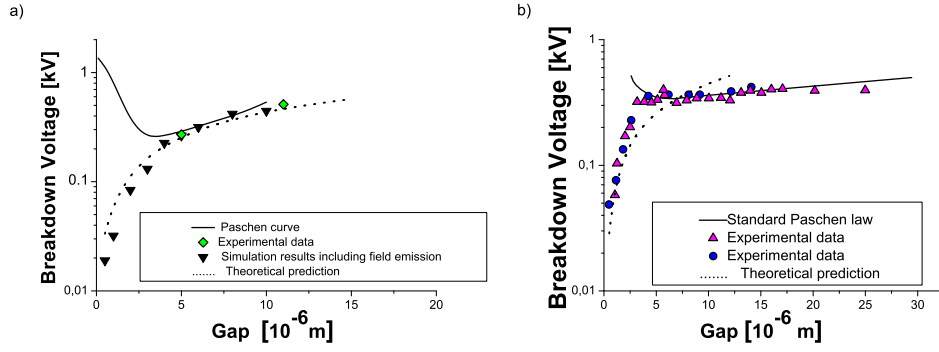


Fig. 16.1. Breakdown voltage curves at the pressure of 1 atm in: a) argon and b) air. In the case of argon, results of measurements [8] are shown by open symbols. The experimental data for air are taken from Refs. [111] and [44] are shown by triangles and circles, respectively.

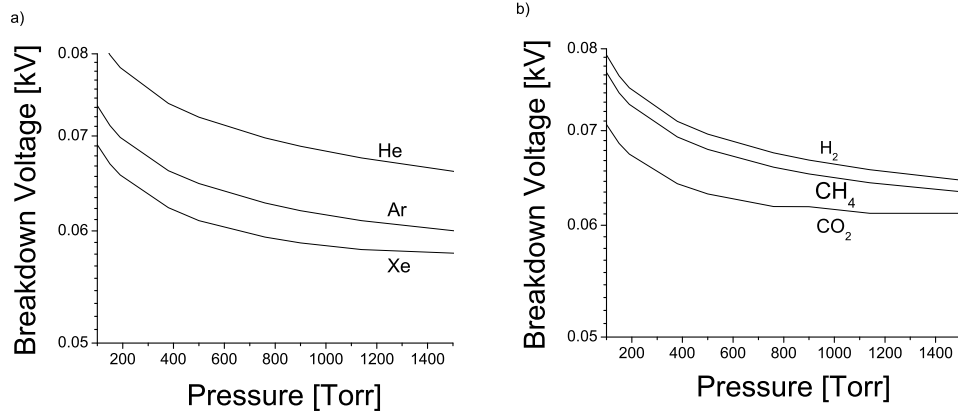


Fig. 16.2. Breakdown voltage for electrodes separations of  $1 \mu\text{m}$  against the gas pressure for: a) inert and b) molecular gases. All curves are obtained by using expression (16.4), with the fitting coefficient given in Table 16.2.

(16.4) based on the numerical solving of the equation (16.2). The dependence was studied for the pressure in the range between 100 and 1500 Torr. As can be observed from the Figure 16.2, the breakdown voltage slightly varied with changing the pressure since in microgaps breakdown is no longer controlled by the processes within the gas. At the gas pressure of 1 atm or more, the electron mean path is of the order of a few micrometers so at small inter-electrode spacings breakdown is initiated by the secondary emission processes instead of a gas avalanche process.

### 17 Semi-analytical relation

The effective yields estimated from the experimental results for the breakdown voltage curves (see Figure 12.2) can be fitted by the expression (12.1). From the slopes of the straight lines plotted in Figure 17.1, parameters  $D$  and  $K$  have been determined for various gases and listed in Table 17.1. These parameters, then, can be used in semi-analytical expression derived for the DC breakdown voltage in microgaps [46, 103]:

$$U_{DC} = \frac{d(D + Bp)}{\ln[ApdK]}. \quad (17.1)$$

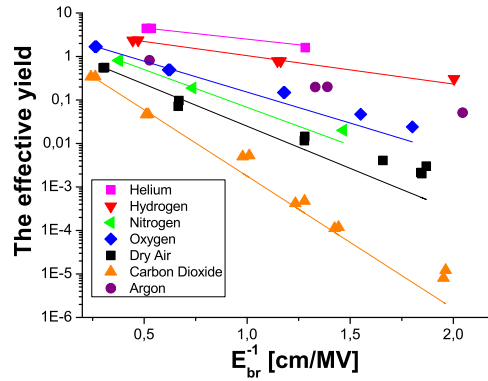


Fig. 17.1. The effective yields determined from the measured breakdown voltage curves shown in Figure 12.2.

Gas	$K$	$D[10^8 \text{ V/cm}]$
Helium	8,08	1,16
Argon	2,02	1,71
Hydrogen	4,69	1,50
Oxygen	4,00	3,28
Dry air	2,16	4,46
Nitrogen	3,69	4,00
Carbon Dioxide	1,98	7,02

Tab. 17.1. Fitting parameters  $D$  and  $K$  for the semi-empirical formula (17.1).

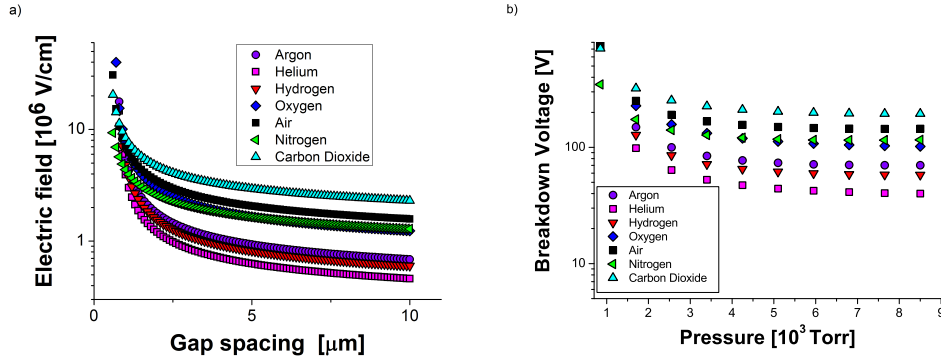


Fig. 17.2. a) The gap size dependence of the electric field strength at a fixed pressure of 600 Torr. b) The pressure dependence of the breakdown voltage at a fixed gap spacing of  $5 \mu\text{m}$ .

## 18 Experimental set-up for DC breakdown in microgaps

The experimental apparatus developed at Comenius University for the studies of the breakdown voltage curves and the volt-ampere (V-I) characteristics of direct-current (DC) gas discharges in microgaps is shown in the Figure 18.1, with schematic view of the system depicted in the Figure 18.2 [134, 64, 88, 103]. The apparatus includes precise positioning systems allowing movements of the electrodes in different directions. The vacuum chamber, pumped to high vacuum by the turbomolecular pump, itself consists of three parts. In the upper part shown in Figure 18.3 there is a positioning system for adjusting of the electrode in three directions (with accuracy of about  $1 \mu\text{m}$ ) and tilting the upper electrode. In the middle part there is a glass crux with four fused silica window for observation of the discharges and possible spectral measurements. In the bottom part (see Figure 18.4) there is also positioning system for tilting electrode as well as a system for ultra fine tilting shown in Figure 18.5. The tilting system is very important for precise plan-parallel alignment of the electrodes.

The upper part of electrode is in the center of the sphere with the radius 45 cm. The electrode is set up in a cradle. There are a micrometric screws for moving electrode in this cradle” enabling to achieve parallelism of the electrodes to an accuracy of  $0.1 \mu\text{m}$  which is, of course, the theoretical limit since the method resides on optical measurement of the gap using illumination by the led diodes and microscope measurements. With micrometric screw we are able to set distance  $1 \mu\text{m}$ .

### 18.1 Electrodes

In the experiments two different types of the electrodes were used. For recording the right hand side of the breakdown voltage curves only we used molybdenum electrodes with Bruce profile shown in Figure 18.6. For the measurements of the breakdown voltages in the whole range of  $pd$ , however, molybdenum electrodes melted in the glass were used (see Figure 18.7)[134, 64, 88, 103]. For both electrodes the identical experimental



Fig. 18.1. Photograph of the apparatus used for the measurements of the DC breakdown voltage curves and volt-ampere characteristics at micrometer separations between two planar electrodes.

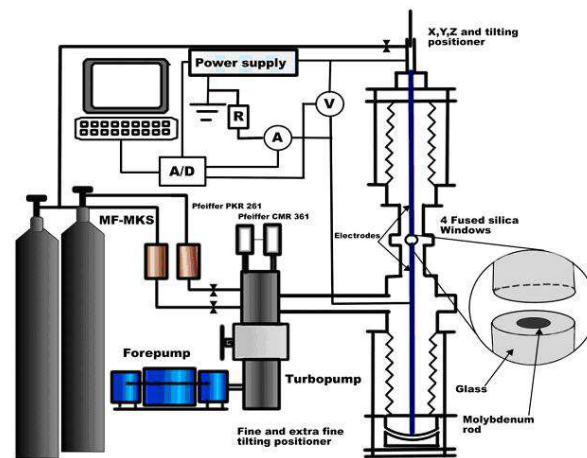


Fig. 18.2. The general layout of the experimental set-up used for the measurements of the direct current breakdown voltage and volt-ampere characteristics in gas discharges in microgaps.

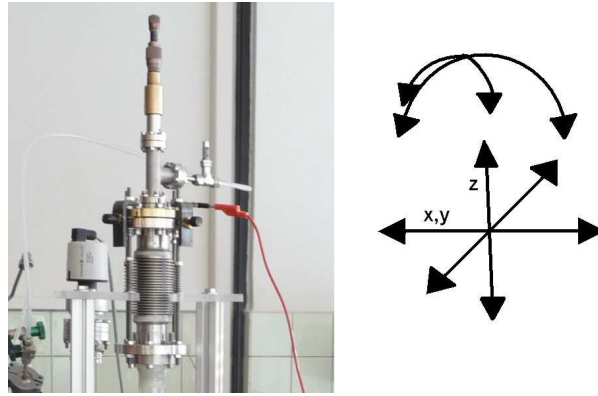


Fig. 18.3. The upper part of the apparatus.

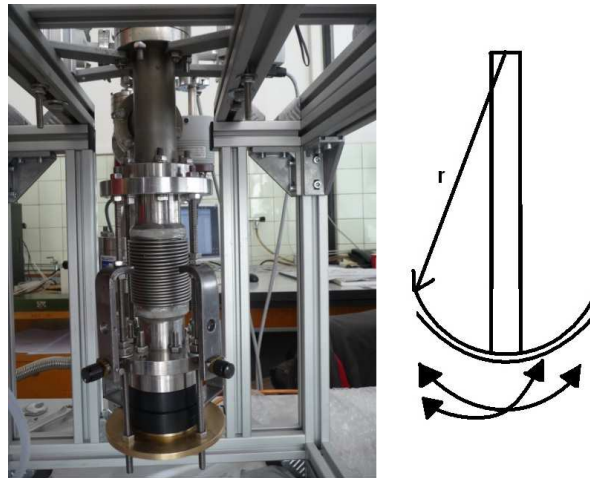


Fig. 18.4. The bottom part of the apparatus.

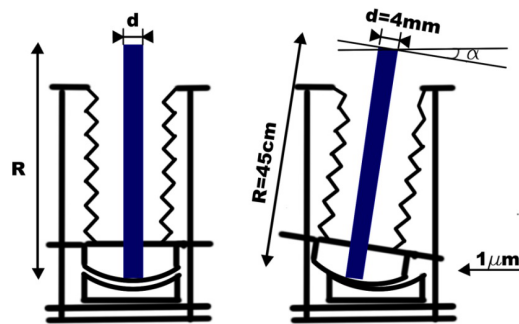


Fig. 18.5. The scheme of the bottom system used for ultra fine tilting.



Fig. 18.6. Molybdenum electrodes with Bruce profile.

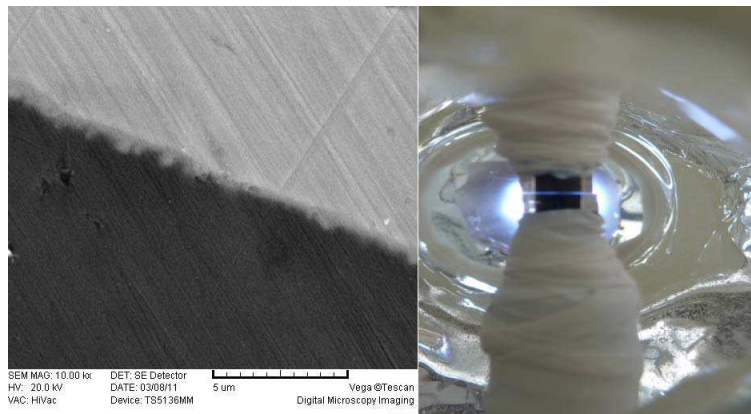


Fig. 18.7. Molybdenum electrodes melting in the glass SEM: The picture of the surface (left) and real view of the electrodes in vacuum chamber (right).

procedures were applied. One of the electrodes was fixed while the other movable with micrometer scale linear feed-through. The  $0\ \mu\text{m}$  distance between them was established by checking the electrical contact between the electrodes and then the movable electrode was pulled away by the means of the micrometer screw at the upper electrode. The electrodes were carefully mechanically polished, chemically cleaned and washed in an ultrasonic bath. The edges of the electrodes were rounded in order to avoid the fringing fields. Both electrodes were equipped with a dielectric cap (dielectric breakdown strength =  $13.8\ \text{kV/mm}$ ) to prevent the ignition of the discharge at longer path at low pressures. The quality of the surface has been measured using SEM. The average roughness of the electrode was better than  $0.25\ \mu\text{m}$ , because the finest diamond paste has  $0.25\ \mu\text{m}$  grain size.

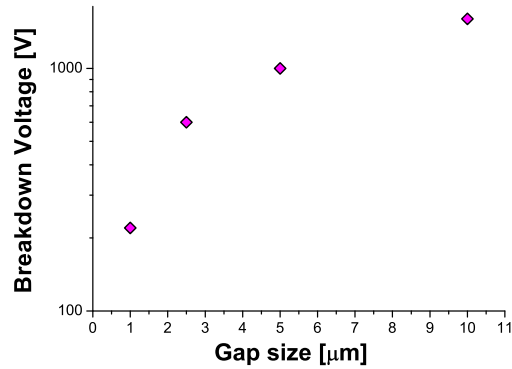


Fig. 18.8. The breakdown voltage curve measured by 485 Picoammeter Keithley at the pressure of  $1.5 \times 10^{-5}$  Torr. The current limit was set to  $2 \mu\text{A}$ .

## 18.2 Measurements of the breakdown voltage

The measurements of DC breakdown voltages was based on the time dependence of the potential difference across the discharge tube using a digital oscilloscope [134, 64, 88, 103]. As a first step, a very slowly increasing potential ( $\dot{0}.5 \text{ V/s}$ ) was applied to one of the electrodes. The potential across the discharge tube was increasing until the breakdown occurred. Due to the discharge breakdown, the potential across the discharge tube decreases rapidly and the breakdown voltage was determined from the maximum potential achieved across the discharge gap.

There are several key issues in the experimental procedures for measurements of the electrical breakdown voltages. The first one is ensuring that the measured breakdown voltage is associated with the Townsend discharge, rather than detection of the higher breakdown voltage associated with streamer. In general, it is hard to strictly define the breakdown voltage of microdischarges in the left hand side of the Paschen curve (small values of  $pd$ ) due to other process, such as field emission. For the left side of the Paschen curve we have defined breakdown voltage as potential difference between the electrodes, at discharge current of  $80 \mu\text{A}$ .

The test measurements were performed at low pressure of  $1.5 \times 10^{-5}$  Torr (background pressure of the system). The breakdown voltage values for  $1 \mu\text{m}$ ,  $2.5 \mu\text{m}$ ,  $5 \mu\text{m}$  and  $10 \mu\text{m}$  are 220 V, 600 V, 1000 V and 1600 V, respectively as depicted in Figure 18.8. For the gap size of  $1 \mu\text{m}$ , the breakdown voltage is estimated with the accuracy of around 20%, while for the separation of  $10 \mu\text{m}$ , the accuracy is 10 – 15%. The lowering of the breakdown voltage with decreasing the gap size is closely related to the electron field emission effect. For electric fields across gaps less than  $5 \mu\text{m}$ , the electric field becomes quite large and electrons can tunnel through the deformed surface potential barrier due to field emission [104, 165]. Electrons from field emission are one reason why breakdown

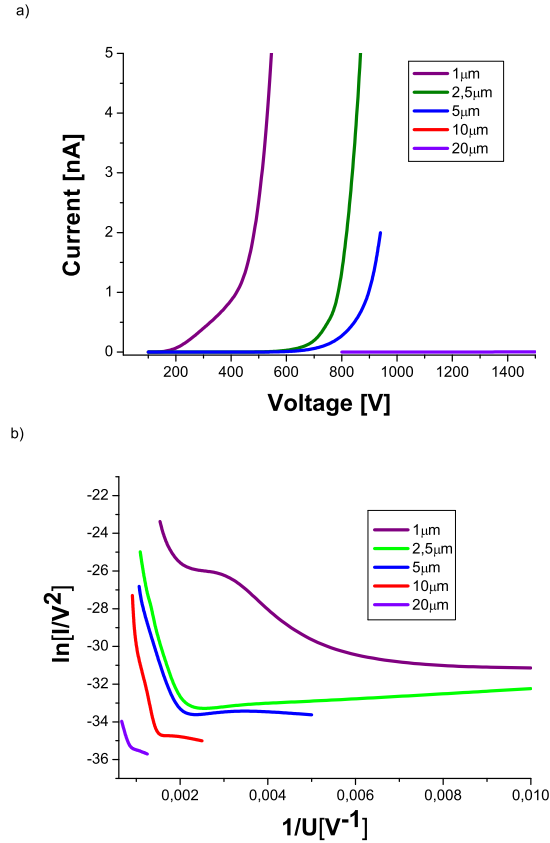


Fig. 18.9. a) The volt-ampere characteristics measured at the pressure of  $1.5 \cdot 10^{-5}$  Torr and b) the Fowler-Nordheim plots. The gap sizes varying from 1  $\mu\text{m}$  to 20  $\mu\text{m}$ . The current limit was set to 2  $\mu\text{A}$ .

and sparks occur in a vacuum, which of course is not possible if one only considers the Townsend Avalanche mechanisms for gas ionization used to generate the Paschen curve.

### 18.3 Measurements of the volt-ampere characteristics

The volt-ampere characteristics were recorded using AD card (National Instruments NI USB-6211) with sampling frequency 10 kHz and averaging 200 or 10 samples. The discharge current was limited to 2 mA for protection electrode, while resistor  $R_2$  where the current was measured was always 520  $\Omega$ . The value of the resistor  $R_1$  usually was 300 k $\Omega$ .

The volt-ampere characteristics recorded at the pressure of  $1.5 \cdot 10^{-5}$  Torr and the Fowler-Nordheim plots are shown in Figure 18.9 [64]. For the gap of 1  $\mu\text{m}$  and voltages greater than 150 V, there is a significant increase in the current that becomes more

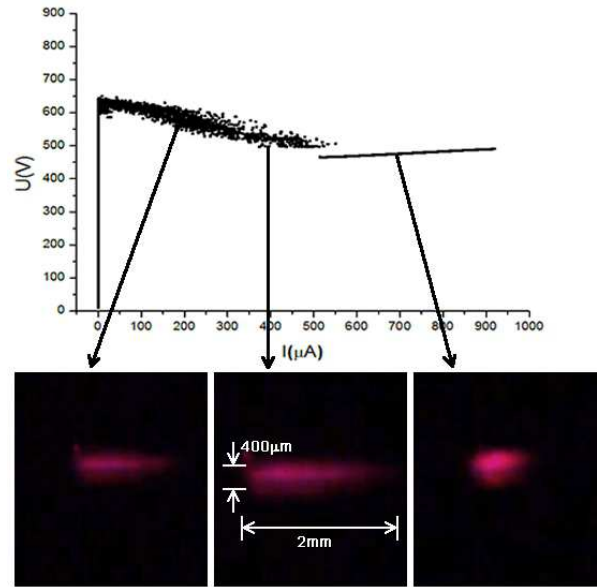


Fig. 18.10. Images of the contraction of discharges and the corresponding volt-ampere characteristics recorded at the pressure of 20.85 Torr and the gap size of  $400 \mu\text{m}$  in water vapor.

evident as breakdown is approached. The current starts at around  $0.5 \mu\text{A}$  (resolution of AD card) and then increases rapidly. As already emphasized, when the electric field generated in the micro gaps becomes sufficiently strong, the electrons are liberated from the surface by quantum mechanical tunneling. In that case, even if the mean free path of the electrons is longer than the distance between the electrodes and electrons therefore can not ionize atoms, a breakdown occurs. If the origin of the current is the field emission, a plot of  $1/V$  vs.  $\ln(I/V^2)$  should yield a straight line with a negative slope that is proportional to the work function of metal. This plot is known as the Fowler-Nordheim (F-N) plot and can be used to determine the mechanism of the electron emission. Figure 18.9b represents F-N plot that corresponds to the volt-ampere characteristics shown in Figure 18.9a. The negative slopes of the F-N plots indicate that field emission is the main source of the current close to breakdown.

The dominant processes taking place during the breakdown could be recognized on the basis of the volt-ampere characteristics and the structure of the discharge. Figure 18.10 demonstrates the connection between the volt-ampere characteristics of the discharge recorded at a fixed pressure, but for different gap sizes and the images of the discharge for typical regimes of non-equilibrium discharges in case of water vapor. For discharge current up to  $500 \mu\text{A}$  an oscillating regime exists. With further increasing of the current, the discharge was becoming stable (some kind of plateau region in V-I characteristics) which was observed optically like contraction of the discharge and electrically as a small voltage drop.

The time dependence of the breakdown at the at 20.85 Torr and  $80 \mu\text{m}$  is presented in

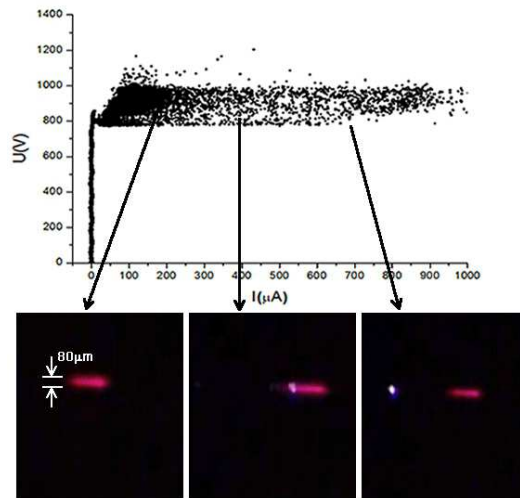


Fig. 18.11. Volt-ampere characteristics and images of the spreading of discharges at 20.85 Torr and  $80 \mu\text{m}$ .

Figure 18.11. The applied voltage was increased and the current-voltage characteristics was recorded. When the breakdown occurred, the discharge immediately changed to oscillating regime. With increasing voltage the current continued to increase. Thus, the discharge spread and the voltage remained in the same range of oscillation. With sharp increase of the discharge current, the voltage across the discharge gap dropped below the extinction voltage within a very short time, thus ending the discharge. Subsequently, the potential difference between electrodes again increased until the firing voltage of spark discharge was achieved as illustrated in Figure 18.12. Regions of spark creepage in which the charges are predominantly of one sign induce charges of opposite sign on the surface of the dielectric and consequently the spark channels spread over the surface of the dielectric.

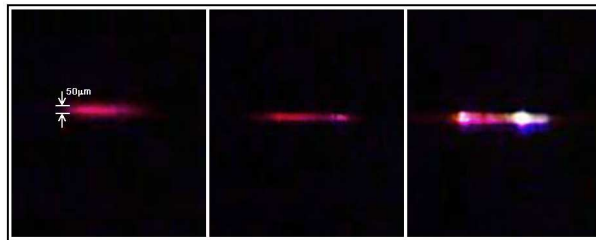


Fig. 18.12. Sparking observed in glow discharge for the gap size of  $50 \mu\text{m}$  and the gas pressure of 24.15 Torr.

## 19 Simulation technique

Particle simulation method has its roots in the pioneering work of Dawson[171] and Buneman[172] in the late 50's. In these basic physics models, space charge was computed from Coulomb's law with particles moving in periodic systems. It was shown that when appropriate methods are used, relatively small systems of a few thousand particles can simulate the collective behavior of real plasmas, thus the kinetic computational plasma physics was established.

In the first kinetic models Coulomb's law was computed for each particle yielding an  $N^2$  operation for  $N$  particles. A big step in improving computation was made with imposing a computational mesh on which to compute Poisson's equation. These methods were referred to as "particle-in-cell" (PIC) and were capable of simulating systems with much more particles resulting from the fact that number of operations was decreased from  $N^2$  to  $N \log N$ .

The PIC scheme was soon formalized and written into codes, and classic texts were published by Birdsall and Langdon [173] and Hockney and Eastwood [174] which remain eminent to the present. The rapid development of PIC codes followed, especially by the Plasma Device Workshop from Berkeley university by C K Birdsall, T Crystal, S Kuhn and W Lawson. This resulted in more rigorous treatment of interactions between the plasma and the boundaries, inclusion of external circuits[175] with improved accuracy to the second order and self-consistent solvers[176]. Collision treatment of charged particles with neutral particles with simple cross section was introduced by Boswell[177] later refined to more realistic differential cross sections by Vahedi and Surendra[178]. Commercial PIC codes including graphical user interface and code maintenance were available, detailed description of this codes was given by Verboncoeur[180]. These codes written in plan C language were later transferred to the object-oriented modeling paradigm[181]. At the present, two- and three- dimensional PIC codes are run on massively parallel platforms using up to  $10^{10}$  particles.

### 19.1 Modeling with the PIC algorithm

The PIC technique drastically improves the computer runtime enabling simulation of real systems. The simulation of a complete systems in every detail is not possible considering the number of particles and binary interactions between every combination of two particles. The calculation of binary interactions is drastically reduced by introducing the computational mesh, as was commented before. Nevertheless a further reduction in number of operation is still needed as the number real particles in a real laboratory plasma system is far beyond any computing power available today. The scaling of particles is thus implemented, a technique in which the number of particles is reduced in consideration of a statistically meaningful ensemble representing all the group phenomena. The scaling is implemented to reduce the number of particles, thus for example one scaled or "superparticle" is representing  $10^5$  real particles in the system.

In the simulated space, a mesh of points of charge and current density is computed on the base of the superparticles positions and speeds. Coulomb interaction between the particles is approximated by the interaction of the particles with the charge and

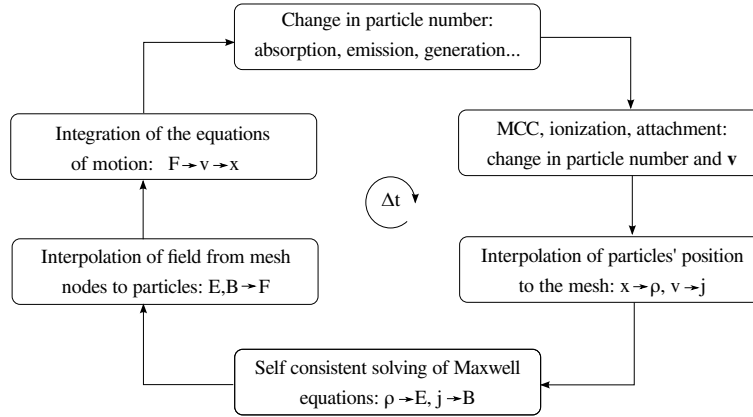


Fig. 19.1. Schematic for the PIC simulation.

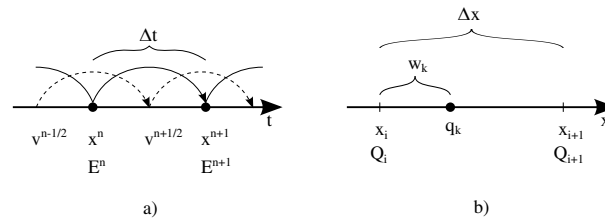


Fig. 19.2. Discretization of time and space. a) Schematic for the leapfrog. Charge density  $\rho$  and potential  $\Phi$  are defined at the same temporal positions as  $x$ ; current density  $j$  and magnetic field  $B$  are defined at positions of the velocity  $v$ . b) Schematic of the weighing the position of one particle  $k$  to neighboring mesh nodes  $i$  and  $i + 1$ .

current from the mesh nodes. When the force on every particle is known a self-consistent method of solving equations of motion and equations of field pushes the simulation in time. Schematically the PIC algorithm is presented in the Figure 19.1 in which a time-step of  $\Delta t$  is the simulated time shift of the whole system represented by particles and electromagnetic field.

To keep it simple here we will analyze one dimensional model with motion in three dimensions. That is model in which the spatial change of electric field is only in one direction and the magnetic field is perpendicular to the electric field. For time integration a "leapfrog" center different integration scheme is used, in which a particle positions and velocities are offset in time by  $\Delta t/2$  as shown in Figure 19.2.a. According to the equations of motion, an advance in time is performed by time integration of the discrete leapfrog

Newton-Lorentz equations:

$$\frac{\mathbf{v}^{t+\Delta t/2} - \mathbf{v}^{t-\Delta t/2}}{\Delta t} = \frac{q}{m} \left( E^t + \frac{\mathbf{v}^{t+\Delta t/2} + \mathbf{v}^{t-\Delta t/2}}{2} \times \mathbf{B}^t \right), \quad (19.1)$$

$$\frac{\mathbf{x}^{t+\Delta t} - \mathbf{x}^t}{\Delta t} = \mathbf{v}^{t+\Delta t/2}. \quad (19.2)$$

Usually a calculation scheme of Boris[182] is used to avoid the calculation of the full cross product. This method also known as Boris rotation doesn't allow the magnetic field to heat the particles.

Particle weighing to the mesh nodes can be done in a number of ways. Here we show the most simple linear interpolation, which for electrostatic model with mesh shown in Figure 19.2.b is represented with the equations:

$$Q_i = \sum_k q_k \left( 1 - \frac{w_k}{\Delta x} \right),$$

$$Q_{i+1} = \sum_k q_k \frac{w_k}{\Delta x},$$

where the summation is done for all the particles positioned between the nodes  $i$  and  $i + 1$ .

Considering the electrostatic case, the source terms and potentials are given at mesh nodes. The Poisson's equation gives the relation between the charge density and potential:

$$\nabla \cdot \varepsilon \nabla \Phi(x, t) = \rho(x, t). \quad (19.3)$$

Which can be solved using a center difference in a linear and homogeneous isotropic medium:

$$\frac{\Phi_{i+1} - 2\Phi_i + \Phi_{i-1}}{\Delta x^2} = -\frac{\rho_i}{\varepsilon}. \quad (19.4)$$

This system of equations is defined as long as we know the boundary conditions, that is the potential and charge of the electrodes. For a system completely enclosed with metal electrodes the potential can be separated into Poisson and Laplace parts:

$$\Phi = \Phi_P + \Phi_L,$$

$$\nabla \cdot \varepsilon \nabla \Phi_P = \rho, \quad (19.5)$$

$$\nabla \cdot \varepsilon \nabla \Phi_L = 0, \quad (19.6)$$

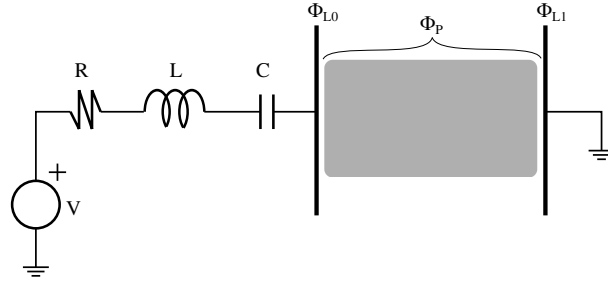


Fig. 19.3. External circuit and potentials: Laplace part  $\Phi_L$  and Poisson part  $\Phi_P$ .

where the boundary condition for equation (19.5) becomes  $\Phi_P = 0$  for all boundaries. The resulting potential of the electrodes  $\Phi_L$  can be solved in coupling with the external electric circuit, that is for charges and potentials of the electrodes and treating the plasma as neutral medium (equation (19.6)). The superposition of these two solutions gives the plasma potential and the electrodes potential in connection to the external circuit figure 19.3. By completing the solution of Poisson's equations particles can be pushed to the next time step after which the whole described process repeats. Treatment of the collisional processes is easily achieved using the Monte Carlo Collision technique (MCC) and it doesn't require additional changes in the described PIC algorithm.

### 19.1.1 Monte Carlo module

Every kinetic simulation algorithm beside the movement of particles and the field solver must also have some kind of collision treatment. The collision is an event in which the velocity vector of the particle changes, this can be due to change of the direction of the vector (elastic scattering) or the magnitude and direction of the velocity vector (inelastic scattering). The most common way to treat a collision is the Monte Carlo algorithm, which is based on a random number generation. A collision for a particle has happened when a random generated number satisfies some condition dictated by the collisional cross section, the magnitude and direction of the velocity vector and the background gas density. Considering the particle speed, a collision probability must be calculated for every particle in every time step. This algorithm can be further simplified by using a null collision scheme [178, 180].

In the Monte Carlo method the null collision cross section for a particle specie was introduced to the set of cross sections so that the total cross section is constant function of the velocity. Let us consider a total cross section for the interaction of the particle (without the null collision)  $\sigma_T(\epsilon)$ , it is a function of the particle energy  $\epsilon$ . Based on this we choose the maximum value of the collisional frequency  $\nu_{max}$ :

$$\nu_{max} = n_g \max_{\epsilon} [\sigma_T(\epsilon) \nu(\epsilon)], \quad (19.7)$$

where  $n_g$  is the gas density and  $\max_{\epsilon} [\sigma_T(\epsilon) \nu(\epsilon)]$  is the value of the maximum of the cross

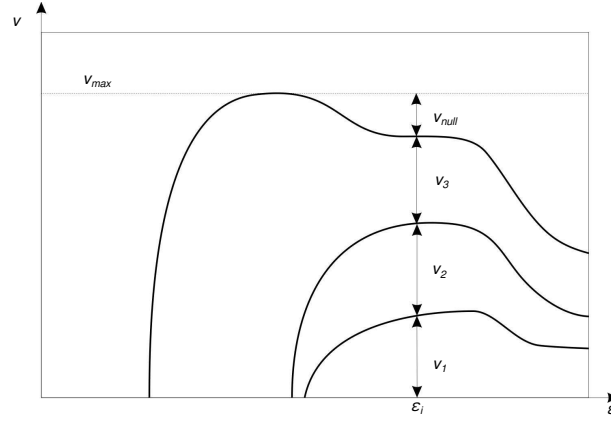


Fig. 19.4. Collisional frequency versus particle energy. On the graph values are given for an energy  $\epsilon_i$ .

section. The maximum probability for collision of a particle in one time step  $P_T$  is:

$$P_T = 1 - \exp(-\nu_{max} \Delta t) \quad (19.8)$$

Considering the maximum probability is the same for every particle, we can randomly choose  $P_T N_s$  particles that could have collided ( $N_s$  being the number of super particles). By doing this we have speeded up the collisional algorithm  $1/P_T$  times, as we don't have to calculate the probability for every particle. Further we choose the type of collision for each of these particles (see Figure 19.4) based on its energy  $\epsilon_i$  and a random number  $R \in [0, 1]$ :

$$R \leq \nu_1(\epsilon_i)/\nu_{max} \quad \dots \quad 1. \text{ type of collision,} \quad (19.9)$$

$$\nu_1(\epsilon_i)/\nu_{max} < R \leq (\nu_1(\epsilon_i) + \nu_2(\epsilon_i))/\nu_{max} \quad \dots \quad 2. \text{ type of collision,} \quad (19.10)$$

$\vdots$

$$\sum_j \nu_j(\epsilon_i)/\nu_{max} < R \quad \dots \quad \text{null collision,} \quad (19.11)$$

Based on the selected process the particle is scattered and in case of generation - new particles are generated. Described Monte Carlo null collision algorithm is very important for the simulation of plasmas as it governs the creation and loss of particles in the gas. Although some plasmas can be sustained from other types of particles generation (generation of particles from the walls) the majority of plasmas are sustained from the ionization of the background gas. This is why the collisional algorithm is the most vital part of the kinetic simulation of plasmas.

### 19.1.2 Mobility Calculations using Monte Carlo Collisions

The mobilities of the ions and electrons are encountered frequently in analytic treatments of plasma. Usually, the values of the mobilities are obtained from the experiments. The PIC/MCC methodology may also be used to obtain the mobilities of electrons and ions with known collision cross-sections for their interactions with neutrals at chosen values of electric field strength and pressure. The mobility of a charge particle is defined from the momentum equation with the assumption of equilibrium with the electric field:

$$m \left( \frac{\partial \mathbf{v}}{\partial t} + (\mathbf{v} \nabla) \mathbf{v} \right) = 0 = q\mathbf{E} - \nu_m m \mathbf{v}, \quad (19.12)$$

$$\mathbf{v} = \frac{q}{\nu_m m} \mathbf{E} = \mu \mathbf{E}, \quad (19.13)$$

where  $q$  is the charge of the particle,  $\nu_m$  is the momentum transfer collision frequency and  $m$  is the reduced mass of the system ion-neutral particle.

### 19.1.3 Boundary and simulation conditions

The simulation parameters were based on the experimental conditions mainly. Choices of the boundary conditions depend on the physical conditions of the boundary walls and electrodes. When an electron reaches the boundary, it is assumed to be absorbed. For an ion, it is also assumed to be adsorbed, but the secondary electrons may be emitted with a probability depending on the impinging ion energy.

Depending on the gas pressure, the time step  $dt$  was varied between  $10^{-18}$  s and  $10^{-16}$  s consuming a lot of time for running each case. The gap size was varied from  $1 \mu\text{m}$  to  $100 \mu\text{m}$ . One million computer particles was used as the initial number in the simulation. In order to determine the breakdown voltage, we use the fact that the breakdown is not an instantaneous phenomenon, it appears over a finite period of the time when the violation of the balance between the creation of charged species by ionization and their losses (via collisional processes and diffusion to the walls) occurs. For each value of the gas pressure, the time development of the electron density was observed and depending on its increasing or decreasing nature, the interval in which the breakdown occurs could be found through trial and error process. Thus, for each value of the gas pressure a number of calculations were needed.

## 19.2 Calculations of the ionization coefficients

Majority of the calculations, presented here, were done using PIC/MCC code, except the ionization coefficients that were calculated using Bolsig++ code [183]. An overall description of the code can be found in [183], so only the main characteristics of the code will be given here. Bolsig++ code is based on the solution of the Boltzmann equation in the Two Term Approximation (TTA) scheme enabling user friendliness and fast calculations. The basic idea under the TTA is the representation of the electron distribution by the first two terms of the expansion in spherical harmonics in velocity space. In a constant electric field, the solution for the Electron Energy Distribution

Function (EEDF) can be expressed as a function of the reduced electric field  $E/N$  (the ratio of the electric field to the gas density). The TTA fails at high values of  $E/N$  since the EEDF becomes highly anisotropic. It was straightforward to perform calculations for the pure gases or gas mixtures, except for dry air.

The sets of the cross sections for nitrogen, oxygen, argon and carbon dioxide include 25, 16, 3 and 13 processes, respectively. During the calculations for dry air, it was considered as a mixtures of gases, mainly nitrogen and oxygen, but containing much smaller amount of argon, carbon dioxide and very small amounts of other gases. In our calculations, we assumed that dry air is composed of 78.08%  $N_2$ , 20.95%  $O_2$ , 0.93% Ar and 0.04%  $CO_2$ . In the calculations we have used cross sections for 57 elastic and inelastic electron-impact collisional processes. However, in the Bolsig++ code, these cross section data are not extrapolated properly at high energies which may cause some errors in calculations.

## 20 Results for microdischarges

The previously described experimental, theoretical and simulation techniques have been extensively applied in order to study fundamental mechanisms beyond the electrical discharges in the microgaps. The breakdown voltage curves and volt-ampere characteristics were recorded for numerous gases and gas mixtures for the micrometer gap size range. The observed effects of the field emission on the secondary electron production and thereby on the breakdown characteristics in microgaps were theoretically studied and modeled. We compared the results obtained using different techniques as well as with the data available in the literature. By fitting the of the experimental data, realistic values of the effective yield in microgaps were obtained for a number of gases. The obtained results provide better insight into the role of the enhancement of the secondary electron emission due to high electric field generated in microgaps.

### 20.1 Argon

The dependence of the DC breakdown voltage on the  $pd$  product for different electrode gaps (from  $1\ \mu\text{m}$  to  $100\ \mu\text{m}$ ) is plotted in Figure 20.1. As can be observed, for the gap sizes smaller than  $20\ \mu\text{m}$  (circles and diamonds) exhibit departure from the standard scaling law. There is a good agreement between our experimental results for the gap size of  $100\ \mu\text{m}$  (solid squares) and the experimental data for the centimeter gaps taken from (black line) [19]. This demonstrates that field emission plays no role for  $100\ \mu\text{m}$  gap sizes.

The breakdown voltage versus the gap size for a fixed gas pressure of 746 Torr is shown in Figure 20.2. As expected, the departure from the similarity law take place for the left hand branch when the electron mean free path is comparable to the interelectrode

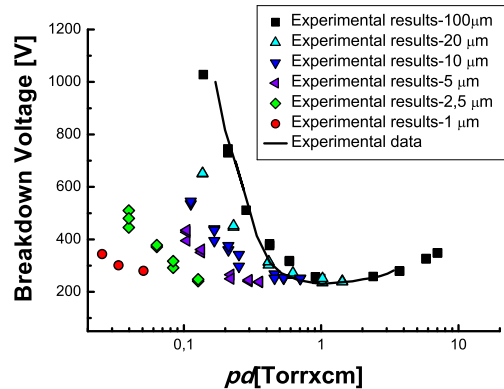


Fig. 20.1. The DC breakdown voltage curves in argon discharges when the gap spacing was varying from  $1\ \mu\text{m}$  to  $100\ \mu\text{m}$  [184], line represents experimental data from [19] .

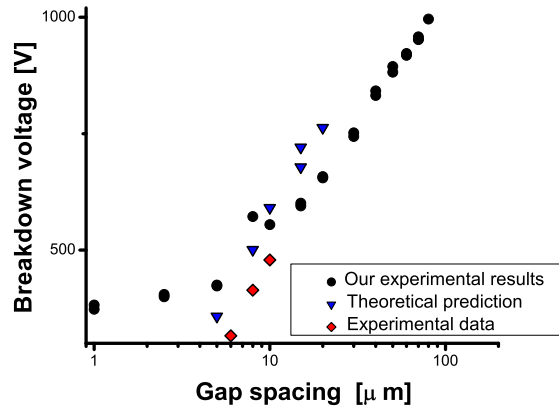


Fig. 20.2. The DC breakdown voltage in argon versus the gap size  $d$ , for a fixed pressure of 746 Torr. Diamonds data are from [185] and theoretical data from equation (17.1).

separation. There are similar trends between our experimental results (circles) and the available experimental data [185] (diamonds) and simple theoretical predictions based on the expression (17.1). The lower breakdown voltages obtained in our measurements can be attributed to the differences between the electrode materials.

Following the procedure described in [186] and using the experimental breakdown voltage curves from in Figure 20.1, the evaluated values of the effective yield of secondary electrons as function of the  $E/p$  ratio is presented in Figure 20.3a. The yield of secondary electrons is called 'effective' because under discharge conditions many particles can be responsible for the production of secondary electrons, such as argon ions, argon atoms, metastable, photons [96]. The procedure starts from the breakdown voltage measurements and determination of the reduced electric field as  $E/p = U_b/(pd)$ . After that, the  $E/p$  dependence of the ionization coefficient  $\alpha$  was used in order to calculate the effective yield based on the expression  $\gamma_{eff} = (e^{\alpha d} - 1)^{-1}$ . Finally, Figure 20.3b shows the values of the ionization coefficients estimated from the breakdown voltage curves measured for various gap sizes.

## 20.2 Hydrogen

The breakdown voltage as a function of  $pd$  product for the interelectrode separation from  $2.5 \mu\text{m}$  to  $100 \mu\text{m}$  is shown in Figure 20.4. For the gap of  $100 \mu\text{m}$ , results of our measurements (pink squares) satisfactorily agree with the data taken from the literature (open symbols) [19]. For the gap sizes below  $20 \mu\text{m}$  a rapid decrease of the breakdown voltage was observed below the minimum of the conventional Paschen curve, in the  $pd$  range where the electron mean free path is comparable to the electrode gap spacing. This is due to generation of the secondary electrons in the high electric field in the microgaps.

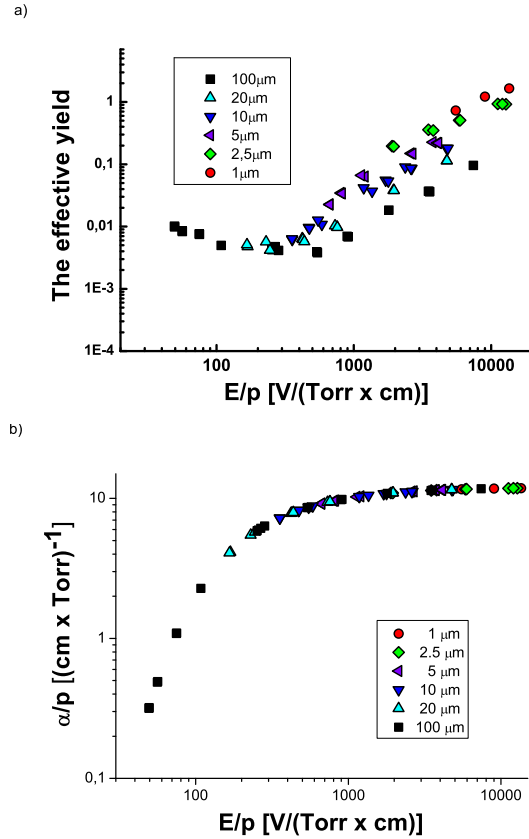


Fig. 20.3. a) The effective yield of secondary electrons as a function of the ratio  $E/p$ . b) The ionization coefficient for argon. Different symbols correspond to the data obtained from the breakdown voltage curves recorded for different gap sizes.

As can be seen from Figure 20.5 that shows the volt-ampere characteristic measured for the 1  $\mu\text{m}$  gap and the pressure of 737 Torr (black symbols), the influence of the enhancement factor  $\beta$  on the current density is also significant. For this volt-ampere characteristic the best agreement between theoretical predictions and experimental data can be obtained with for  $\beta$  values between 20 and 25.

From the breakdown voltage curves shown in Figure 20.6 and following the procedure described in [186], the dependence of the effective secondary electron yield on the reduced electric field  $E/p$  has been determined and presented in Figure 20.6a. Figure 20.6b contains the values of the ionization coefficient determined from the breakdown voltage curves recorded for different gap sizes. In line with the expectations, the lowest values of the yield were obtained for the interelectrode separation of 100  $\mu\text{m}$ , while the values of the yield increase with the reduction of the gap size. The effective yields estimated from

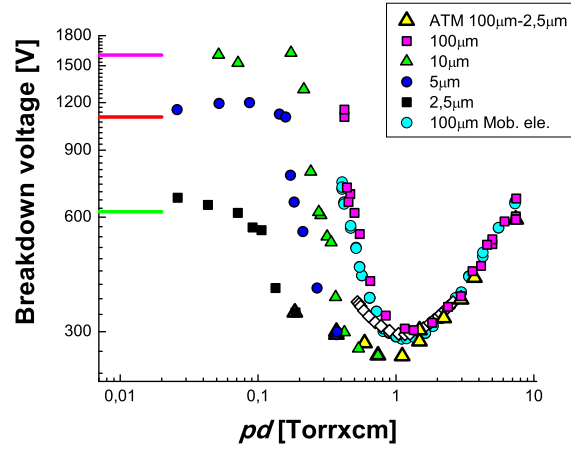


Fig. 20.4. The breakdown voltage curves in DC hydrogen discharges with the gap spacing varying from  $2.5 \mu\text{m}$  to  $100 \mu\text{m}$ , open symbols represent experimental data from [19].

our measured breakdown voltage curves satisfactorily agree with the data taken from [187].

Table 20.1) contains the values of the effective secondary electron yield  $\gamma_{eff}$  in hydrogen estimated for different electrode gap sizes. For the gap spacing of  $100 \mu\text{m}$  and  $50 \mu\text{m}$ , the values of the effective yield  $\gamma_{eff}$  are very similar to those published by Raizer for the centimeter distances [187]. The maximum value of the effective yield  $\gamma_{eff}$  exceeds 0.1, for  $10 \mu\text{m}$  gap and  $5 \mu\text{m}$ . On the other hand, for the gaps of  $2.5 \mu\text{m}$  and  $1 \mu\text{m}$ , the effective secondary electron yields are much higher than 1 due to field emission effect.

Gap [ $\mu\text{m}$ ]	$(\gamma_{eff})_{\min}$	$(\gamma_{eff})_{\max}$
100	$1.8 \times 10^{-4}$	0.142
50	0.0026	0.184
20	0.036	0.35
10	0.14	0.9
5	0.39	1.08
2.5	1.04	2.08
1	2.17	6.39

Tab. 20.1. The minimum and maximum values of the effective secondary electron yield  $\gamma_{eff}$  for hydrogen estimated from the experimental data.

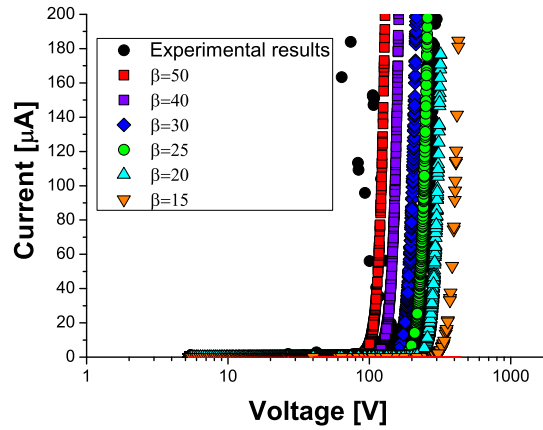


Fig. 20.5. The measured volt-ampere characteristics (black symbols) and the curves plotted in accordance with the F-N expression (14.1) for various  $\beta$  values for the gap of  $1\ \mu\text{m}$  and the pressure of 737 Torr.

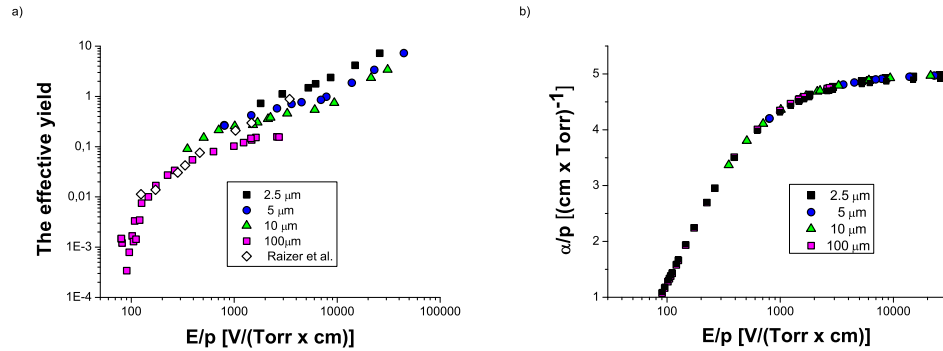


Fig. 20.6. a) The effective secondary electron yield versus the ratio  $E/p$  for hydrogen. b) The ionization coefficient for hydrogen. Different symbols correspond to the data obtained from the breakdown voltage curves recorded for different gap sizes.

### 20.2.1 Argon-hydrogen mixtures

The breakdown voltage curves in pure argon (black symbols), pure hydrogen (red symbols) and argon-hydrogen mixtures for the gap spacing of  $100\ \mu\text{m}$  are compared in Figure 20.7. As can be noticed, addition of the hydrogen to the argon gas resulted in the increase of the breakdown voltage. Breakdown voltage curves for the mixture that contains small amount of hydrogen exhibits similar properties (such as position of the minimum)

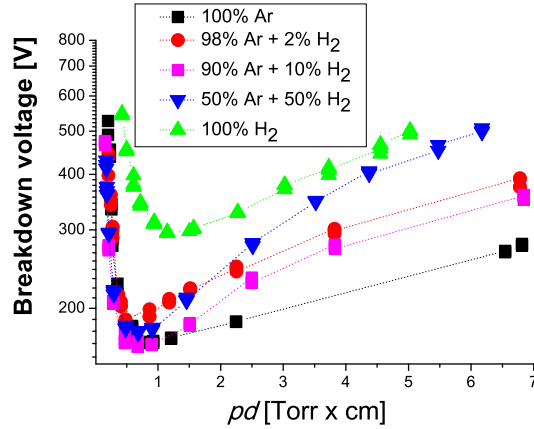


Fig. 20.7. The breakdown voltage against the  $pd$  product, for a fixed gap spacing of  $100\mu\text{m}$  for argon-hydrogen mixtures.

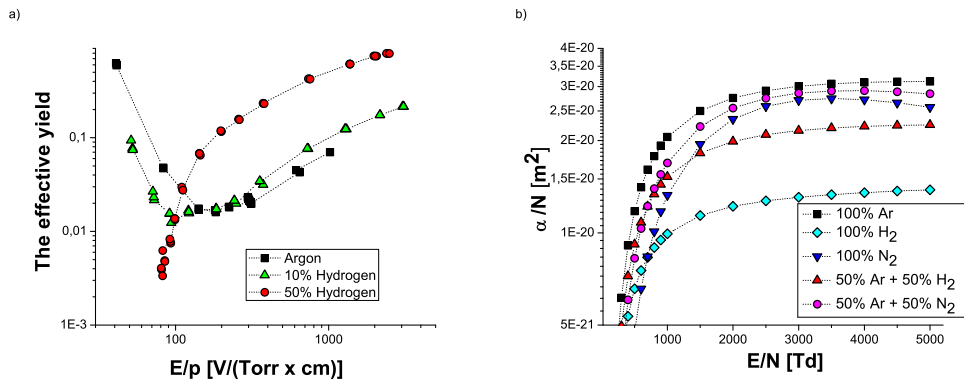


Fig. 20.8. a) The dependence of the effective yield on the reduced electric field  $E/p$  and b) the ionization coefficient for pure argon and argon-hydrogen mixtures.

as the breakdown curve for pure argon. However, as the amount of hydrogen increases, the breakdown voltage curves exhibit different behavior at the right hand side. In pure argon the minimum of the Paschen curve is lower than that of argon-hydrogen mixture. This can be explained by the fact that the secondary emission coefficient of hydrogen is lower than that of argon. This permits to extract more electrons in pure argon and thus decrease the breakdown voltage. On the other hand, the increase of the breakdown voltage curves observed in argon mixtures containing small amounts of impurities can be interpreted as being due to quenching collisions between argon metastables and impurity

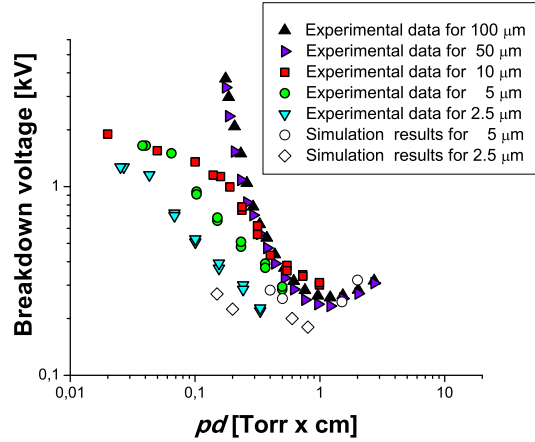


Fig. 20.9. The dependence of the DC breakdown voltage on the  $pd$  product in nitrogen. The experimental data are compared with the simulation results taken from [190].

particles. However, we should note, that the values of the breakdown voltages at the minimum depend on the concentration of hydrogen.

Figure 20.8a exhibits how  $\gamma$  coefficient depends on the reduced electric field  $E/p$  when hydrogen is added to the argon gas. Addition even of a small amount of hydrogen ( symbols) strongly affects the value of the yield. In the case of pure argon, there is similar trend and relatively good agreement between present values (black symbols) and those provided by Auday et al. [188]. Figure 20.8b shows the ionization coefficients for pure argon, pure hydrogen and mixture that contains different amount of hydrogen. It is obvious that addition of hydrogen leads to higher influence to the ionization coefficient.

### 20.3 Nitrogen

As can be deduced from Figure 20.9, the results for the gap sizes of  $100\ \mu\text{m}$  (black triangles) and  $50\ \mu\text{m}$  (violet symbols) are typically U-shaped with a minimum breakdown voltages of around 258 V and 288 V, respectively. As expected, the breakdown voltages for the  $10\ \mu\text{m}$  (red squares) and  $5\ \mu\text{m}$  (green circles) are lower but still obey the standard Paschen law. For the  $2.5\ \mu\text{m}$  gap size (down triangles), however, failure from the standard scaling law can be observed. The shape to the left of minimum would suggest that long path breakdown leads to the lowering of the breakdown voltages and departures from the Paschen law. We were able to estimate the ionization coefficients from the breakdown voltage curves for nitrogen (Figure 20.10).

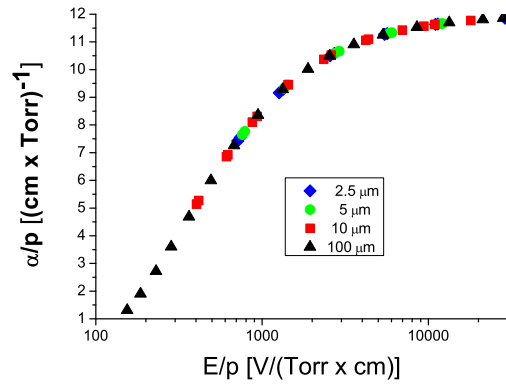


Fig. 20.10. The ionization coefficient against the reduced electric field  $E/p$  for nitrogen.

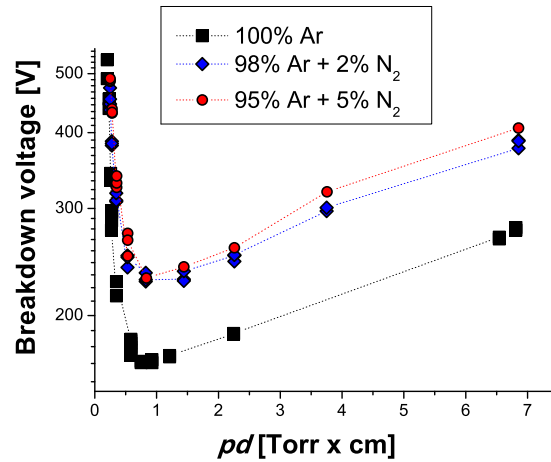


Fig. 20.11. The breakdown voltage curves for argon-nitrogen mixtures with a different amount of nitrogen. The gap size is  $100\ \mu\text{m}$ .

### 20.3.1 Argon-nitrogen mixtures

The breakdown voltage curves shown in Figure 20.11 demonstrate that even when a small percentage of nitrogen gas added to argon leads to higher breakdown voltages. At the right side of minimum of Paschen curve (higher values of the  $pd$ ) the effect of both impurities is noticeable.

Figure 20.12a leads to the conclusions that a small amount of nitrogen added to argon does not affect significantly the values of the ionization coefficients significantly, however,

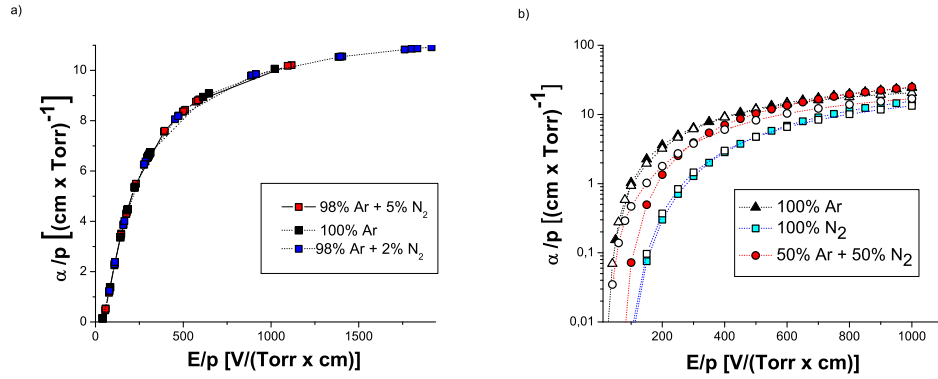


Fig. 20.12. The effect of nitrogen admixture to argon gas on the ionization coefficients. a) Determined from the measured breakdown voltage curves. b) Results calculated by using TTA [76] and compared with the values obtained using the formulas given in [90].

it allows to apply substantially higher values of  $E/p$ . On the other hand, Figure 20.12b demonstrates that ionization coefficients for gas mixtures composed of 50% of argon and 50% nitrogen (solid red symbols) are about halfway (in logarithmic scale) between the coefficients for pure argon (solid black symbols) and those for pure nitrogen (solid blue symbols). In spite of the limitation of the TTA, results of calculations (solid symbols) are in a good agreement with the results achieved by using expression provided by Marić et al. [90].

### 20.3.2 Argon-hydrogen-nitrogen mixtures

The dependence of the breakdown voltage on the  $pd$  product when a small amount (2%) of  $\text{H}_2$  and  $\text{N}_2$  are added to argon is depicted in Figure 20.13. The nitrogen addition to argon shifts the breakdown voltage at the minimum of the Paschen curve to higher voltages as compared to the addition of the same amount of  $\text{H}_2$ . At right site of minimum of Paschen curve (higher values of the  $pd$ ) the effect of both impurities is almost identical.

Figure 20.14a demonstrates that the addition of a small amount of hydrogen (circles) or nitrogen (diamonds) to argon gas causes the lowering of the effective yields compared to the yield for pure argon (squares). Figure 20.14b clearly shows that the ionization coefficients for gas mixture that contains 50% of argon and hydrogen (down triangles) or nitrogen (up triangles) are about halfway between the coefficients for pure argon (black squares) and those for pure hydrogen or nitrogen (solid blue symbols). On the other hand, addition of hydrogen leads to higher influence to the ionization coefficient. In spite of the limitation of the TTA, results of calculations (solid symbols) are in a good agreement with the results achieved by using expression provided by Marić et al. [90].

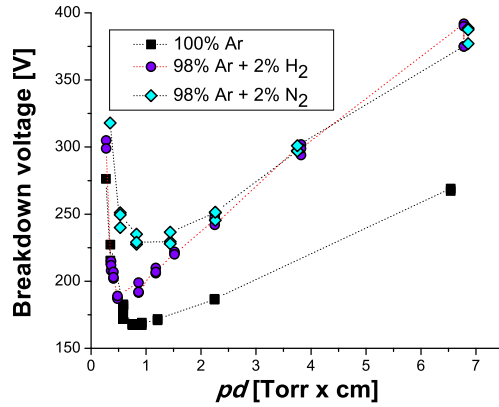


Fig. 20.13. The breakdown voltage curves when the same amount of (2%) of hydrogen (circles) and nitrogen (diamonds), are admixed to argon. Squares correspond to the experimental data taken from [189].

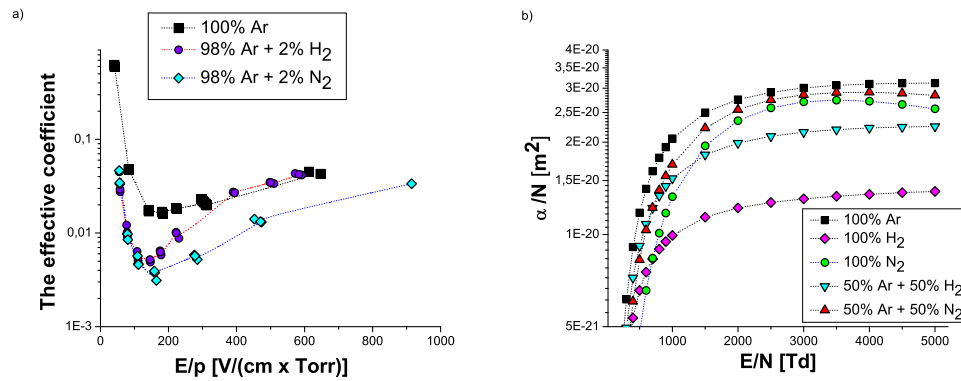


Fig. 20.14. The effect of hydrogen and nitrogen added to argon gas on the: a) the effective secondary electron yield and b) the ionization coefficients.

### 20.4 Air

The breakdown voltage curves for dry (triangles) and synthetic air with water vapor (circles) measured for the gap size of  $20\ \mu\text{m}$  are compared in Figure 20.15. Obviously, the breakdown voltage of air is influenced by the presence of the humidity. The water vapor has a higher breakdown strength than air, so a mixture of water vapor and air (i.e. higher humidity) has a higher breakdown voltage. Water also recombines very quickly

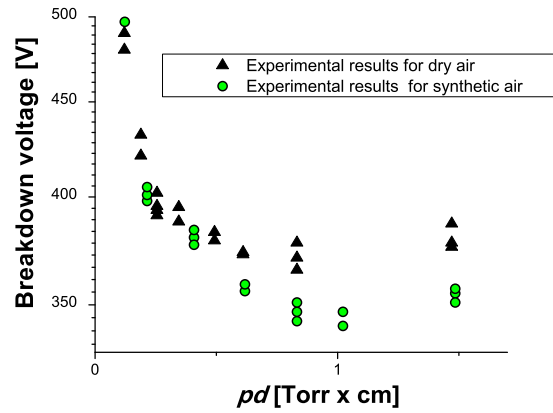


Fig. 20.15. The breakdown voltage curves for synthetic air with water vapor (triangles) and dry air (circles) recorded for the interelectrode separation of  $20 \mu\text{m}$ .

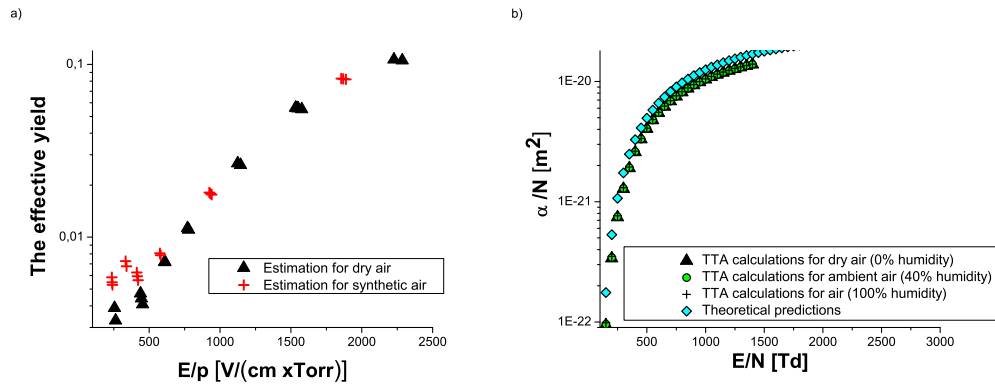


Fig. 20.16. a) The effective yield and b) the ionization coefficient against the ratio  $E/p$ , for dry (black triangles) and synthetic air with water vapor (red crosses).

after dissociation, which increases its breakdown strength.

The humidity also affects the transport parameters of air. Based on the experimental curves shown in Figure 20.15, the dependence of the effective yield on the  $E/p$  ratio both for dry air and synthetic air is determined and shown in Figure 20.16a. As can be observed, the effective yields for dry and synthetic air are similar except for lower  $E/p$  values.

In addition to the measurements, calculations of the ionization coefficients were performed for dry air (with no humidity), ambient air (humidity 40%) and air with high

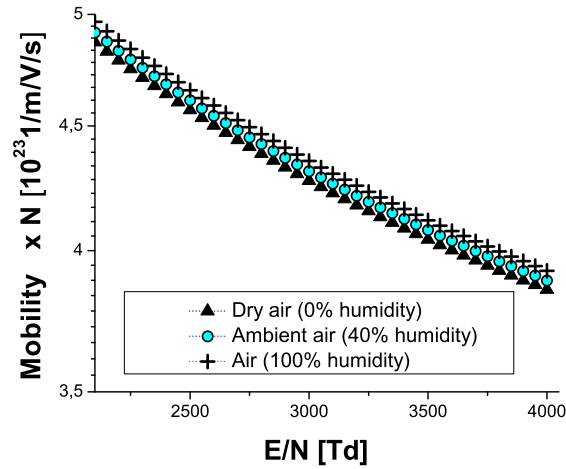


Fig. 20.17. The mobility versus the reduced electric field  $E/N$  obtained by Bolsig++ code. Triangles, circles and crosses correspond to results for air with 0% humidity, 40% humidity 100% humidity, respectively.

humidity (100%) and presented in Figure 20.16a. In accordance with the formula (4.12), the ionization coefficient for the mixture can be expressed as linear combination of ionization coefficient of the constituent gases weighted by corresponding abundances. Since in our study, 100% relative humidity in air corresponds to  $\approx 3.2$  vol%  $\text{H}_2\text{O}$ , its abundance is small so the presence of water will not change the ionization coefficient significantly.

Results of TTA calculations for the the dependence of the mobility on the reduced electric field  $E/N$ . Black triangles and circles represent results for dry air (0% humidity) and ambient air (40% humidity), respectively, while results for air with 100% humidity are shown by crosses. Obviously, the humidity has no great influence on the mobility.

## 21 Conclusions

There are still many questions that exist about the fundamental nature of micro-discharges and how they are similar to or different from their macroscale counterparts. One of the possible ways to achieve atmospheric pressure discharges which are still nonequilibrium is to operate at very small gaps which have to be of the order of few microns or less in order to reach minimum breakdown voltage and stable operation under low temperature conditions. This review is the results our efforts to provide better understanding of the non-equilibrium processes which occur in discharges generated in micrometer gap sizes during breakdown starting from our knowledge of the processes and scaling laws that are valid for the large scale systems.

At low pressures secondary electron emission plays an important role in determining the electrical breakdown. At low values of  $pd$  product, the ionization mean free path is larger than the electrode separation and most electrons are lost to the walls before ionizing, so higher applied electric fields are required to balance the energy loss. At high pressures, however, breakdown conditions are dominated by volume processes and relatively independent of surfaces conditions.

The breakdown of  $pd$  scaling law is essential in deciding whether one may proceed by extrapolating discharges with standard properties to micro discharges, atmospheric pressure discharges and high frequency discharges. It was found that electrical breakdown across sub-micron and micron gaps at atmospheric pressure results from the mechanisms other than the Townsend avalanche within an ionized gas and does not obey the Paschen law. These other mechanisms that are not considered in the theory behind the Paschen law are closely related to the phenomena of electron field emission and tunneling. As one may conclude the field emission will serve as a significant source of free electrons and will actually alter the way a discharge operates as well as its fundamental properties in regimes other than the breakdown point. Actually, field emitted electrons create an abundance of ions through collisional processes. These ions increase the field at the cathode, inducing increased field emission. This feedback mechanism ultimately leads to breakdown at applied voltages lower than those predicted by the Paschen law or vacuum breakdown theory. Kisliuk and Boyle has suggested the expression for the effective secondary electron yield when the ion-enhanced field emission is accounted for [104]. Determination of the parameters that appear in this expression, however, still remains very difficult task. Some often used models for the secondary electron emission provide unrealistically high values of the parameters with no physical meaning. Based on our measurements of the breakdown voltage characteristics of the electrical micro-discharges in various gases, we estimated the effective secondary electron yields  $\gamma_{eff}$  that correspond to microgaps. Semi-empirical expressions given here are valid for applied potentials up to breakdown voltage, at which ion-enhanced field emission begins to play a significant role.

Unlike centimeter gaps, the presence of field emission in a microdischarge provides a large source of cathode electrons that create an abundance of ions in the gap through ionizing collisions. When positive space charge densities in the gap become sufficiently large, the electric field at the cathode is increased and field emission current increases. In other words, mechanism of the electrical breakdown in the gaps less than a few mi-

rometers is similar to that of vacuum breakdown and is primarily the result of field emission from micro-protrusions on the cathode surface, which enhance the electric field by a factor  $\beta$ , as verified by a linear Fowler-Nordheim plot with a negative slope. The volt-ampere characteristics, measured in microgaps, can be fitted well with using F-N equation and appropriate value of the enhancement factor. Finally, the F-N theory has been very successful in many systems, not only for the planar geometry but also for small tips with the size of micrometers.

Nowadays modelling and computer simulations of gas discharges, especially microdischarges, are spreading within the plasma community, driven by the reduction in cost of computational resources. Of course, choosing the right model requires an understanding of the capabilities and limitations of the models and of the main physics governing a particular discharge. Since simulation results continue to be validated both by experiments and theoretical models, computer simulations can be used to improve understanding of plasma physics as an alternative to analytical models and laboratory experiments. It can be particularly important in situations when analytical complexity or achievements of experimental conditions prevent further analysis.

### Acknowledgments

The work has been carried out under Ministry of Education and Science Republic of Serbia O171037 and III41011 projects. This work has also been supported by the VEGA grant agency; project VEGA 1/0514/12, the Slovak Research and Development Agency Projects APVV-0733-11, DO7RP-0025-11, SK-SRB-0026-11 and COST CMST TD1208.

## References

- [1] A. C. Eckbreth, J. W. Davis: *Appl. Phys. Lett.* **21** (1972) 25
- [2] C. O. Brown, J. W. Davis: *Appl. Phys. Lett.* **21** (1972) 480
- [3] A. Franks: *J.Phys. E* **20** (1987) 1442
- [4] F. Charbonnier: *J. Vacum Sci. Technol.* **B16** (1998) 880
- [5] W. Oepts, H. Verhagen, W. J. M. de Jonge, R. Coehoom: *Appl. Phys. Lett.* **73** (1998) 2363
- [6] D. Ono, D. Y. Sim, M. Esahi: *J. Micromech. Microeng.* **10** (2000) 445
- [7] P. Dario, M. C. Carrozza, A. Benvenuto, A. Menciasci: *J. Micromech. Microeng.* **10** (2000) 235
- [8] T. Ito, T. Izaki, K. Terashima: *Thin Solid Films* **386** (2001) 300
- [9] A. Neumann: *J. Appl. Phys.* **90** (2001) 1
- [10] I. Tsuyohito, T. Kazuo: *Appl. Phys. Lett.* **80** (2002) 2648
- [11] J. Xiong, Z. Zhou, X. Ye, X. Wang, Y. Feng, *Sensors Actuators A* **108** (2003) 134
- [12] C. H. Chen, J. A. Yeh, P. J. Wang: *J. Micromech. Microeng.* **16** (2006) 1366
- [13] U. Kogelschatz: *Contribution to Plasma Physics* **47** (2007) 80
- [14] C. M. Du, J. Wang, L. Zhang, H. X. Li, H. Liu, Y. Xiong: *New Journal of Physics* **14** (2012) 013010
- [15] L. B. Loeb: *Fundamental Processes of Electrical Discharges in Gases* (J. Wiley and Sons, Inc., 1939)
- [16] M. J. Druyvesteyn, F. M. Penning: *Rev. Mod. Phys.* **12** (1940) 87
- [17] S. C. Brown, A. D. MacDonald: *Phys. Rev.* **76** (1949) 1629
- [18] L. J. Varnerin, S. C. Brown: *Phys. Rev.* **79** (1950) 946
- [19] J. M. Meek, J. D. Craggs: *Electrical breakdown of gases* (Oxford University Press, 1953)
- [20] R. G. Jr. Meyerand, A. F. Haught: *Phys. Rev. Lett.* **11** (1963) 401
- [21] P. Yu. Raizer: *Gas Discharge Physics* (Springer, 1991)
- [22] V. A. Lisovskiy, S. D. Yakovin, V. D. Yegorenkov: *J. Phys. D: Appl. Phys.* **27** (1994) 2340
- [23] H. B. Smith, C. Charles, R. W. Boswell: *Phys. of Plasmas* **10** (2003) 875
- [24] M. Radmilović-Radjenović, Z. Lj. Petrović: *Eur. Phys. J.D* **54** (2009) 445
- [25] M. Radmilović-Radjenović, B. Radjenović: *J. Phys. D: Appl. Phys.* **39** (2006) 3002
- [26] E. Wagenaars, M. D. Bowden, G. M. W. Kroesen: *Phys. Rev. Lett.* **98** (2007) 075002
- [27] T. Ficker: *J. Plasma Fusion Res.* **8** (2009) 744
- [28] D. Marić, N. Škoro, P. D. Maguire, C. M. O. Mahony, G. Malović, Z. Lj. Petrović: *Plasma Sources Science and Technology* **21** (2012) 3
- [29] J. C. T. Eijkel, H. Stoeri, A. Manz: *Anal. Chem.* **72** (2000) 2547
- [30] C. Wilson, Y. Gianchandani: *J. Microelectromech. Sist.* **10** (2001) 50
- [31] P. Kurunczi, J. Lopez, H. Shah, K. Becker: *Int. J. Mass Spectrom.* **205** (2001) 277
- [32] S. S. Yang, J. K. Lee, S. W. Ko, H. C. Kim, J. W. Shon: *Contrib. Plasma Phys.* **44** (2004) 536
- [33] L. Que, C. G. Wilson, Y. B. Gianchandani: *J. Microelectromech. Sist.* **14** (2005) 185
- [34] N. Škoro, N. Puač, S. Lazović, U. Cvelbar, G. Kokkoris, E. Gogolides: *Journal of Physics D:Appl. Phys.* **46** (2013) 47

- [35] S. Lazović, N. Puač, K. Spasić, G. N. Malović, U. Cvelbar, M. Mozetić, M. Radetić, Z. Lj. Petrović: *Journal of Physics D:Appl. Phys.* **46** (2013) 47
- [36] N. S. Xu, R. V. Latham: *High Voltage Vacuum Insulation: Basic Concepts and Technological Practice* (Academic Press, 1995)
- [37] I. Langmuir: *Proceedings of the National Academy of Sciences of the United States of America* **14** (1928) 627
- [38] F. Paschen: *Wied. Ann.* **37** (1889) 69
- [39] J. S. E. Townsend: *Electrons in Gases* (London:Hutchinson's. 1947)
- [40] L. H. Germer, F. E. Haworth: *Phys. Rev.* **73** (1948) 1121
- [41] F. L. Jones, C. G. Morgan: *Phys. Rev.* **82** (1951) 970
- [42] L. H. Germer: *J. Appl. Phys.* **30** (1959) 46
- [43] J. M. Torres, R. S. Dhariwal: *Nanotechnology* **10** (1999) 102
- [44] J. M. Torres, R. S. Dhariwal: *Microsystem Technologies* **6** (1999)6
- [45] M. Radmilović-Radjenović, B. Radjenović:*Plasma Sources Sci. Technol.* **17** (2008) 024005
- [46] M. Radmilović-Radjenović, B. Radjenović: *Europhysics Letters* **83** (2008) 25001
- [47] R. Tirumala, D. B. Go: *Applied Physics Letters* **97** (2010) 151502
- [48] A. Semnani, A. Venkatraman, A. A. Alexeenko, D. Peroulis: *Applied Physics Letters* **102** (2013) 174102
- [49] M. J. Kushner: *J. Appl. Phys.* **95** (2004) 846
- [50] Q. Liu, G. Ding, Z. Yang, B. Zhu, Y. Wang: *Journal of Micromechanics and Microengineering* **22** (2012) 075014
- [51] K. Yamamura, T. Mitani: *Surface and Interface Analysis* **40** (2008) 1011
- [52] K. Devi, S. C. Kumar, M. Ebrahim-Zadeh: *Optics Express* **21** (2013) 24829
- [53] T. H. Stievater, M. W. Pruessner, D. Park, W. S. Rabinovich, R. McGill, D. A. Kozak, R. Furstenberg, S. A. Holmstrom, J. B. Khurgin: *Optics Letters* **39** (2014) 969
- [54] N. N. Meeravali, K. Madhavi, S. J. Kumar: *Journal of Analytical Atomic Spectroscopy* **26** (2011) 214
- [55] Y. Rahmawan, L. Xua, S. Yang: *J. Mater. Chem. A* **1** (2013) 2955
- [56] A. Folch: *Introduction to BioMEMS* (CRC Press, 2012)
- [57] D. F. Farson, H. W. Choi, S. I. Rokhlin: *Nanotechnology* **17** (2006) 132
- [58] H. C. Kim, F. Iza, S. S. Yang, M. Radmilović-Radjenović, J. K. Lee: *Journal of Physics D: Appl. Phys.* **38** (2005) R283
- [59] Z. Lj. Petrović, S. Dujko, D. Marić, G. Malović, Ž. Nikitović, O. Šašić, J. Jovanović, V. Stojanović, M. Radmilović-Radenović: *Journal of Physics D: Appl. Phys.* **42** (2009) 194002
- [60] M. Jugroot: *Plasma Processes and Polymers* **6** (2009) 360
- [61] K. Aktas, S. Acar, B. G. Salamov: *Plasma Sources Science and Technology* **20** (2011) 045010
- [62] M. Radmilović-Radjenović, J. K. Lee, F. Iza, G. Y. Park: *J. Phys. D : Appl. Phys.* **2005** 950
- [63] M. Klas, Š. Matejčik, B. Radjenović, M. Radmilović-Radjenović: *Physics Letters A* **376** (2012) 1048
- [64] M. Radmilović-Radjenović, Š. Matejčik, M. Klas, B. Radjenović: *J. Phys. D : Appl. Phys.* **46** (2013) 015302

- [65] J. P. Boeuf, L. C. Pitchford: *IEEE Trans. Plasma Sci.* **19** (1991) 286
- [66] R. A. Stewart, P. Vitello, D. B. Graves: *J. Vac. Sci. Technol. B* **12** (1994) 478
- [67] A. Bogaerts, R. Aerts, R. Snoeckx, W. Somers, W. Van Gaens, M. Yusupov, E. Neyts: *Journal of Physics: Conference Series* **399** (2012) 012011
- [68] M. Shihab, A. T. Elgandy, I. Korolov, A. Derzsi, J. Schulze, D. Eremin, T. Mussenbrock, Z. Donko, R. P. Brinkmann: *Plasma Sources Sci. Technol.* **22** (2013) 055013
- [69] P. Colella, M. R. Dorr, D. D. Wake: *Journal of Computational Physics* **152** (1999) 550
- [70] C. Chiastra, S. Morlacchi, D. Gallo, U. Morbiducci, R. Cardenes, I. Larrabide, F. Migliavacca: *J. R. Soc. Interface* **6** (2013) 1742
- [71] C. K. Birdsall, A. B. Langdon: *Plasma Physics via Computer Simulation* (IOP Publishing Ltd, 1991)
- [72] Y. Xu, X. Qi, X. Yang, C. Li, X. Zhao, W. Duan, L. Yang: *Plasma Sources Science and Technology* **23** (2014) 015002
- [73] Y. A. Omelchenko, H. Karimabadi: *Journal of Computational Physics* **216** (2006) 153
- [74] H. B. Nersisyan, K. A. Sargsyan, D. A. Osipyan, M. V. Sargsyan, H. H. Matevosyan: *Armenian Journal of Physics* **4** (2011) 74
- [75] D. L. Bruhwiler, R. E. Giacone, J. R. Cary, J. P. Verboncoeur, P. Mardahl, E. Esarey, W. P. Leemans, B. A. Shadwick: *Phys. Rev. Spec. Top.- Acc. Beams* **4** (2001) 101302
- [76] G. J. M. Hagelarr, L. C. Pitchford: *Plasma Sources Sci. Technol.* **14** (2005) 722
- [77] H. Reather: *Electron Avalanches and Breakdown in Gases* (Butterworths, 1964)
- [78] M. J. Noy, A. D. Ernest: *Journal of Physics D: Applied Physics* **25** (1992) 1210
- [79] M. P. Fewell, S. C. Haydon: *Journal of Physics D: Applied Physics* **30** (1997) 1778
- [80] Yu. D. Korolev, G. A. Mesyats: *Physics of Pulsed Breakdown in Gases* (URO-PRESS, 1998)
- [81] H. C. Miller: *IEEE Trans. Elec. Insul.* **E1-26** (1991) 949
- [82] L. B. Loeb, A. F. Kip: *Journal of Applied Physics* **10** (1939) 142
- [83] H. Raether: *Zeitschrift fur Physik* **112** (1939) 464
- [84] M. Sato: *Bull. Yamagata Univers.* **25** (1999) 119
- [85] M. Radmilović-Radenović, Z. Lj. Petrović, G. Malović, D. Marić, B. Radjenović: *Czechoslovak Journal of Physics* **56** (2006) B996
- [86] A. A. Kruithoff: *Physica* **7** (1940) 519
- [87] L. M. Chain, G. D. Rork: *Phys. Rev.* **133** (1964) 1005
- [88] M. Radmilović-Radjenović, B. Radjenović, M. Klas, Š. Matejčik: *Mod. Phys. Lett. B* **26** (2012) 1250122
- [89] K. A. Klimenko, A. V. Kozyrev, Yu. D. Korolev, Yu. N. Novoselov: *Fizika Plazmy* **9** (1984) 196
- [90] D. Marić, M. Radmilović-Radjenović, Z. Lj. Petrović: *Eur. Phys. J. D* **35** (2005) 313
- [91] S. N. Sen, A. K. Ghosh: *Proc. Phys. Soc. B* **79** (1962) 293
- [92] G. Petraconi, H. S. Maciel, R. S. Pessoa, G. Murakami, M. Massi, C. Otani, W. M. I. Uruchi, B. N. Sismanoglu: *Braz. J. Phys.* **34** (2004) 1662
- [93] A. C. Melissinos: *Experiments in Modern Physics* (Academic Press, 1973)
- [94] M. E. Kiziroglou, X. Li, A. A. Zhukov, P. A. J. De Groot, C. H. De Groot: *Solid-State Electronics* **52** (2008) 1032
- [95] R. R. Newton: *Phys. Rev.* **73** (1948) 1122

- [96] A. V. Phelps, Z. Lj. Petrović: *Plasma Sources Sci. Technol.* **8** (1999) R21
- [97] H. Seiler: *Journal of Applied Physics* **54** (1983) R1
- [98] F. Taccogna, S. Longo, M. Capitteli: *Physics of Plasmas* **11** (2004) 1220
- [99] J. P. Gunn: *Plasma Physics and Controlled Fusion* **54** (2012) 085007
- [100] J. R. M. Vaughan: *IEEE Trans. on Electron Devices* **36** (1989) 1963
- [101] J. R. M. Vaughan: *IEEE Trans. on Electron Devices* **40** (1993) 830
- [102] H. C. Smith, C. Charles, R. W. Boswell: *Physics of Plasmas* **10** (2003) 875
- [103] M. Radmilović-Radjenović, B. Radjenović, Š. Matejčik, M. Klas: *Plasma Chem. Plasma Process.* **34** (2014) 55
- [104] W. S. Boyle, P. Kisliuk: *Phys. Review* **97** (1955) 255
- [105] P. Kisliuk: *J. Appl. Phys.* **30** (1959) 51
- [106] D. B. Go, D. A. Pohlman: *Journal of Applied Physics* **107** (2101) 103303
- [107] S. N. Sen, A. K. Ghosh: *Proc. Phys. Soc.* **80** (1962) 909
- [108] S. N. Sen, A. K. Ghosh: *Proc. Phys. Soc. A* **79** (1962) 180
- [109] H. A. Blevin, S. C. Haydon: *Proc. Phys. Soc.* **81** (1963) 490
- [110] C. L. Wadhwa: *High Voltage Engineering* (New Age International, 2007)
- [111] R. T. Lee, H. H. Chung, Y. C. Chiou: *Proc. Inst. Electr. Eng.- Sci. Meas. Technol* **148** (2001) 8
- [112] M. Radmilović-Radenović, J. K. Lee: *Physics of Plasmas* **12** (2005) 063501
- [113] T. Kihara: *Rev. Mod. Phys.* **24** (1952) 45
- [114] N. Yu. Kropotov, A. Yu. Kachanov, A. G. Reuka, V. A. Lisovskiy, V. D. Erorenkov, V. Farenik: *Sov. Tech. Phys. Lett.* **14** (1998) 159
- [115] V. A. Lisovskiy, V. D. Yegorenkov: *J. Phys. D: Appl. Phys.* **27** (1994) 2340
- [116] A. Ganguli, R. D. Tarey: *Current Science* **83** (2002) 279
- [117] C. Charles, R. W. Boswell, K. Takahashi: *Plasma Physics and Controlled Fusion* **54** (2012) 124021
- [118] M. J. Colgant, M. Meyappan, D. E. Murnick: *Plasma Sources Sci. Technol.* **3** (1994) 181
- [119] L. J. Varnerin, S. C. Brown: *Phys. Rev.* **79** (1950) 946
- [120] M. Radmilović-Radjenović, B. Radjenović: *Plasma Sources Sci. Technol.* **15** (2006) 1
- [121] S. Hamaguchi: *IBM J. Res. Develop. B* **43** (1999) 199
- [122] M. A. Harlin, S. C. Brown: *Phys. Review* **74** (1948) 291.
- [123] M. Radmilović-Radjenović, B. Radjenović: *Spectroscopy Letters* **44** (2011) 146
- [124] D. Anderson, U. Jordan, M. Lisak, T. Olsson: *IEEE Trans. On Microwave Theory and Techniques* **47** (1999) 47
- [125] S. Z. Li, H. S. Uhm: *Physics of Plasmas* **11** (2004) 3443
- [126] R. A. Siliprandi: *Atmospheric Pressure Plasmas for Surface Modifications* (UNIVERSIT' A DEGLI STUDI DI MILANO-BICOCCA, 2007)
- [127] L. J. Cranberg: *J. Appl. Phys.* **23** (1952) 518
- [128] W. Liu, D. Zhang, F. Kong: *Plasma Science and Technology* **14** (2012) 122
- [129] M. A. Shannon, P. W. Bohn, M. Elimelech, J. G. Georgiadis, B. J. Marinas, A. M. Mayes: *Nature* **452** (2008) 301
- [130] C. M. Du, J. Wang, L. Zhang, H. X. Li, H. Liu, Y. Xiong: *New J. Phys.* **14** (2012) 013010
- [131] K. R. Stalder, G. Nersisyan, W. G. Graham: *J. Phys. D: Appl. Phys.* **39** (2006) 3457

- [132] P. Bruggeman, C. Leys: *J. Phys. D: Appl. Phys.* **42** (2009) 053001
- [133] P. Bruggeman, D. Schram, M. A. Gonzalez, R. Rego, M. G. Kong, C. Leys: *Plasma Sources Sci. Technol.* **18** (2009) 025017
- [134] M. Klas, Š. Matejčik, M. Radmilović-Radjenović, B. Radjenović: *Europhys. Letters* **99** (2012) 57001
- [135] T. J. Lewis: *IEEE Trans. Electr. Insul.* **EI-20** (1985) 123
- [136] N. Prasad, J. D. Craggs: *Proc. Phys. Soc.* **76** (1960) 223
- [137] R. Hackam: *J. Phys. D: Appl. Phys.* **4** (1971) 1134
- [138] N. Škoro, D. Marić, G. Malović, W. G. Graham, Z. Lj. Petrović: *Phys. Rev. E* **84** (2011) 055401
- [139] R. A. Millikan, R. A. Sawyer: *Physical Review* **12** (1919) 167
- [140] R. H. Fowler, L. Nordheim: *Proceedings of the Royal Society (London)* **119** (1928) 173
- [141] E. L. Murphy, R. H. Good: *Physical Review* **102** (1956) 1464
- [142] C. D Ehrlich, E. W. Plummer: *Physical Review B* **18** (1978) 3767
- [143] R. J. Noer: *Applied Physics A* **28** (1982) 1
- [144] I. Brodie, I. Weissman: *Vacuum* **14** (1964) 299
- [145] R. V. Latham, C. J. S. Chapman: *Journal of Physics E: Scientific Instruments* **3** (1970) 732
- [146] Y. Y. Lau, Y. Liu, R. K. Parker: *Physics of Plasmas* **1** (1994) 2082
- [147] J. D. Lawson: *The Physics of Charged-Particle Beams* (Clarendon Press, 1988)
- [148] R. P. Little, S. T. Smith: *IEEE Transactions on Electron Devices* **12** (1965) 77
- [149] R. P. Little, W. T. Whitney: *Journal of Applied Physics* **34** (1963) 2430
- [150] N. S. Xu, R. V. Latham: *High Voltage Vacuum Insulation: Basic Concepts and Technological Practice, chapter 5* (Academic Press, 1995)
- [151] W. P. Dyke, J. K. Trolan, E. E. Marten, J. P. Barbour: *Physical Review* **91** (1953) 1043
- [152] W. P. Dyke, J. K. Trolan, E. E. Marten, J. P. Barbour: *Physical Review* **91** (1953) 1054
- [153] F. M. Charbonnier, C. J. Bennette, L. W. Swanson: *Journal of Applied Physics* **38** (1967) 627
- [154] P. Kranjec, L. Ruby: *Journal of Vacuum Science and Technology* **4** (1967) 94
- [155] D. Alpert, D. A. Lee, E. M. Lyman, H. E. Tomaschke: *Journal of Vacuum Science and Technology* **1** (1964) 35
- [156] C. J. Bennette, L. W. Swanson, F. M. Charbonnier: *Journal of Applied Physics* **38** (1967) 634
- [157] D. K. Davies, M. A. Biondi: *Journal of Applied Physics* **41** (1970) 88
- [158] D. K. Davies, M. A. Biondi: *Journal of Applied Physics* **48** (1977) 4229
- [159] Y. T. Yen, D. T. Tuma, D. K. Davies: *Journal of Applied Physics* **55** (1984) 3301
- [160] P. G. Slade, E. D. Taylor: *Proc. IEEE Elect. Contacts* (2001) 245
- [161] A. A. Al-Tabbakh, M. A. More, D. S. Joag, I. S. Mulla, V. K. Pillai: *ACS Nano* **4** (2010) 5585
- [162] Y. Khlifia, K. Kassmia, A. Aziza, F. Oliviea: *The European Physical Journal Applied Physics* **28** (2004) 27
- [163] L. Wu, H. Duan, P. Bai, M. Bosman, J. K. Yang, E. Li: *ACS Nano* **7** (2013) 707
- [164] M. Radmilović-Radjenović, B. Radjenović: *IEEE TRANSACTIONS ON PLASMA SCIENCE* **35** (2007) 1223

- [165] M. Radmilović-Radjenović, B. Radjenović, Š. Matejčik, M. Klas: *Europhys. Letters* **103** (2013) 45002
- [166] J. M. Houston: *Phys. Rev.* **88** (1952) 349
- [167] R. E. Burgess, H. Kroemer: *Phys. Rev.* **90** (1953) 515
- [168] K. Yuasa, A. Shimoi, I. Ohba, C. Oshima: *Surf. Sci.* **520** (2002) 18
- [169] L. Yingjie, R. Tirumala, P. Rumbach, D. B. Go: *IEEE Transaction on Plasma Science* **41** (2013) 24
- [170] Y. Feng, J. P. Verboncoeur: *Phys. Plasmas* **13** (2006) 073105
- [171] J. M. Dawson: *Phys. Fluids* **5** (1962) 445
- [172] O. Buneman: *Phys. Rev.* **115** (1959) 115
- [173] C. K. Birdsall, A. B. Langdon: *Plasma Physics via Computer Simulation* (McGraw-Hill, 1985)
- [174] R. W. Hockney, J. W. Eastwood: *Computer Simulation Using Particles* (McGraw-Hill, 1981)
- [175] W. S. Lawson: *J. Comput. Phys.* **80** (1989) 253
- [176] J. P. Verboncoeur, M. V. Alves, V. Vahedi, C. K. Birdsall: *J. Comput. Phys.* **104** (1993) 321
- [177] R. W. Boswell, I. J. Morey: *Appl. Phys. Lett.* **52** (1988) 21
- [178] V. Vahedi, M. Surendra: *Comput. Phys. Commun.* **87** (1995) 179
- [179] V. Vahedi, G. DiPeso, C. K. Birdsall, M. A. Lieberman, T. D. Rognlien: *Plasma Sources Sci. Technol.* **2** (1993) 261
- [180] J. P. Verboncoeur: *Plasma Phys. Control. Fusion* **47** (2005) A231
- [181] J. P. Verboncoeur, A. B. Langdon, N. T. Gladd: *Comput. Phys. Commun.* **87** (1995) 199
- [182] J. P. Boris: *Proc. 4th Conf. on Numerical Simulation of Plasmas* (1970) 3
- [183] G. J. M. Hagelarr, L. C. Pitchford: *Plasma Sources Sci. Technol.* **14** (2005) 722
- [184] M. Radmilović-Radjenović, Š. Matejčik, M. Klas, B. Radjenović: *J. Phys. D: Appl. Phys.* **46** (2013) 015302
- [185] E. Hourdakis, B. J. Simonds, N. M. Zimmerman: *Review of scientific instruments* **77** (2006) 034702
- [186] P. Guillot, P. Belenguer, L. Therese, V. Lavione, H. Chollet: *Surface and interface analysis* **35** (2003) 590
- [187] M. S. Mokrov, Y. P. Raizer: *Technical Physics* **78** (2008) 47
- [188] G. Auday, Ph. Guillot, J. Galy, H. Brunet: *J. Appl. Phys.* **83** (1998) 5917
- [189] M. Klas, Š. Matejčik, B. Radjenović, P. Papp, M. Radmilović-Radjenović: *Nuclear Instruments and Methods B* **279** (2012) 100
- [190] M. Radmilović-Radjenović, B. Radjenović, M. Klas, Š. Matejčik: *Micro&Nano Letters* **7** (2012) 232



**Dr. Marija Radmilović-Radjenović** obtained her M.Sc. and Ph.D degrees at the Faculty of Physics, University of Belgrade (2001). Dr. Radmilović-Radjenović is research professor at the Institute of Physics, University of Belgrade. During 2004-2005, she was a research professor at POSTECH, University of Science and Technology, Pohang, S. Korea. She was a general secretary of the organizing committee of 5th EU-Japan Workshop on Plasma Processing. She has published more than 70 papers and has been cited more than 400 times without self citations.



**Prof. dr. Branislav Radjenović** was born on June 10<sup>th</sup>, 1954. He received his B.Eng., M.Sc. and Ph.D degrees (1990) from the Faculty of Electrical engineering, University of Belgrade. He joined Military Technical Institute in Belgrade in 1980, where he worked on the design of weapon systems and telecommunication devices. From 1993 he taught several courses: Solid State Electronics, Electromagnetics, Optoelectronics, Television technique and Digital electronics at Military Technical Academy in Belgrade. During 2004-2005, he was a Research Professor at POSTECH, University of Science and Technology, Pohang, S. Korea. From 2008 he is Research Professor at the Institute of Physics, University of Belgrade. Dr. Branislav Radjenović has been supervisor to several Ph.D and M.Sc theses. He has published so far more than 60 articles in leading international scientific journals including 2 review articles, 4 chapters in the books and was author/co-author in more than 10 invited lectures at international conferences.



**Dr. Matej Klas** received his M.S (2007) and Ph.D. (2011) degrees from the Comenius University in Bratislava, Slovak republic. From 2011 until 2012, he was working as a post-doctoral researcher at the Notre Dame University, USA. Currently, he is working as a researcher at the Comenius University in Bratislava. His research is focused on atmospheric thermal and cold pressure plasma jets, low pressure plasma at very high electric field and plasma diagnostics.



**Aleksandar Bojarov** obtained his MSc. degree at the Faculty of Electrical Engineering, University of Belgrade, department for Nanoelectronics, Optoelectronics and Laser technique, University in Belgrad (2010). He is Phd student at the Faculty of Physics, University of Belgrade.



**Prof. Dr. Štefan Matejčík** obtained his MSc in Physics at Comenius University in Bratislava, Slovakia (1991) and PhD in Physics at Leopold-Franzens University in Innsbruck, Austria (1995). Since 1998 he is employed at Faculty of Mathematics, Physics and Informatics, Comenius University, since 2008 as full professor and 2012 as Head of the Department of Experimental Physics. His research fields are the interaction of low energy electrons with atoms, molecules and clusters, the ion-molecule processes, mass spectrometry, ion mobility spectrometry and electric discharges.